Lattice Boltzmann simulations of fluid flow in the vicinity of rough and hydrophobic boundaries

Von der Fakultät Mathematik und Physik der Universität Stuttgart zur Erlangung der Würde eines Doktors der Naturwissenschaften (Dr. rer. nat.) genehmigte Abhandlung

vorgelegt von
Christian Kunert
aus Stuttgart

Hauptberichter: P.D. Dr. Jens Harting
Mitberichter: Prof. Dr. Udo Seifert

Tag der mündlichen Prüfung: 17.02.2010

Institut für Computerphysik der Universität Stuttgart

2010

Disclaimer

Most results presented in this thesis have been published already in the following articles:

- J. Hyväluoma, C. Kunert, and J. Harting "Simulations of slip flow on nanobubble-laden surfaces " *Journal of Physics: Condensed Matter* **22**, *in press* (2010)
- C. Kunert, J. Harting, and O. I. Vinogradova, "Random-roughness hydrodynamic boundary conditions ", *Physical Review Letters* **105**, 016001 (2010).
- J. Harting, C. Kunert, and J. Hyväluoma, "Lattice Boltzmann simulations in microfluidics: probing the no-slip boundary condition in hydrophobic, rough, and surface nanobubble laden microchannels", *Microfluidics and Nanofluidics* **8**, 1-10 (2010).
- C. Kunert and J. Harting, "Calibration of lubrication force measurements by lattice Boltzmann simulations", *Proceedings of the 2nd Micro and Nano Flows Conference (2009)*, ISBN 978-1-902316-72-7 (2009).
- C. Kunert and J. Harting, "Simulation of fluid flow in hydrophobic rough microchannels", *International Journal of Computational Fluid Dynamics* **22**, 475-480 (2008).
- J. Harting and C. Kunert, "Boundary effects in microfluidic setups", *in NIC series* **39***: NIC Symposium 2008*, edited by G. Münster, D. Wolf, M. Kremer (2008).
- C. Kunert and J. Harting, "On the effect of surfactant adsorption and viscosity change on apparent slip in hydrophobic microchannels", *Progress in Computational Fluid Dynamics* **8**, 197 (2008).
- C. Kunert and J. Harting "Roughness induced boundary slip in microchannel flows", *Physical Review Letters* **99**, 176001 (2007).

Hiermit versichere ich, dass ich diese Arbeit selbstständig verfasst habe und nur die angegebenen Quellen und Hilfsmittel benutzt habe.

Christian Kunert, Stuttgart, den 23.09.2010

Contents

Chapter 1

Zusammenfassung in deutscher Sprache

1.1 Fachlicher Hintergrund und Motivation

In den letzten Jahren hat die Mikro- und Nanofluidik eine stark wachsende Bedeutung in der Industrie gewonnen. Das wurde durch mehrere an Förderprogrammen unterstützt. Dabei galt die Aufmerksamkeit vor allem dem Design von Mikrokanälen. Die physikalischen Grundlagen des Flusses in kleinen Geometrien wurden aber vernachlässigt, obwohl der Fluß in solchen Geometrien meist nicht durch klassische Kontinuumsmethoden beschrieben werden kann. Besonders die Wechselwirkung zwischen der Flüssigkeit und der Kanalwand spielt in Mikrofluid-Systemen eine wichtigere Rolle, da das Verhältnis der Oberfläche zum Volumen weit größer ist als in makroskopischen Systemen. Das bedeutet, dass die Randbedingungen in solchen Systemen besonders genau untersucht werden müssen. In den letzten Jahren ist dabei eine Verletzung der Haftbedingung beobachtet worden. Das hat zur Folge, dass als Randbedingung in Mikrofluid-Systemen Naviers' Schlupfbedingung

$$u_y(x_0) = \beta \frac{\partial u_y(x)}{\partial x}|_{x=0}, \tag{1.1}$$

angewendet werden muss. Dabei ist u_y die Flussgeschwindigkeit in y Richtung. β ist die sogenannte Schlupflänge (engl. slip-length) und $\frac{\partial u_y(x)}{\partial x}$ die Scherrate der Flüssigkeit an der Oberfläche. Eine anschauliche Interpretation der Schlupflänge ist, dass sie die Position innerhalb der Wand angibt, in der das extrapolierte Geschwindigkeitsprofil verschwindet. In den letzten Jahren wurden zahlreiche Experimente zur Messung der Schlupflänge durchgeführt, die abr widersprüchliche Ergebnisse lieferten – sowohl was den absoluten Wert der Schlupflänge angeht als auch die Abhängigkeiten von verschiedenen Parametern. Mittlerweile gibt es aber einen Konsens darüber, dass Schlupflängen in einfachen Flüssigkeiten an hydrophoben Oberflächen unter einem Mikrometer liegen, typischerweise sogar deutlich unter 100nm. Andere Daten lassen auf scheinbaren Schlupf schliessen. Wie dieser scheinbare Schlupf aber zustande kommt und wovon er abhängt, ist weitgehend unbekannt. Mögliche Ursachen für diesen Effekt sind die Oberflächenrauigkeit oder die Bildung von Gasblasen auf der Oberfläche.

Die Untersuchung dieser Phänomene ist sehr schwierig. Eine analytische Beschreibung von rauen Oberflächen ist nur in wenigen Fällen möglich. Deshalb sind Computersimulationen hilfreich, um einen tieferen Einblick zu erhalten und so das scheinbare Auftreten von Schlupf in Experimenten zu verstehen. Dabei ist zu klären, welche Simulationsmethode geeignet ist. Die Ursache von Hydrophobizität liegt auf der molekularen Skala. Deshalb wären MD-Simulationen ein angemessenes Mittel. Allerdings sind die verfügbaren Längen- und Zeitskalen zu klein. Klassische CFD-Kontinuums-Löser können problemlos diese Längen- und Zeitskalen erreichen, sind aber nicht in der Lage, Wechselwirkungen auf molekularer Skala zu modellieren. Aus diesem Grund bieten sich sogenannte mesoskopische Methoden an, bei denen nicht die gesamte Molekülbewegung simuliert wird, sondern nur deren statistisches Mittel. In dieser Arbeit geht es um die Simulation von Fluss in der Umgebung von rauen und hydrophoben Oberflächen mittels der Gitter Boltzmann Methode.

Zu Beginn der Arbeit wird in Kapitel 3 ein Überblick über die gängigen Experimente zur Schlupfbestimmung gegeben. Besonderes Augenmerk wird dabei auf Experimente gelegt, die die hydrodynamische Kraft auf eine Kugel an der Spitze eines Kraftfeld-Mikroskops messen, die in einer Flüssigkeit gegen die zu untersuchende Oberfläche bewegt wird. Die gemessene Kraft F wird dann mit dem theoretischen Wert

$$F_z = -\frac{6\pi R_e^2 \mu v}{h} f^* \tag{1.2}$$

verglichen. Die Korrekturfunktion ist durch

$$f^* = \frac{1}{4}\left(1 + 6\frac{h}{4\beta}\left[\left(1+\frac{h}{4\beta}\right)\ln\left(1+\frac{4\beta}{h}\right) - 1\right]\right). \tag{1.3}$$

gegeben. Dabei ist μ die Viskosität der Flüssigkeit, v die Geschwindigkeit und R der Radius der Kugel. Der Abstand zwischen Kugel und Oberfläche ist h. Die Schlupflänge β wird dann durch das Anfitten der Korrekturfunktion an die Messwerte ermittelt.

1.2 Simulationsmethode

Kapitel 4 gibt einen Überblick über verschiedene Simulations-Methoden wie Molekular-Dynamik (MD), dissipative Teilchen-Dynamik (DPD), sowie die stochastische Rotationsdynamik (SRD). Im Folgenden wird dann die Gitter-Boltzmann-Methode beschrieben, mit welcher die Simulationen dieser Arbeit durchgeführt werden. Dabei betrachtet man die Dynamik der Einteilchen-Verteilungsfunktion η. Sie ist ein Maß, für die Wahrscheinlichkeit ein Teilchen mit Geschwindigkeit $\mathbf{c}$ am Ort $\mathbf{x}$ anzutreffen. Dabei ist der Phasenraum auf einem Gitter diskretisiert. Somit läßt sich die Gitter Boltzmann Gleichung als

$$\eta(\mathbf{x} + \mathbf{c}_i, \mathbf{c}_i, t + \delta t) - \eta(\mathbf{x}, \mathbf{c}_i, t) = \Omega \tag{1.4}$$

ausdrücken [129]. Dabei ist $\mathbf{x}$ der diskretisierte Ort, $\mathbf{c}_i$ die diskretisierte Geschwindigkeit, die so gewählt ist, dass sie in einem Zeitschritt δt, gerade zum nächsten oder nächst-nächsten Nachbarn reicht [129]. Der linke Teil der Gleichung gibt an, wie sich

die virtuellen Teilchen frei bewegen, welche durch die Einteilchenverteilungsfunktion beschrieben werden. Der Kollisionsoperator Ω steht dann für Kollisionen, die dafür sorgen, dass die Verteilung η zu einem Gleichgewicht η^{eq} tendiert. Die lokale Masse und der Impuls der Flüssigkeit bleiben dabei erhalten.

Durch Erweiterungen der Methode ist es möglich, die hydrophobe Flüssigkeits-Wand-Wechselwirkung durch eine Shan Chen Kraft

$$F_{wf}(\mathbf{x}) = \Psi^{\text{fluid}}(\mathbf{x}) \sum_i \mathbf{c}_i g_{wf} \Psi^{\text{wall}}(\mathbf{x} + \mathbf{c}_i) \tag{1.5}$$

zu modellieren. Dabei ist Ψ^{fluid} eine Funktion der lokalen Flüssigkeitsdichte, g_{wf} ein globaler Kopplungssarameter und Ψ^{wall} ein Maß für die Hydrophobizität der Wand an der angegebenen Position $\mathbf{x}$. Es wurde gezeigt, dass solch ein Modell in der Lage ist, einen Wandschlupf zu erzeugen, der von der Stärke der Wechselwirkung und dem Druck der Flüssigkeit abhängt [48].

Ferner ist die Methode in der Lage, sich bewegende Teilchen in der Flüssigkeit zu simulieren. Dazu wird die Teilchenwand auf dem Gitter diskretisiert. Die Gitterwandpunkte tauschen dann ihren Impuls mit der Flüssigkeit aus. Auf diese Weise kann auch die gesamte hydrodynamische Kraft, die auf das Teilchen wirkt, bestimmt werden.

1.3 Fluss über raue Oberflächen

In Kapitel 5 wird Poiseuille-Fluss über raue Oberflächen untersucht. Dabei wird die Überlegung verfolgt, dass sich eine raue Oberfläche durch eine effektive Wand beschreiben läßt, die sich zwischen den Spitzen und den Vertiefungen der Rauigkeit befindet. Um die Position der effektiven Wand zu bestimmen wird die effektive Kanalbreite bestimmt, indem das theoretische Flussprofil an das gemessene angefittet wird. Aus der effektiven Kanalbreite lässt sich dann die effektive Wandhöhe bestimmen, welche den Abstand der effektiven Wand zum tiefsten Punkt der Rauigkeit angibt [74].

Es wird zuerst gezeigt, dass die Methode in der Lage ist, die theoretischen Werte für die effektive Wandposition von Panzer et al. für sinusförmige Rauigkeit wiederzugeben [108]. Auch können die Werte von Lecoq et al. für eine dreiecksförmige Rauigkeit bestätigt werden [88]. Allerdings ist es mittels analytischer Verfahren nicht möglich, komplexere Oberflächen mit starken Variationen zu beschreiben. Aus diesem Grund ist man zur Untersuchung solcher Oberflächen auf numerische Verfahren angewiesen. Da das Verfahren für die analytisch lösbaren Fälle die korrekte Position ergibt, werden weitere Modellrauigkeiten untersucht. Das sind Rillen mit quadratischem und dreieckigem, Querschnitt, sowie eine Rauigkeit mit zufälliger Rauigkeitshöhe an jedem Punkt der Oberfläche. Abschließend wird der Fluss über eine Oberfläche simuliert, wie sie in Experimenten verwendet wurde.

Die Ergebnisse lassen sich folgendermassen zusammenfassen: Die Position der effektiven Wand steigt linear mit der maximalen Höhe der Rauigkeit. Sie hängt nur im geringen Maß von der tatsächlichen Form der Rauigkeit ab. Für Rillen mit quadratischem Querschnitt befindet sich die effektive Wand bei 95% der maximalen Rauigkeit. Für Rillen mit dreieckigem Profil bei 85 % und bei gleichverteilten, zufälligen

Rauigkeitselementen bei 92%. Für die Rauigkeit einer experimentellen Oberfläche wurde ermittelt, dass die Position der effektiven Wand an derselben Stelle liegt, wie die einer zufälligen Oberfläche mit derselben gaußförmigen Höhenverteilung. Weiter wird in diesem apitel festgestellt, dass eine falsch angenommene Wandposition großen Einfluss auf die Schlupfmessung haben kann. Abschließend wird auch gezeigt, dass Rauigkeit den Schlupf an hydrophoben Oberflächen sowohl erhöhen als auch herabsetzen kann: je nach Stärke der Hydrophobizität und Höhe der Rauigkeit [74, 76, 49].

1.4 Kraftmessung einer Kugel in der Umgebung einer glatten Oberfläche

In Kapitel 6 wird überprüft, ob die theoretischen Werte für die Kraft auf eine Kugel in der Nähe der Wand erreicht werden. Das sind wichtige Vorarbeiten, um sicherzugehen, dass spätere Ergebnisse nicht das Resultat von Simulationsartefakten sind. Dabei wird die simulierte Kraft mit der Theorie von Maude für eine Kugel, die sich einer Wand nähert, verglichen [95]. Auf diese Weise kann gezeigt werden, dass der Einfluss der Diskretisierung und des begrenzten Simulationsvolumens unter zwei Prozent liegt wenn das Verhältnis von Systemgröße zu Radius größer als 16/1 ist und der Radius mindestens acht Gitterpunkte misst. Außerdem wird überprüft, ob der Schlupf, der durch die hydrophoben Wände erzeugt wird, auch durch die Kraftmessung erfasst werden kann. Dabei zeigt sich, dass der Schlupf, der durch die Kraftmessung bestimmt wird, wie erwartet, mit dem einer Poiseuille-Flussmessung übereinstimmt.

1.5 Kraftmessung einer Kugel in der Umgebung einer rauen Oberfläche

In Kapitel 7 geht es um die Untersuchung von rauen Oberflächen mittels der Kraftmessung an einer Kugel, die gegen die Wand bewegt wird. Aufgrund der Erkenntnisse aus den vorangegangenen Kapiteln wird zuerst gezeigt, dass sich Rauigkeit in diesem Fall auch durch eine effektive Wand beschreiben lässt und nicht durch eine Schlupf-Korrektur wie in Gleichung 1.3. Mittels Poiseuille-Fluss zwischen festen Wänden ist es nicht möglich, die beiden Fälle genau zu unterscheiden. Es wird überprüft, wie weit die Annahme einer effektiven Wand gültig ist. Dabei konnte innerhalb der Grenzen der Simulationsgenauigkeit keine Abhängigkeit der effektiven Wandposition vom Kugelradius, vom Abstand der Kugeloberfläche zur Wand oder dem ,,Auftreffpunkt" gefunden werden. Das heisst unter anderem, dass die effektive Wandposition unverändert bleibt, selbst wenn die maximale Höhe der Rauigkeit grösser als der Kugelradius ist.

Ein besonderes Augenmerk liegt auf der Untersuchung von Oberflächen mit einer Rauigkeit, die aus zufällig verteilten, gleich hohen Rauigkeitselementen besteht. Dabei wird festgestellt, dass schon bei einer Bedeckung von nur 10% der Oberfläche die effektive Wandposition bei 90% der Elementhöhe liegt. Weiter kann gezeigt wer-

den, dass die Position der effektiven Wand Position für isotrope Oberflächen mit der für Poiseuille-Fluss übereinstimmt. Bei Oberflächen, die eine Vorzugsrichtung aufweisen, wie zum Beispiel Gräben, befindet sich die effektive Wand zwischen den Werten für Fluss in einer der beiden ausgezeichneten Richtungen [78].

1.6 Superhydrophobe Oberflächen

Kapitel 8 beschreibt die Untersuchung von superhydrophoben Oberflächen. Dazu werden zuerst zwei superhydrophobe Einheitszellen vorgestellt. Die erste besteht aus einem Graben mit quadratischem Querschnitt, dessen Innenwände stark hydrophob sind. Auf diese Weise entsteht eine Dampfblase im Inneren des Grabens über den die äussere Flüssigkeit mit stark verminderter Reibung fliessen kann. Die Dampfblase kann über den Rand des Kanals herausragen (oder unter ihm bleiben) und bildet mit der festen Oberfläche, den sogenannten Herrausragungswinkel φ (engl. protrusion angle). Die zweite Zelle besteht aus einer zylindrischen Aussparung in der Oberfläche, deren Innenwände ebenfalls stark hydrophob sind. Während die erste Einheitszelle eine quasi 2D Struktur hat, besitzt die zweite eine echte 3D Struktur.

Die Schlupfeigenschaften der Oberfläche werden in diesem Fall wieder durch das Anlegen eines Poiseuille-Flusses ermittelt und es werden erste Ergebnisse gezeigt. Zunächst werden die Flussprofile in Flussrichtung und orthogonal zur Flussrichtung ermittelt und mit den experimentellen Daten von Tsai et al. verglichen [142]. Dabei wird in guter Übereinstimmung mit dem Experiment festgestellt, dass das Flussprofil aufgrund der Schlupf-Keinschlupfstreifen in Flussrichtung stark oszilliert. Die Oszillation nimmt stark ab, je weiter das Flussprofil von der Wand entfernt aufgenommen wird. Orthogonal zur Flussrichtung ergibt sich ein schlupfbehaftetes Parabelprofil, welches man für eine derartige Geometrie erwartet. Weiter wird die Abhängigkeit der Schlupflänge von φ, mit den theoretischen Voraussagen von Davis und Lauga verglichen. Dabei wird beobachtet, dass die Schlupflänge stark von φ abhängt und ein Maximum bei $\varphi_{\max} = 31°$ hat. Weiter wird die Schlupflänge für φ grösser als $\varphi_c i > 70°$ negativ. Diese Ergebnisse stimmen mit der Theorie von Davis und Lauga überein, allerdings sind die in der Simulation gefundenen Schlupflängen kleiner als die vorausgesagten. Das liegt an der relativ großen Grenzfläche zwischen der Dampf- und der Flüssigkeitsphase. Andererseits nimmt die Theorie perfekten Schlupf auf der Blasenoberfläche an. Des weiteren ist φ aufgrund der Dicke der Grenzschicht nicht eindeutig definiert. Abschliessend wird dann ermittelt, dass die Blase bei hohen Scherraten deformiert wird, was zu einer Reduktion der Schlupflänge führt. Ein Effekt, der auch von Hyväluoma und Harting beobachtet wurde [59].

Ausblick

Die Ergebnisse dieser Arbeit zeigen, dass Rauigkeit und Hydrophobizität zu unterschiedlichem Verhalten der Flüssigkeit an der Oberfläche führen. Weiter wird gezeigt, dass das Zusammenspiel aus Rauigkeit und Hydrophobizität zu unerwarteten Phänomenen führt. Wird hingegen die Rauigkeit nicht in die Auswertung von

Experimenten einbezogen, wie beispielsweise bei der Schlupfmessung mittels eines AFM, führt das zu einer groben Ungenauigkeit der Ergebnisse.

Auf Basis der verwendeten Simulationsmethode lassen sich nun auch weitere Fragestellungen beantworten. Beispielsweise kann der Einfluss der Deformation von Dampfblasen an superhydrophoben Oberflächen untersucht werden. Einige Experimente beobachten beispielsweise eine Erhöhung des Schlupfes mit der Scherrate. Hier wurde vermutet, dass sich die Blasen dabei von der Oberfläche lösen. Des Weiteren wäre es interessant zu untersuchen, in wie weit sich die Deformation der Blasen auf die Lubrikationskraft in Kraftmessungsexperimenten auswirkt.

Chapter 2

Introduction

During the last decade, micro- and nano-technology has become an important industry. This development has been assisted by a funding policy supporting the design of miniaturized mechanical structures and complex micro-machines through which fluids move. However, the actual transport of fluids in these confined geometries have become an area of interest only during the recent years, even though the fluid flow on increasingly smaller scales cannot always be properly described by conventional continuum equations: physical phenomena which, can be neglected on the macro scale, become dominant as the length scale diminishes. On the other hand, systems on scales on which micro effects become sensible cannot yet be treated by molecular methods, owing to the lack of computational power. Hence, there is a definite need for novel theories, numerical methods, and measurement techniques devised to properly describe the confined fluid flow on length scales in the range from 10 and 1000nm.

Reynolds numbers in microfluidic systems are usually small, i.e., usually below 0.1. In addition, due to the small scales of the channels, the surface to volume ratio is high causing surface effects like wettability or surface charges to be more important than in macroscopic systems. Also, the mean free path of a fluid molecule might be of the same order as the characteristic length scale of the system. For gas flows, this effect can be characterized by the so-called Knudsen number [70]. While the Knudsen number provides a good estimate for when to expect rarefaction effects in gas flows, for liquids one would naively assume that its velocity close to a surface always corresponds to the actual velocity of the surface itself. This assumption is called the no-slip boundary condition and can be counted as one of the generally accepted fundamental concepts of fluid mechanics. However, this concept was not always well accepted. Some centuries ago, there were long debates about the velocity of a Newtonian liquid close to a surface and the acceptance of the no-slip boundary condition was mostly due to the fact that no experimental violations could be found, i.e., a so-called boundary slip could not be detected.

In recent years, it became possible to perform very well controlled experiments that have shown a violation of the no-slip boundary condition in sub-micron sized geometries. Since then, mostly experimental [86, 30, 139, 16, 20, 5, 27, 149, 139], but also theoretical works [146, 43], as well as computer simulations [130, 3, 23, 136, 140] have been performed to improve our understanding of boundary slip. The topic is

of fundamental interest because it has practical consequences in the physical and engineering sciences as well as for medical and industrial applications. Interestingly, also for gas flows, often a slip length much larger than expected from classical theory can be observed. Extensive reviews of the slip phenomenon have recently been published by Lauga et al. [86], Neto et al. [104], as well as Bocquet and Barrat [12].

The reason for such findings is that the behavior of a fluid close to a solid interface is very complex and involves the interplay of many physical and chemical properties. These include the wettability of the solid, the shear rate or flow velocity, the bulk pressure, the surface charge, the surface roughness, as well as impurities and dissolved gas. Since all those quantities have to be determined very precisely, it is not surprising that our understanding of the phenomenon is still very unsatisfactory.

A boundary slip is typically quantified by the so-called slip length β – a concept that was already proposed by Navier in 1823 [101]. He introduced a boundary condition where the fluid velocity at a surface is proportional to the shear rate at the surface (at $y = y_0$), i.e.,

$$u_x(y_0) = \beta \frac{\partial u_x(y)}{\partial y}. \tag{2.1}$$

In other words, the slip length β can be defined as the distance from the surface where the relative flow velocity vanishes.

The substantial scientific research invested in the slip phenomenon has lead to a more clear picture which can be summarized as follows: one can argue that many surprising published results were only due to artefacts or misinterpretation of experiments. In general, there seems to be an agreement within the community that slip lengths larger than a few nanometers can usually be referred to as "apparent slip" and are often caused by experimental artefacts. However, the understanding of those artefacts is limited because it involves a large interplay of different parameters. Besides this, it is interesting whether such an apparent slip is based on a physical effect that can be technically used or if it is simply a misinterpretation of experimental results.

Therefore, it is of importance to perform computer simulations which have the advantage that most parameters can be changed independently without modifying anything else. Thus, the influence of every single modification can be studied in order to present estimates of expected slip lengths or experimental "errors".

One of the most important deviations between the reality and the idealized case which is used for the analysis of the experimental data, is surface roughness. Typically, it is assumed that surface roughness simply increases friction and therefore decreases any possible slip. However it is still not clear how surface roughness should be treated in microfluidic setups. This problem becomes more serious when the surface becomes hydrophobic, since hydrophobicity is known to cause slip [86, 104, 12]. Here, the interplay of roughness can cause so-called super-hydrophobicity, as it is known in the lotus effect [115]. In this thesis, computer simulations are applied to investigate the influence of roughness and the influence of the combination of roughness and hydrophobicity on the slip phenomenon.

The simulation method used to study microfluidic devices has to be chosen carefully. While Navier-Stokes solvers are able to cover most problems in fluid dynamics, they lack the possibility to include the influence of molecular interactions as needed

to model boundary slip. Molecular dynamics (MD) simulations are the best choice to simulate the fluid-wall interaction, but the computer power today is not sufficient to simulate length and time scales necessary to achieve orders of magnitude which are relevant for experiments. However, boundary slip with a slip length β of the order of many molecular diameters σ has been studied with molecular dynamics simulations by various authors [136, 23, 24, 5, 111]. The problem of MD simulations is that the achievable time- and length scales are very small. Therefore, mesoscopic simulation methods should be applied to describe phenomena in microfluidics.

This work focuses on numerical investigations of the slip phenomenon by means of lattice Boltzmann simulations with a strong focus on roughness and the interplay between roughness and wetting phenomena. To do so, two different slip measurement methods are simulated. One is to apply a Poiseuille flow between two patterned boundaries, and to record the flow profile. Then, the profile can be compared to the theoretical one, which assumes a slip boundary condition. The second method records the drag force that is acting on a sphere which is moved with a constant velocity towards the observed surface. Due to the influence of the boundary, the drag force acting on the sphere is disturbed and a correction function is needed to describe the measured force. This correction function, which depends on the slip, is fitted via the slip length towards the recorded force.

The lattice Boltzmann method has to be extended to be able to simulate hydrophobic boundaries by means of a repulsive fluid-boundary interaction. Further, it is necessary to implement a multi-phase model to simulate liquid- and gas phases in the vicinity of the boundary. Both tasks can be achieved by a Shan-Chen interaction [124, 126]. The next important enhancement is the implementation of moving objects. Ladd et al. have developed a method to implement this [82]. A detailed description of the simulation method which is applied here is given in chapter 4.

In chapter 5, fluid flow in the vicinity of rough surfaces is investigated. Here, different model roughnesses and experimental surfaces are implemented in the simulation. The roughness is described by means of an effective boundary position that corresponds to a virtual plane at which the no-slip boundary condition holds. An important finding is the fact that the effective boundary position mainly depends on the maximum height of the roughness elements but only to a small extent on the actual shape or the detailed position of them [74].

An alternative way of investigating boundaries is the measurement of the drag force acting on a sphere that is approaching a surface. Since the boundary condition on the surface is changing the fluid flow in its vicinity and thus the drag force created by the flow around the sphere changes. This effect is utilized in many experiments where typically a sphere is attached to the cantilever of an atomic force microscope which approaches a surface [146, 147, 128, 13, 156, 157]. To simulate such a behavior it is essential to understand the limits of the applied simulation method. Therefore, detailed studies of finite size and discretization effects in a system of a sphere, which is approaching a flat surface, are performed in chapter 6 [77]. Further, it is shown that the results for the slip length β in a Poiseuille flow and a drag force measurement are equivalent. Therefore, it is possible to utilize the simulation scheme to investigate other boundary properties as well.

In chapter 7, the findings of chapter 6 are used to investigate the influence of a

rough surface on the drag force. Here, it is possible to demonstrate that the drag force shows a different asymptotic behavior when the sphere is approaching a rough or a slippery surface. A rough surface can be described by an effective boundary position that leads to a shift of the recorded force curve, while a slip surface requires a complex correction function [78]. This finding is important because it is not possible to distinguish a shift or slip in a Poiseuille or Couette flow setup with fixed separation between the boundaries. However, the question of the correct boundary condition is fundamental in nature.

After the investigation of rough surfaces the interplay of roughness and hydrophobicity is of interest. Here, the focus lies on the flow over so-called super-hydrophobic surfaces. At these surfaces, a gas bubble is trapped in the asperities of the surface roughness, leading to a decreased friction. In chapter 8, two super-hydrophobic cells are presented. In addition, Poiseuille flow over such surfaces is studied and the preliminary findings are compared to analytical and experimental studies. A good agreement to experimental data is found considering the flow profiles and the dependence of the slip length on the protrusion angle, which depicts how strongly the bubble invades into the bulk fluid. Further, a shear dependence of the slip length is detected due to the deformation of the bubbles trapped in the roughness.

The results show that the roughness has an influence on slip measurements. In case of a wrongly assumed boundary condition, large apparent slip length could be measured. Further, the interplay of roughness and hydrophobicity can lead to both, an increase and a decrease of the apparent slip. Here, future research can be done applying the presented methods.

Chapter 3

Slip in microfluidic devices

For more than a century the no-slip boundary condition, stating that the velocity of a fluid close to a solid boundary is equal to the boundary velocity, was assume to describe fluid flow. Its wide acceptance is founded on the fact that no experimental violation was found on a macroscopic length scale. To characterize slip in 1823 Navier [101] postulated a slip boundary condition stating that the flow velocity v at the boundary at $x = 0$ is proportional to the shear rate and the so-called slip length β,

$$v(x = 0) = \beta \frac{\partial v}{\partial x}|_{x=0}. \tag{3.1}$$

In the recent years, fluid flow in micro and nano sized geometries has become a popular research topic. Here, several experiments have been performed that showed a violation of the no-slip boundary condition, which can be explained by Navier's slip boundary condition (or its tensorial generalization [7]). However, typical slip lengths are found to be less than one μm.

In the following chapter an overview on typical slip experiments is given. Further, some controversial findings are presented and different dependencies are discussed. Those contradicting experimental results are the starting point for this thesis. Therefore, it is necessary to understand the fundamentals of the experimental setups and possible error sources.

3.1 How slip is detected

In recent years, it became possible to perform very well controlled experiments that have shown a violation of the no-slip boundary condition in sub-micron sized geometries. Since then, mostly experimental [86, 30, 139, 16, 20, 5, 27, 149, 139], but also theoretical works [146, 43], as well as computer simulations [130, 3, 23, 136, 140] have been performed to improve our understanding of boundary slip. However, many results are contradicting each other concerning the value of slip and the influence of different parameters. Extensive reviews of slip phenomena have been published recently by Lauga et al. [86], Neto et al. [104], and Bocquet and Barrat [12]. Therefore, only a short overview on the topic will be given.

In this section the most common experiments, simulations and theories about boundary slip are discussed. A strong focus lies on the experiments based on force

measurements, since they are the foundation of this thesis. Then an overview on possible parameters that have an influence on the slip length β is given and reasons for the development of slip are discussed.

3.1.1 Double focus cross correlation

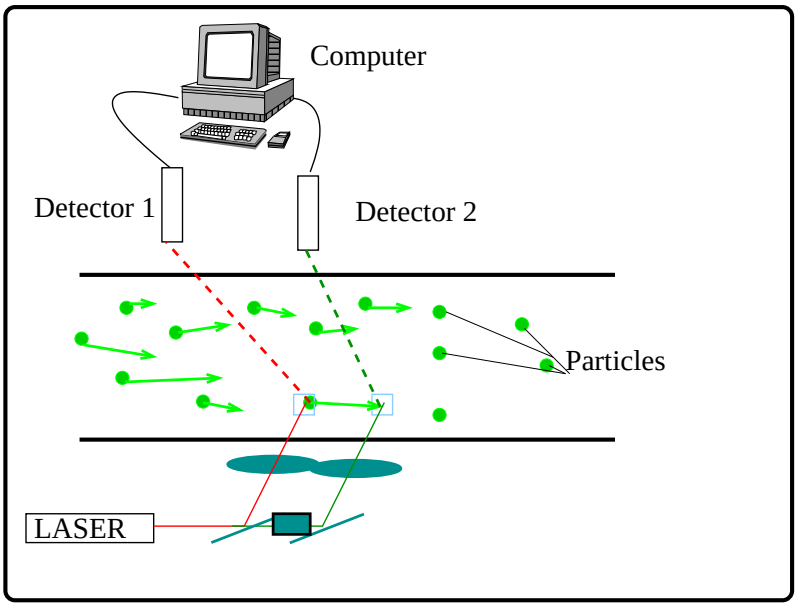

Figure 3.1: Cartoon of the cross correlation method. The particles are illuminated by the foci of two laser beams. By calculating the time cross-correlation function the velocity between the two foci can be derived.

For the cross correlation method fluorescent particles are brought into the flow. Typically, a laser beam split into two beams is used to illuminate the particles. The two beams can be focused at a fixed distance at a fixed location. By having two beams at a fixed distance it is possible to record every particle that crosses one of the focal points of the beams. The technique rests in the premise that only a small number of labeled particles are simultaneously located in an effective focal volume of the order of 10^{-15}l. Therefore the time cross-correlation can be used to determine the average time a particle needs to cross the second focus after it crosses the first one. A time cross-correlation function $g_2(t)$ may generally be derived from any two time-resolved intensities $I_1(t')$, $I_2(t')$. It is calculated via

$$g_2(t) = \frac{\langle I_1(t')I_2(t'+t)\rangle_{t'}}{\langle I_1(t')\rangle_{t'}\langle I_2(t')\rangle_{t'}},$$

with $\langle ...\rangle_{t'}$ denoting the ensemble average for an ergodic system. The quantity $I_n(t')$ is given by the fluorescence intensity detected by focus n at time t'. Typically the time cross-correlation function exhibits a local maximum t_m which is the average time a particle needs to travel from one focus to the other.

Since the focus of the laser beams can be located very precisely one has an accurate measurement of the flow velocity at a given point [91]. Pit et al. have applied

the cross correlation method for hexadecan flowing on a hydrocarbon lyophobic smooth surface, and found a slip length of 400nm [110].Vinogradova et al. refined the method and determined a slip length for water and NaCl aqueous solution of less than 100nm which is independent on the shear rate and the salt-concentration, at a hydrophobic polymer channel. For hydrophilic surfaces no measurable slip was detected [148] .

3.1.2 Micro particle image velocimetry

A common tool for the measurement of flows is the so-called particle image velocimetry (PIV). The method is very similar to the cross correlation method, but instead of just taking into account single events of a particle crossing the focus of a laser beam, one takes a whole video and correlates the single frames to each other, in a similar way as described in the section above.

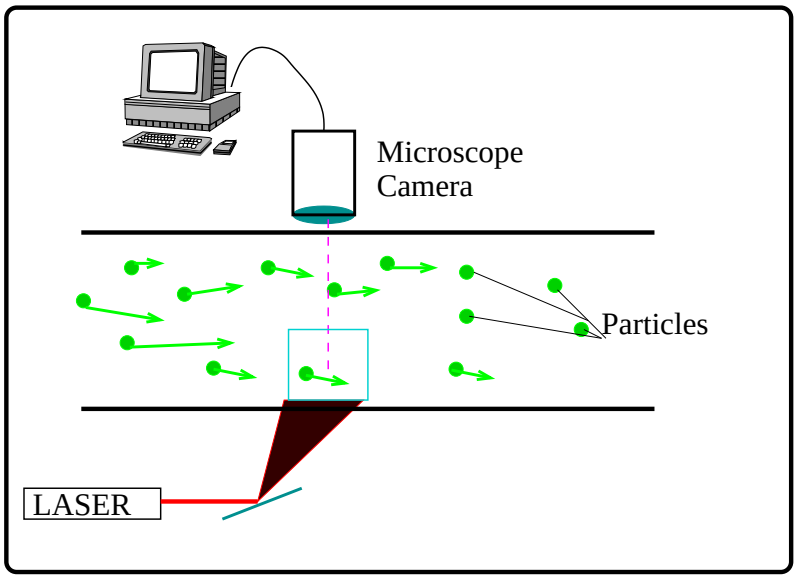

Figure 3.2: A cartoon of the PIV method. The particles are illuminated by a laser and their movement is recorded by a camera through a microscope. The data is then analysed by a computer by calculating the cross-correlation function between consecutive frames.

The simplest form of micro-PIV is to illuminate the whole micro-channel under a microscope and to take an video. The disadvantage of such a setup is that possible frame rates are low so the correlation is highly disturbed by the Brownian motion of the particles. Therefore typically the volume is illuminated by two laser pulses with different wave length. By this, the autocorrelation can be determined on a much smaller timescale, which reduces the noise.

Tretheway and Meinhart [138, 139] applied micro PIV in hydrophobic glass channels and measured slip lengths of up to 1μm. However Joseph and Tabeling [67] found slip lengths of less than 100nm, stating that this is the minimal resolution of the method, i.e., that it is doubtful whether there is any slip.

Both methods have systematic problems in the measurement of slip in Newtonian fluids. The basic assumption of the methods is that the particles have the same

velocity as the fluid and that the particles do not disturb the fluid flow. In case of simple fluids on a length scale that is not large compared to the particle size those assumptions might not be valid. Further, the particles might interact directly with the boundary which influences their velocities.

3.1.3 Flow rates

A less direct method to measure the slip length is to measure the mass flow $Q = \int \rho v dA$ through a pipe and compare the ratio between the theoretical value $Q_{\text{Poiseuille}}$ and the measured one Q_β. Here v is the flow velocity and A is the cross-section of the pipe. For a circular pipe with radius R the slip length can be calculated via

$$\frac{Q_\beta}{Q_{\text{Poiseuille}}} = 1 + \frac{4\beta}{R}. \tag{3.2}$$

Experiments of this kind have been performed by different groups using different fluids and different channels. An early experiment was performed by Schnell in 1956, finding a slip length of $\beta = 1...10\mu$m [122]. However, this early experiments suffer from a lack of accuracy. More recent experiments report slip lengths of $10 - 70$nm [138]. For an overview on slip measurements several reviews have been published recently [104, 86, 12, 90]. The measurement of the flow rate has several problems. The first one is that it is hard to exactly measure the parameters that enter the flow rate like the radius of the channel or the exact pressure drop. The second drawback of the method is that all deviations to the flow rate automatically result in a measured slip length. Therefore one obtains no deeper understanding of a potential slip mechanism.

3.1.4 Force measurement

A very popular way to measure fluid slip is the measurement of the lubrication force acting on a sphere that is approached towards a surface. Since such experiments are one of the background of this thesis, a more detailed overview on their theoretical background is given here.

The main theory was developed by O.I. Vinogradova [149, 150, 147, 146] and is an extension of the Reynolds lubrication theory adopted for slip surfaces. For simplicity the derivation concentrates on spherical rigid bodies instead of arbitrarily curved surfaces as presented in [69]. Additionally the focus lies on the case where a no-slip boundary condition is applied on one sphere with radius R_1 approaching another sphere with infinite radius R_2 (i.e. a flat surface). According to the symmetry a cylindrical coordinate system (r, θ, Z) is employed, thus the spheres move along the z-axis. The angular direction θ drops out. The distance between the two surfaces is h and the approaching velocity is v. The two surfaces can be described by paraboloids:

$$Z = h + \frac{1}{2}\frac{r^2}{R_1} + O(r^4)$$

and

$$Z = -\frac{1}{2}\frac{r^2}{R_2} + O(r^4)$$

By shifting coordinates with $z = Z + r^2/(2R_2)$ and $R_e = R_1R_2/(R_1+R_2)$ the surfaces read as

$$z = h + \frac{1}{2}\frac{r^2}{R_e} + O(r^4)$$

and

$$z = O(r^4).$$

From the Stokes equation of a fluid with viscosity μ, pressure gradient $\nabla\mathbf{p}$ and the fluid velocity of $\mathbf{u}$

$$\mu\nabla^2\mathbf{u} = -\nabla\mathbf{p}$$

we get

$$\mu\frac{\partial^2 u_r}{\partial z^2} = \frac{\partial p}{\partial r} \tag{3.3}$$

when assuming that pressure gradient in z-direction vanishes $\frac{\partial p}{\partial z} = 0$. This implies that the pressure is a function of r only. On the lower boundary we now assume a slip boundary condition with the slip length β, which reads as

$$u_z = 0$$

and

$$u_r = \beta\frac{\partial u_r}{\partial z}$$

while on the top surface we apply the no-slip boundary condition so we get

$$u_z - \frac{ru_r}{R_e} = -v$$

and

$$u_r = 0.$$

In the original paper by O.I. Vinogradova [146] an arbitrary slip β_1 is assumed but for simplicity we focus on the case that is applied in this thesis, i.e. $\beta_1 = 0$. The solution of Eq. 3.3 with the given boundary conditions reads now as

$$u_r = \frac{1}{2\mu}\frac{\partial p}{\partial r}\left[z^2 - z\frac{H^2}{H+\beta} - \frac{\beta H^2}{H+\beta}\right],$$

where $H = h + \frac{r^2}{2R_e}$. Further, the continuity equation

$$\frac{\partial u_z}{\partial z} + \frac{1}{r}\frac{\partial(ru_r)}{\partial r} = 0$$

has to be fulfilled. By integrating we get

$$v = \frac{1}{r}\frac{\partial}{\partial r}\left[\left(r\frac{\partial p}{\partial r}\right)\frac{\partial p}{2\mu}\left(\frac{H^3}{3}3 - \frac{H^4}{2(H+\beta)} - \frac{\beta H^3}{H+\beta}\right)\right]$$

which gives us the dependence of the flow field on the constant relative velocity v of the spheres. Due to this we have obtained a differential equation of the pressure p:

$$\frac{d}{dr}\left(X^{-1}r\frac{dp}{dr}\right) = 2\mu v r \tag{3.4}$$

where

$$X = \frac{6(\beta + H)}{-H^3(H + 4\beta)}.$$

By integrating Eq. 3.4 two times while assuming $p = 0$ for $r \to \infty$ and due to the rotational symmetry $\frac{dp}{dr} = 0$ at $r = 0$ one obtains

$$p = -\frac{3\mu R_e v}{H^2} p^*,$$

with the dimensionless correction function

$$p^* = \frac{1}{4} 2 \frac{H}{3\beta} \left[1 - \frac{H}{4\beta} \ln(1 + \frac{4\beta}{H}) \right],$$

The hydrodynamic resistance force F on the upper sphere is now the inverted of the one acting on the lower surface. Therefore it can be calculated as

$$F_z = -\int_0^\infty \left(-p + 2\mu \frac{dv_z}{dz} \right) 2\pi r \; dr.$$

Since the contribution of the outer region can be neglected one concludes that the pressure term is dominant and one ends up with

$$F_z = -\frac{6\pi R_e^2 \mu v}{h} f^* \tag{3.5}$$

where

$$f^* = \frac{1}{4} \left(1 + 6 \frac{h}{4\beta} \left[\left(1 + \frac{h}{4\beta} \right) \ln \left(1 + \frac{4\beta}{h} \right) - 1 \right] \right). \tag{3.6}$$

In the case of a flat lower surface, as discussed above, R_e will become the radius of the upper sphere R. The force is valid for small distances h and slow approaching velocities v. Eq. 3.5 is widely used in experiments, but here some corrections have to be applied, due to deviations from the ideal case. Such deviations include the acceleration of the sphere due to surface forces, or the drag force of the cantilever.

A typical experimental setup is shown in Fig. 3.3. On the cantilever of an atomic force microscope (AFM) or a surface force apparatus (SFA) a silicon sphere is attached. Then the surface is approached towards the sphere while the distance and the force are recorded and compared with Eq. 3.5 using the slip length β in f^* as a fit parameter.

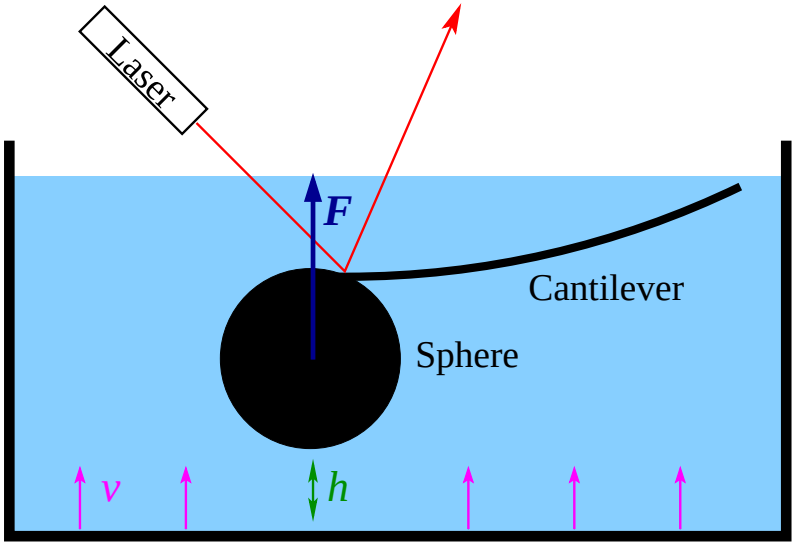

Figure 3.3: Typical setup of an AFM-based slip experiment. The lower surface is approached towards the silicon sphere attached to the cantilever of the AFM.

Several authors used this method to investigate slip phenomena but ended up with different results, like slip length varying from a few nm up to 2.5μm [156, 157, 158, 140, 24, 25, 30, 103, 17]. Additionally there was a strong argument about whether the slip length depends on the shear rate or not. Craig et al. published several articles about shear dependent slip [30, 103, 104], but there was no further evidence like computer simulations for their findings and the shear dependency could not be reproduced with a different setup. Later it was argued that the shear dependency is an experimental artefact from a torsion of the cantilever that appears only with a specific cantilever setup [151]. Further, problems in such experiments appear due to the simplifications that have to be made in the theory. Those include the constant and small velocity and perfectly smooth surfaces. Therefore the experimental data has to be processed. For example due to the van der Waals interaction between the sphere and the surface the velocity and the force itself has to be adopted. Further the exact boundary shape and position is unknown what requires separate measurements which do not include the actual surface properties at the point of contact, i.g. between the slip measurement and the surface measurement, impurities might settle on the surface.

3.2 Reasons for boundary slip

Generally, the slip length β is just a mesoscopic parameter, meaning it includes a variety of microscopic effects like wetting, surface roughness, or surface charge. In this section different causes and different "types" of slip are discussed. Their dependences on different parameters is shown.

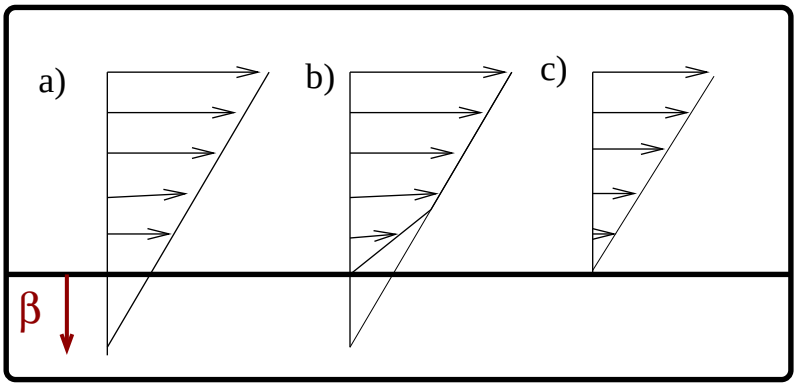

Figure 3.4: Depiction of the slip length β. The scatches show: intrinsic (or molecular) slip (a), apparent slip (b), and no-slip (c).

Slip can be categorized into intrinsic slip and apparent slip as depicted in Fig. 3.4. Intrinsic (or molecular) slip means that the fluid has a non-zero velocity at the boundary, down to molecular resolution. Apparent slip means that there is a layer in which the effective viscosity of the fluid is reduced and therefore the fluid velocity increases stronger than it does in the bulk. When the whole velocity field is observed, this increased velocity appears as slip. Usually the low viscosity layer is so small that it is below the spatial resolution of the experiment. In this case it is not possible to distinguish between both kinds. Further, the concept of slip is a continuum model, which has its basis on the molecular scale. This means that a possible reduction of the friction between the liquid and the solid boundary or the reduction of the viscosity takes place on a molecular length scale. However the slip length assumes a continuum velocity close to the boundary which makes it necessary to be in the hydrodynamic limit. Thus in case the low viscosity layer is in the range of a few molecular diameters one cannot apply a continuum approximation for this layer and therefore a distinction between the two types is not only an experimental problem but as well a theoretical one. An additional problem is the fact that the slip length is always coupled with the position of the boundary. In most experiments it is not possible to distinguish between slip and a shift of the boundary position. Therefore, all measured slip is just a mesoscopic effective slip.

Besides the question of what kind of slip one is looking at, there are different theories about the origin of the detected slip. For gases, Maxwell [96] postulated that a molecule will be reflected with the probability $(1 - p)$ while it inelastically collides with the probability p. The mean free path for a single molecule with the effective cross section σ in a gas of density ρ is $l_m \approx 1/(\sqrt{2}\pi\sigma^2\rho)$. With this one can calculate a slip length as

$$\beta = \frac{2-p}{3p} l_m. \tag{3.7}$$

This is a classical example of slip in rarefied gases. But for liquids this assumption cannot be applied, since the mean free path is not well defined.

Another classical example of slip occurs in non Newtonian liquids. The reason for this is either shear thinning or shear thickening which leads to a slip effect due to the shear forces near the boundary. In polymer solutions depletion layers occur.

Here, the polymers are not entering an area close to the boundary[152]. Since the solution has a higher viscosity than the solvent, apparent slip occurs [49].

The most simple explanation of slip is the low friction between the boundary and the fluid molecules, compared with the inner friction of the liquid [83]. Reasons might be repulsive forces between the fluid and the boundary, like at hydrophobic boundaries. However, this effect is small since other effects like the surface roughness generally increase the friction so it is questionable whether the low molecular friction overcompensates this unless there is a mechanism that creates more slip due to roughness. The surface-fluid interaction that causes the slip might be increased by the roughness due to the larger total surface.

One way to decrease the friction is the formation of nano-bubbles. They are either formed by solved gas or vapor that forms bubbles in pockets created by the surface roughness. Since the viscosity of the gas inside the bubbles is very low the fluid will slide over this film of bubbles [43, 142]. Specially designed surfaces can be produced to create gas or vapor bubbles. Such surfaces show a very large contact angle and therefore are called super-hydrophobic surfaces which will be discussed later. A way to create such surfaces is the deposition of carbon nanotubes to form so-called carbon nanotube forests [25, 66, 26]. Another possible geometry are grooves that are filled with vapor [142].

In the case that the surface roughness is of the same order of magnitude as the size of the fluid molecules the molecules get trapped inside the roughness, but in the case where the molecules are significantly larger, they will just roll over the roughness. In consequence the friction is reduced and slip occurs. This effect is known for friction of solid state bodies [73] and MD simulations came to similar conclusions [39, 40].

Another phenomenon in a fluid near a solid surface is the ordering of the fluid molecules according to the crystal structure of the solid boundary. Due to this ordered fluid layers are formed which can slide over each other with reduced friction [132, 120].

Due to the variety of different effects that influence the surface-fluid interaction and therefore the slip length, one observes a significant dispersion of the results for almost similar systems [86, 104]. For example, observed slip lengths vary between a few nanometers [21] and micrometers [139] and while some authors find a dependence of the slip on the flow velocity or shear rate [20, 156, 30], others do not [16, 139].

However, the substantial scientific research during the past few years allows to draw a clearer picture that can be summarized as follows: many surprising results published were only due to artifacts or misinterpretation of experiments. In general there seems to be an agreement within the scientific community that slip lengths in simple fluids larger than "a few nanometers" can usually be referred to as apparent slip and are often caused by experimental artefacts. Small slip length are even harder to determine experimentally and require sophisticated methods like the presented AFM measurements or well controlled micro PIV experiments.

Extensive reviews of the slip phenomenon have recently been published by Lauga et al. [86], Neto et al. [104], as well as Bocquet and Barrat [12]. This brief introduction to the topic should give a sufficient overview for this thesis while a deeper insight is given by the cited literature.

3.3 Surface roughness

One important parameter entering the slip length β is the surface roughness that cannot be neglected if the height of the roughness is of the same magnitude as typical length scales of the system. The influence of roughness on β has been investigated by numerous authors. The first idea is that roughness leads to higher drag forces and thus to no-slip on macroscopic scales. Richardson showed analytically that when looking on a no-shear (full-slip) surface with a periodic roughness a significant drag force arises that leads to a finite slip length and in the continuum limit to no-slip [114].

Panzer et al. calculated the slip length β analytically for Poiseuille flow with rough walls by performing a Fourier expansion of the streaming function Ψ containing the solution of the Navier-Stokes equations in the laminar case [108]. Ψ is obtained by a Fourier expansion of the boundary surface and of the pressure field and its solution contains information of an effective boundary. The problem of such an approach is that it works only for small wave numbers. One would have to take into account an infinite number of terms to achieve a result for arbitrary geometries. Panzer et al. gave an analytical equation for β in the case of small cosine-shaped surface variations [108]. It is applicable to two infinite planes separated by a distance $2d$ being much larger than the highest peaks $r_{\max}$. Surface variations are determined by peaks of height $r_{\max}$, valleys at $r_{\min} = 0$ and given by $r(z) = \frac{r_{\max}}{2} + \frac{r_{\max}}{2}\cos(qz)$. Here, q is the wave number. Since the surfaces are separated by a large distance, the calculated slip length is equal to the negative effective boundary r_{eff} that is found to be

$$r_{\text{eff}} = -\beta = \frac{r_{\max}}{2}\left(1 + k\frac{1 - \frac{1}{4}k^2 + \frac{19}{64}k^4 + \mathcal{O}(k^6)}{1 + k^2(1 - \frac{1}{2}k^2) + \mathcal{O}(k^6)}\right). \tag{3.8}$$

The first and k-independent term shows the linear behavior of the effective height r_{eff} on the average roughness $R_a = r_{\max}/2$. Higher order terms cannot easily be calculated analytically and are neglected. Thus, Eq. 5.2 is valid only for $k = \frac{q r_{\max}}{2} \ll 1$. However, for realistic surfaces, k can become substantially larger than 1 causing the theoretical approach to fail. This shows that for flow over a rough surface one has either to assume an effective boundary position inside the boundary or to describe the flow by a slip boundary condition.

Lecoq and coworkers [88] performed experiments with well defined roughness, and developed a theory to predict the position of the effective boundary. For the experiments they utilised a laser interferometer to measure the trajectory of a colloidal sphere and thereby determined the lubrication force and an effective boundary position. The used geometry consists of grooves with a triangular profile. For a theoretical description the boundary is expressed in a Fourier series that gives the boundary condition for the Laplace equation. From this an effective boundary can be derived by a fast converging series. The approach is very similar to the theory of Panzer et al. and only varies in details and in the investigated surface, i.e., the shape being triangular instead of sinusoidal.

However, an analytical description of the flow near an arbitrarily rough surface is not possible [83]. The reason is that the surface has to be expressed in an expansion that enters the covering flow equations but the higher orders of the expansion

cannot be neglected in an arbitrary geometry. Thus, the correct boundary condition is unknown. Therefore in classical boundary layer theory the usage of the "sand equivalent" is still in use [119]. This means that a rough surface is compared to a surface with sand of different grain sizes glued on it.

Besides the obvious creation of friction there are some cases were roughness leads to a slip effect. Jansons has shown analytically that even few perturbations on flat surfaces lead to mesoscopic slip [64]. This was experimentally demonstrated by McHale and Newton [98]. Jabbarzadeh et al. performed molecular dynamics (MD) simulations of Couette flow between sinusoidal walls and found that slip appears for roughness amplitudes smaller than the molecular length scale [63]. Also, it can cause pockets formed by the corrugations of the surface, to be filled with vapor or gas nanobubbles leading to apparent slip [33, 66]. Molecular dynamics simulations (MD) have been applied to investigate roughness as well [154, 1]. Recently, Sbragaglia et al. applied the LB method to simulate fluids in the vicinity of microstructured hydrophobic surfaces [117] and Varnik et al. showed that even in small geometries rough channel surfaces can cause flow to become turbulent [144].

3.4 Super-hydrophobic surfaces

In recent years specially designed surfaces have become popular. In the context of fluid dynamics and with a special focus on slip phenomena so-called super-hydrophobic surfaces are of great interest. A review of the topic was written by Rothstein [115].

3.4.1 Hydrophobic surfaces

When talking about wettability, one typically assumes a liquid drop on a solid surface surrounded by vapor. The wettability of a surface is defined by the spreading coefficient $S = \gamma_{SV} - \gamma_{LV} - \gamma_{LS}$ where γ_{SV}, γ_{LV}, and γ_{LS} are the solid-vapor, liquid-vapour, and liquid-solid interfacial tensions. For spreading coefficients greater than zero $S > 0$, the solid is fully wetted by the liquid whereas for $S < 0$, the solid is only partly wetted by the liquid, which forms a spherical end cap with an equilibrium contact angle θ defined by Young's law as [155]

$$\theta = \cos^{-1} \frac{\gamma_{SV} - \gamma_{LS}}{\gamma_{LV}}.$$

For surfaces with contact angle $\theta < 90°$ the surface is considered hydrophilic, whereas $\theta > 90°$ is called hydrophobic as depicted in Fig. 3.5. However, this applies only to the equilibrium contact angle. Due to surface roughness and other effects like chemical heterogenity a variety of contact angles is possible, depending on the actual wetted parts of the surface on the micro scale or in other words it depends on the "history" of the wetting process. This non-uniqueness of the contact angle is known as contact angle hysteresis [41].

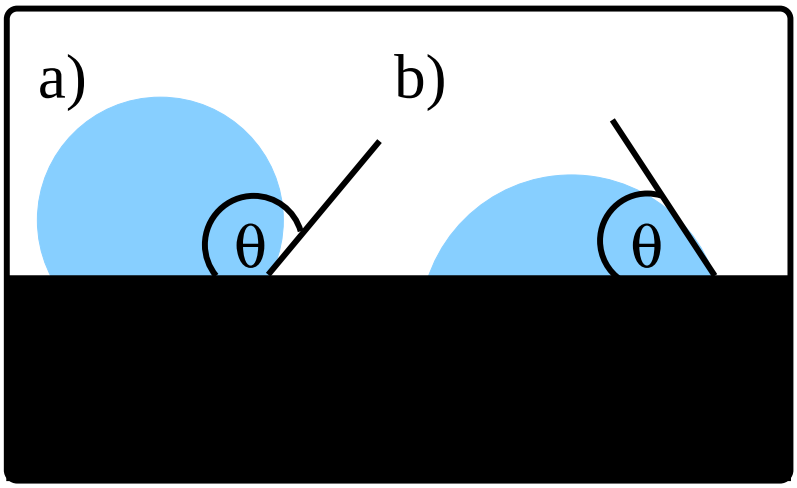

Figure 3.5: A liquid drop on a surface forms a contact angle θ with the surface. For $\theta > 90°$ the surface is considered as hydrophobic (a), whereas $\theta < 90°$ is called hydrophilic (b).

The influence of the wettability on the slip was investigated by various authors. Results showed, that hydrophobicity can cause slip lengths much larger than the mean free path. Thompson and Trojan [137] performed molecular dynamics (MD) simulations and found a nonlinear increase of the slip velocity at large (unphysical) shear rates and that the slip length diverges at a critical shear rate. Barrat and Bocquet [3, 10, 11] showed that the slip length can be larger than 40 molecular diameters in the linear (shear independent) regime that corresponds to experimental shear rates. The slip results from a liquid depletion layer near the wall. Within this layer, the density and thus the viscosity are decreased resulting in a large apparent slip. However, the possible slip length that can be achieved by plane hydrophobic surfaces is limited to some tens of nanometers and for a stronger effect some surface structure is needed.

3.4.2 Rough and hydrophobic surfaces

Super-hydrophobic surfaces were originally inspired by the strong water repellent properties of the Lotus leaf [4]. Barthlott and Neinhuis stated that a very large contact angle and a small contact angle hysteresis is responsible for the efficient self cleaning behavior of the plant's leaf and called this behavior super-hydrophobic. Due to the small hysteresis a drop becomes unstable to small perturbations on the surface and starts to roll over it.

Synthetic super-hydrophobic surfaces have been created recently by a variety of groups. They achieve a contact angle of nearly 180° with little to no measurable contact angle hysteresis. The difference between a hydrophobic and a super-hydrophobic surface lies not in the surface chemistry but in the surface structure or its topology. As an example the Lotus leaf has micrometer sized protrusions that are covered with hydrophobic wax.

One distinguishes between two different states that characterize a hydrophobic rough surface. The first one is the Wenzel state [153] in which all surface asperities

are covered with fluid. Since the total surface is larger than the projected surface area, the hydrophobicity is increased. Compared to the equilibrium contact angle θ the contact angle in the Wenzel state is given by

$$\cos\theta_W = c \cdot \cos\theta,$$

with c being a roughness parameter that can be calculated in the case of a periodic array of posts like in Fig. 3.6, as $c = 1 + 4\phi_s r/d$, where $\phi_s = \frac{d^2}{(d+w)^2}$ is the fraction of surfaces covered with posts. In the Wenzel state the contact line is pinned to the roughness and therefore the contact angle hysteresis is relatively high.

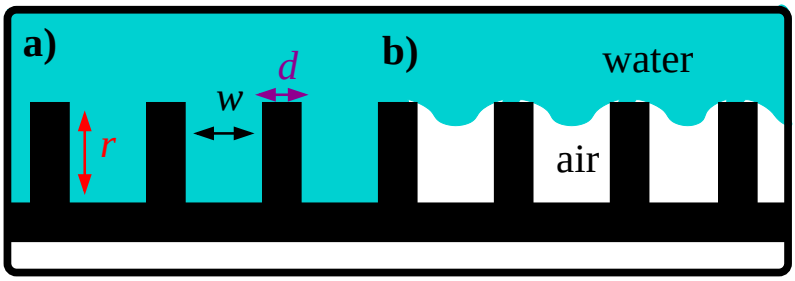

Figure 3.6: Cartoon of **a)** the Wenzel state and **b)** the Cassie-Baxter or fakir state. In the Wenzel state the fluid enters the volume w between the posts of hight r and thickness d. In the Cassie-Baxter state the fluid is not allowed to enter this free volume and sits on top of the asperities.

The second case is the so-called Cassie-Baxter state [15]. In this case, the dimples formed by the surface roughness are filled with vapor or solved gas and the fluid does not invade into them. Since the fluid sits on top of the roughness peaks like a fakir on a bed of nails another common name of this state is "fakir state". Here the equilibrium contact angle θ_C is increased by the fraction of air-water interface $(1 - \phi_s)$ so that it is given by

$$\cos\theta_C = -1 + \phi_s(1 + \cos\theta).$$

Since the contact line is only pinned to the solid pins the contact angle hysteresis is small. Due to those properties commonly only the Cassie-Baxter state is called (true) super-hydrophobic. To maximize the effect the fraction of posts-covered surface should be reduced. This leads to a practical limit since there is a maximum pressure that can be sustained by the liquid-air interface before the liquid enters the free space and the system drops into the Wenzel state.

Another interesting case that would lie in between the two possible states is one where a less viscous liquid is attracted to the surface. Here the dimples would not be filled with gas but still the friction is decreased. A possible realization would be a light oil and water solution at a hydrophobic rough boundary or a polydisperse polymer melt, where the lighter molecules are repelled less by the surface [6].

3.4.3 Slip on super-hydrophobic surfaces

As reported in the previous sections slip occurs on hydrophobic surfaces. Therefore, it is not surprising that super-hydrophobic surfaces should show large slip lengths.

The reason for a large slip-length in the fakir state is easy to understand. While on the solid parts a no-slip condition can be applied, the gas filled parts of the surface are in good approximation shear free. As example, the viscosity (and therefore the friction) of water μ_{water} is about a thousand times the viscosity of air. Therefore, a model for slip over super-hydrophobic surfaces is a surface pattern consisting of no-slip and no-shear (full-slip) areas. Theoretical studies have been performed on such a system by several authors [109, 87, 118]. Philip was the first who assumed such a model for the flow over a porous media that can be seen as a super-hydrophobic surface as well [109]. He calculated an effective slip length β_{eff} by assuming longitudinal and transversal stripes. Based on this, Lauga et al. improved the model to arbitrary stripes [87]. Feuillebois et al. concentrated on the limit of arbitrarily shaped but infinitely small elements which are more relevant since this is the case where the surface texture cannot be resolved by the experiment, and one assumes an averaged boundary condition [37]. They found that the main parameter is the fraction of no-slip to no-shear surface and not a shape parameter. Therefore, to obtain large slip lengths one needs to create a pattern that needs less supporting poles to stay in the Cassie-Baxter state. Due to the non trivial description of most surface patterns an analytical description is hard to realize and numerical methods should be applied. Classical CFD methods have been used to solve the flow field near a no-slip / full-slip patterned surface [97]. Besides the analysis of no-slip/ no-shear surfaces classical CFD methods are not able to model the underlying physics of the slip phenomenon.

For a more detailed and deeper understanding of the super-hydrophobic phenomena simulations on the molecular scale are needed. Cottin-Bizone et al. applied molecular dynamics simulations, were able to create a fakir State, and showed that the friction is dramatically reduced [25, 24].

Since the typical length- and time-scales of MD simulations are very short, it is helpful not to simulate the complete atomistic behavior but rather do a coarse-grain modeling and use so-called mesoscopic simulation methods as described in detail in chapter 4. Sbragaglia et al. used the lattice Boltzmann method to investigate a model with repulsive boundaries to create a low density layer and showed that such a model is able to simulate a drag reduction and an increased flow rate [117]. Hyväluoma and Harting used a similar method and investigate the slip length of a surface with bubbles trapped to holes in the surface. Further they showed that the deformation of the bubble due to shear has a great influence on the slip length [59].

Experimentally, there are only a few works that have measured slip on super-hydrophobic surfaces [107, 66]. Ou et al. used a series of lithographically etched and silanized grooves on a silicon surface. In a pressure driven flow they measured a drag reduction of up to 40% compared to the no-slip case, applying flow rate measurements and micro PIV. The corresponding slip length would be 25μm. Joseph et al. created a super-hydrophobic surface by deposing carbon nano tubes on a silicon substrate and measured the slip length with micro PIV. They found a slip length of a few microns in the Cassie-Baxter state that scales linearly with the characteristic roughness length, while the slip vanishes in the Wenzel state [66]. A number of more recent experiments have extended these results to a variety of super-hydrophobic surface designs and flow geometries [18, 19, 141]. Some of these

studies have moved towards super-hydrophobic surfaces with nanometer-sized features. Choi et al. studied a super-hydrophobic surface created using Teflon-coated nanogrooves with 60nm wide ridges spaced 180nm apart. They used a specially designed flow meter to measure differences in the throughput of a microfluidic device between smooth and super-hydrophobic surfaces and infer slip lengths. A slip length of roughly $\beta \approx 140$nm was found for flow parallel to the ridge direction and roughly half that length for flow transverse to the ridge direction. Choi and Kim created needle-like structures on a silicon wafer using the deposition of carbon nanotubes [18]. The resulting carbon-nanotube forest consisted of 1 to 2 nm tall nanoposts spaced 500nm to 1μm apart, which were coated with Teflon to make the surface hydrophobic. They measured drag reduction using a cone-and-plate rheometer. Slip lengths of approximately $\beta \approx 20\mu$m and $\beta \approx 50\mu m$ were determined for water and for glycerin, respectively.

Resume

To conclude this chapter it can be said that the field of microfluidics provides a variety of interesting physical phenomena that are hard to describe by analytic theories. The experimental results about slip phenomena have been discussed controversially which made a common understanding hard to achieve. However, in the past few years the effect of hydrophobicity on the flow past smooth surfaces is reasonably clear. Despite some remaining controversies in the data and amount of slip (cf. [86]), a concept of hydrophobic slippage is now widely accepted. For rough hydrophilic surfaces the situation is much less clear, and opposite experimental conclusions have been made. Computer simulations can help do draw a clearer picture of slip phenomena. However, the simulation method has to be chosen carefully. Classical CFD methods need a founded analytical theory to model sub-continuum effects. Since such a theory is missing they are less helpful in the case of micro-fluidic slip phenomena. Molecular dynamics has the advantage that it can utilize first principles but suffers of a large computational effort. Therefore, the time and length scales one can achieve by this method are too small. A possible way to approach the problem are so-called mesoscopic methods as described in the next chapter.

Chapter 4

Simulation method

As explained in the previous chapter, microfluidic experiments have a large variety of parameters that might influence the results. Mostly these parameters such as viscosity, surface roughness, and wettability influence each other or cannot be varied independently. Therefore, computer simulations can help to gain a deeper understanding of the phenomena in microfluidic systems, since here all parameters are known and can be well controlled. But still, for the simulation of microfluidic systems and the fluid-surface interaction the simulation method has to be chosen carefully. The challenge is to cover the molecular interaction and still be able to resolve the flow field and relevant time scales.

The latter could be achieved easily by classical Navier-Stokes solvers like finite volume or finite difference methods [113]. The problem lies here in the modeling of the fluid-wall interaction. It would be possible to implement a slip boundary condition but in this case the slip length β would just enter as a free parameter without any deeper physical meaning. Further, surface roughness would just be modeled by an effective boundary or require a very sophisticated mes refinement, thus the computational advantage is gone. Sophisticated models are implemented in case of turbulence, like perturbation is added to the flow field close to the boundary. To model the physical origin of surface effects, other simulation methods are needed. In this chapter, an overview on simulation methods like molecular dynamics simulations (MD), stochastic rotation dynamics (SRD), and dissipative particles dynamics (DPD) is given, followed by a description of the Lattice Boltzmann (LB) method which is used in this thesis, including a deeper insight into the used simulation technique and its theoretical foundation.

4.1 Molecular dynamics simulations and mesoscopic methods

4.1.1 Molecular dynamics simulations

Molecular-dynamics (MD) simulations are simulating the dynamics of single molecules or even atoms. It is a very well grounded type of simulation, since all information entering the method are Newtons equations of motion and the usually pairwise po-

tential between the molecules. However, the latter has some pitfalls because the potentials have to be derived from measurements or other principles. Since MD-simulations are described well in the literature [2, 38] and are not in the focus of this thesis they will be described here just briefly.

The basis for MD-simulations are Newton's equations of motion

$$m_i \frac{d^2 \mathbf{r}_i}{dt^2} = \mathbf{F}_{ij}, \tag{4.1}$$

which have to be solved for every particle i at every time-step δt. Here, $\mathbf{r}_i$ is the position of the i-th particle, m_i its mass and $\mathbf{F}_{i,j}$ is the force between the i-th and j-th particle plus possible external forces. Note that this includes already the assumption that only two-body interactions between particles have to be taken into account. In the case of strong dipolar molecules one would need multi-body interactions, and additional descriptions are necessary. Then, the Newton equations of motion are integrated numerically over the time-step δt. A commonly used integration method is the velocity Verlet algorithm. The velocity Verlet algorithm reduces the level of errors introduced into the integration by calculating the position and velocity at the next time step from the positions and velocity at the previous and current time steps:

$$\mathbf{r}(t+\delta t) = \mathbf{r}(t) + \mathbf{v}(t)\,\delta t + \frac{1}{2}\mathbf{a}(t)(\delta t)^2 \; \mathbf{v}(t+\Delta t) = \mathbf{v}(t) + \frac{\mathbf{a}(t) + \mathbf{a}(t+\delta t)}{2}\delta t \tag{4.2}$$

with $\mathbf{a} = \frac{\mathbf{F}}{m}$ being the acceleration of the particle. The standard implementation scheme of this algorithm is:

- Calculate: $\mathbf{r}(t+\delta t) = \mathbf{r}(t) + \mathbf{v}(t)\delta t + \frac{1}{2}\mathbf{a}(t)(\delta t)^2$
- Calculate: $\mathbf{v}(t+\frac{\delta t}{2}) = \mathbf{v}(t) + \frac{\mathbf{a}(t)\delta t}{2}$
- Derive: $\mathbf{a}(t+\Delta t)$ from the interaction potential.
- Calculate:$\mathbf{v}(t+\delta t) = \mathbf{v}(t+\frac{\delta t}{2}) + \frac{\mathbf{a}(t+\Delta t)\delta t}{2}$

A common interaction potential is the Lennard-Jones potential [65].

$$V_{i,j} = \epsilon \left[\left(\frac{\sigma}{r_{i,j}} \right)^{12} - \left(\frac{\sigma}{r_{i,j}} \right)^{6} \right]. \tag{4.3}$$

$r_{i,j}$ is the distance between the molecules, σ indicates the size of the molecules and ϵ the energy scale. The potential consists of a very small short range $r_{i,j}^{-12}$ repulsive term and a long range attractive $r_{i,j}^{-6}$ term. It is used due to its simplicity and its capability to be fitted to real molecular interaction potentials. Other potentials are the Yukawa potential, which has an exponential form but is missing the repulsive part. A very simple model is the hard sphere potential, where the potential is infinity when the spheres overlap, and zero otherwise.

Since one potentially needs to take into account the interaction with all particles, the calculation of the potential is the most computer time consuming part of the

MD simulation. Here, several methods like the linked-cell or neighbor-list algorithm have been introduced to reduce the computer power needed, but all of them require a truncation of the potential in order to minimise the amount of particles that have to be taken into account. Besides this the number of molecules that can be simulated is limited due to the available memory. The time scale of MD-simulations is typically very short because the time step δt has to be small. Typical length and time scales of MD simulations are below μm and nm.

To overcome these problems, so called mesoscopic models have been invented to achieve larger length scales without giving up the molecular foundation of the theory. Here, the trajectory of every single molecule is not modeled in detail but the molecular ensemble as a whole is modeled.

4.1.2 Dissipative particle dynamics

A very common method that follows the idea of simulating a molecular ensemble is the so called dissipative particle dynamics (DPD). It was introduced by Hoogerbrugge and Koelmann [58]. It is based on the idea that a simulation particle does not represent a single molecule but rather a whole group of them. The representative particles move during a time-step according to their momentum. After this, in the collision step, the particle i changes its momentum $\mathbf{p}_i$ according to

$$\dot{\mathbf{p}}_i = \sum_{j \neq i} \mathbf{F}^C_{i,j} + \sum_{j \neq i} \mathbf{F}^D_{i,j} + \sum_{j \neq i} \mathbf{F}^R_{i,j}. \tag{4.4}$$

Here $\mathbf{F}^C_{i,j}$ stands for the momentum transfer during collisions between particle i and j. The thermal fluctuations are represented by the random interaction term $\mathbf{F}^R_{i,j}$, while $\mathbf{F}^D_{i,j}$ represents dissipative terms due to viscous effects within the molecule group that is represented by the representative particle. However, to obtain a correct ensemble several conditions of the interactions have to be fulfilled as it was introduced by Español and Warren [36]. Conditions are isotropy and Galilean -invariance. Further, the random forces should have a vanishing time average and must not be correlated in time.

Since the method is very close to a molecular dynamics simulation it is possible without much programming effort to transform an existing MD-simulation package into a DPD-simulation. Further, it is no problem to introduce different species of fluid particles to simulate multi component flow (like oil and water). For this Español [28], Marsh and Coveney [94] developed an H-theorem and the method was successfully used by Coveney and Novik to simulate phase separation in shear flow [29].

Besides its good theoretical foundation and its easy implementation based on an existing MD-code, DPD intrinsically creates thermal noise. Further, it is not able to cover larger volumes since the number of particles is limited as it is in MD codes because one still needs to store a large amount of information for every particle and needs to take into account every particle-particle interaction which is computationally costly.

4.1.3 Stochastic rotation dynamics

The high computational costs of the collisions in the DPD lead to the idea of a way to simplify them with an easier collision rule. Malevantes and Kapral developed the method [92, 93] that is known under many names like *stochastic rotation dynamics*, *real-coded lattice gas*, *discrete simulation automation* or *multi-particle-collision dynamics*. The method uses a simplification idea that is based on the assumption of the Navier Stokes equation of local conservation of mass and momentum. Instead of calculating all collisions of all particles one rather assumes an interaction between them that conserves local mass and momentum but is fast to calculate. As in DPD a particle does not represent a single molecule but a whole ensemble, that has the same momentum. During the streaming step they move freely. The collision is realized by discretizing the simulated volume onto a lattice. Then, in every lattice box the center of mass velocity of all particles in the box is calculated and subtracted from each particle in the box. After this the momentum vectors are rotated by a random angle and finally the center of mass velocity is added again. By this the local momentum is conserved and on average the rotation of the velocity vectors results in the same as real collisions between particles. Due to the simplified collision one is able to simulate much larger volumes.

By using different rotations for each species it is possible to introduce a phase separation between those species [50]. Further, amphiphiles could be implemented [116]. Hecht et al. developed a model to simulate charged particles in a solution of SRD-fluid taking into account the DLVO potential of the particles and the hydrodynamic coupling [55, 53, 54].

The problem of the method is that due to the strong simplification of the collision some fundamental physical properties might be violated. In general due to the underlying lattice structure the method is not Galilei invariant, which can be overcome by a random translation of the lattice during every time-step [60, 61]. An intrinsic drawback of the method is that thermal fluctuations cannot be switched off if they are not desired. Further, to obtain averaged values, a good statistics is needed which is computationally costly.

4.2 The lattice Boltzmann method

During the last decade the lattice Boltzmann method (LBM) became a fast growing field of computational fluid dynamics (CFD). Due to its nature it is able to cover conventional CFD problems but can be adapted for high Knudsen-number $Kn > 0.1$ flow, simulate flow in porous media, and multiphase flow.

In this section the lattice Boltzmann method (LB) which is used for the simulations in this thesis is presented. The method is described in more detail beginning with the fundamentals of the method, and basic additions for boundary conditions, multiphase flow and suspensions with a strong focus on the models that are used for this thesis. Besides the used schemes an overview on alternative implementations is given as well. For more details the reader is recommended to the cited literature [129, 131].

4.2.1 The Boltzmann equation

The fundamentals of the lattice Boltzmann method is the kinetic Boltzmann equation which is well described in textbooks [123]. It is based on the evolution of the single particle distribution function $\eta(\mathbf{x}, \mathbf{v}, t)$. This function indicates how many particles are present at a point in space $\mathbf{x}$ with the velocity $\mathbf{v}$ at time t. During the time dt the particles will now move according to their velocities to the new location $\mathbf{x}^* = \mathbf{x} + \mathbf{v}dt$. In case of external forces $\mathbf{f}$ the velocity of the particles will change as well to $\mathbf{v}^* = \mathbf{v} + m\mathbf{f}dt$, with m being the mass of a particle. Without particle-particle collisions they would just move on like

$$\left[\eta(\mathbf{x} + \mathbf{v}dt, \mathbf{v} + \frac{1}{m}\mathbf{f}dt, t + dt) - \eta(\mathbf{x}, \mathbf{v}, t)\right] d^3x d^3v = 0,$$

but due to intermolecular collisions the particle distribution function η changes. This change can be described by a collision Operator Ω that represents the number of particles that enter or leave the given phase space volume so the Boltzmann equation reads as

$$\left[\eta(\mathbf{x} + \mathbf{v}dt, \mathbf{v} + \frac{1}{m}\mathbf{f}dt, t + dt) - \eta(\mathbf{x}, \mathbf{v}, t)\right] d^3x d^3v = \Omega. \tag{4.5}$$

The problem to solve is how the collision operator Ω has to be constructed. Here, it can be mentioned that Boltzmann himself could not solve this problem. However, he proposed the following thoughts that illustrate the problem.

Ω is the number of particles that enter or leave the phase space volume $\mu = [\mathbf{x}, \mathbf{x} + d\mathbf{x}];[\mathbf{v}, \mathbf{v} + d\mathbf{v}]$. Following assumptions are used: Every collision results in either a particle entering or leaving μ. Further, particles only collide with particles outside of μ or particles from outside μ are collide into μ. $W(\mathbf{v}, \mathbf{v}_2, \mathbf{v}_3, \mathbf{v}_4)$ gives the probability that two particles with velocity $\mathbf{v}$ and $\mathbf{v}_2$ collide and end up with the velocities $\mathbf{v}_3$ and $\mathbf{v}_4$ while all velocities except $\mathbf{v}$ are outside μ. Therefore, the number of particles lost during a time step is $W(\mathbf{v}, \mathbf{v}_2, \mathbf{v}_3, \mathbf{v}_4)$ and due to symmetry the number of particles added to μ is $W(\mathbf{v}_3, \mathbf{v}_4, \mathbf{v}_2, \mathbf{v}) = W(\mathbf{v}, \mathbf{v}_2, \mathbf{v}_3, \mathbf{v}_4)$. Taking into account the fact that W is proportional to the number of particles with the relevant velocity $\eta(\mathbf{v}_i)$ one ends up with

$$\begin{gathered}[\tfrac{\partial \eta}{\partial t} + v\nabla_x + \tfrac{1}{m}\mathbf{f}(\mathbf{x})\nabla_v]\eta(\mathbf{x}, \mathbf{v}, t) = \\ \int d^3v_2 \int d^3v_3 \int d^3v_4 W(\mathbf{v}, \mathbf{v}_2, \mathbf{v}_3, \mathbf{v}_4) \left[\eta(\mathbf{x}, \mathbf{v}_3, t)\eta(\mathbf{x}, \mathbf{v}_4, t) - \eta(\mathbf{x}, \mathbf{v}_2, t)\eta(\mathbf{x}, \mathbf{v}, t)\right]\end{gathered} \tag{4.6}$$

which is a non-linear integrodifferential equation.

Since the Boltzmann equation (4.6) cannot be solved analytically, different approximations have been proposed to find solutions like the one by P.L. Bhatnagar, E.P. Gross und M. Krook [9]. Their idea was that the system relaxes towards a local equilibrium distribution $\eta^{eq}(\mathbf{x}, \mathbf{v})$. Further, it can be assumed that in case the system is not far from this equilibrium it will relax with a single relaxation rate $1/\tau$. Thus, the Boltzmann equation with BGK collision operator reads as

$$\left[\frac{\partial \eta}{\partial t} + v\nabla_x + \frac{1}{m}\mathbf{f}(\mathbf{x})\nabla_v\right]\eta(\mathbf{x}, \mathbf{v}, t) = \frac{\eta(\mathbf{x}, \mathbf{v}, t) - \eta^{eq}}{\tau}. \tag{4.7}$$

Here, it should be noted that one can now "choose" the equilibrium function in order to obtain the desired physical properties. However, one needs to fulfill some requirements such as isotropy and conservation of mass and momentum. Usually, the Maxwell distribution or some expansions of it are used. By performing a Chapman Enskog procedure it is possible to show that such a model reproduces the Navier-Stokes equation if one looks at the moments of the single particle distribution function η such as mass and momentum.

4.2.2 Concept of lattice Boltzmann

The core concept of the lattice Boltzmann method is to discretize the Boltzmann equation in time, velocity- and real space [99]. This means instead of having infinitely small phase space elements μ one takes into account the single particle distribution function $\eta(\mathbf{x}_j, \mathbf{c}_i, t)$ only on a lattice site $\mathbf{x}_j$, with velocities $\mathbf{c}_i$ that point to the nearest and next-nearest neighbors. The lattice Boltzmann equation [129] then reads as

$$\eta(\mathbf{x} + \mathbf{c}_i, \mathbf{c}_i, t + \delta t) - \eta(\mathbf{x}, \mathbf{c}_i, t) = \Omega. \tag{4.8}$$

In the implementation used, the position $\mathbf{x}$ is discretized on a 3D cubic lattice with 19 discrete velocities $\mathbf{c}_i, i = 0, ..., 18$ pointing from a lattice node to its 18 neighbours and to itself (D3Q19). In two dimensions a D2Q9 model is commonly used. Since it can be drawn on a paper, such a model is used here to illustrate some parts of the used model, leaving the extension to three dimensions to the reader. Fig 4.1 shows the two lattice types. Other lattice types in two and three dimensions can be used as well but will not be discussed here. The article of Qian et al. provides an overview on different lattice schemes [112]. In his notation that is widely used in the context of lattice Boltzmann the D indicates the dimension and the Q the number of used velocities $\mathbf{c}_i$. The choice of the lattice has an impact on several quantities like the speed of sound c_s. Taking less velocities into account decreases the computational costs but computational artefacts due to the lattice nature become more severe, since certain directions might be favored, violating Galilei invariance.

The left hand side of equation (4.8) represents the advection of the particles, i.e., the population $\eta(\mathbf{x}, \mathbf{c}_i, t)$ moves during a time-step δt along its velocity $\mathbf{c}_i$ to the neighboring lattice point $\mathbf{x} + \mathbf{c}_i \delta t$. Commonly, the time step is set to $\delta t = 1$ so it is only needed for dimensional reasons and is left out very often.

The collision operator Ω represents inter-molecular interactions, i.e., collisions between molecules that lead to a redistribution of $\eta(\mathbf{x}, \mathbf{c}_i, t)$. This redistribution relaxes the single particle distribution function η towards a local equilibrium η^{eq}, while it conserves mass and momentum. The actual shape of the collision operator Ω can differ in the way how the equilibrium distribution η^{eq} is calculated or how the actual relaxation is realized. For a more detailed overview of the method the reader is referred to the literature [129, 131, 82, 45, 44, 34, 80] thus the focus lies on the two simulation codes which are actually used for this thesis.

The first code as it is used for the simulations in chapter 5 uses an BGK (or single relaxation time) collision operator, similar to the Eq. 4.7. The equilibrium

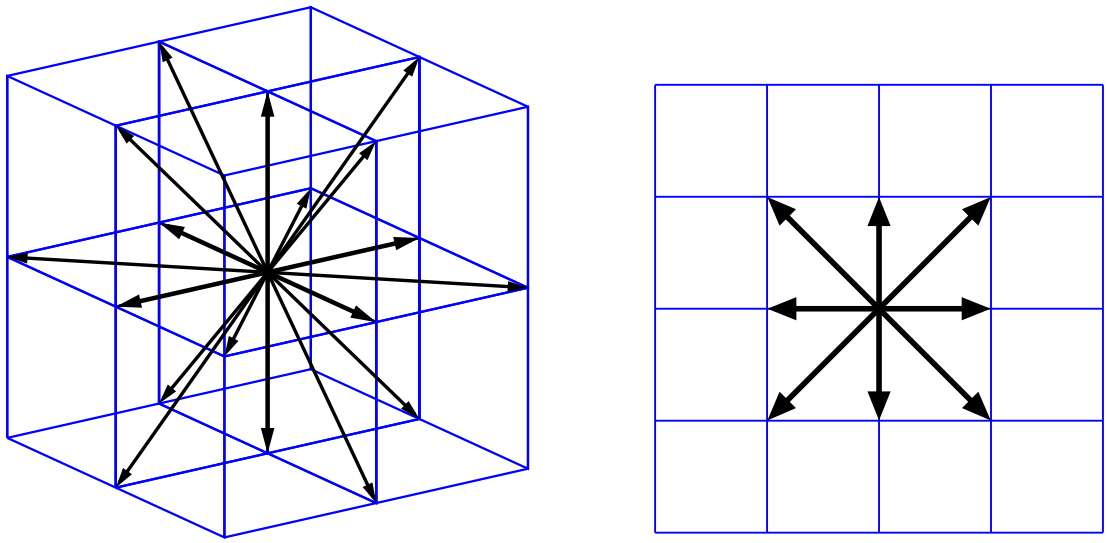

Figure 4.1: A D3Q19 lattice as it is used in the presented simulation and a D2Q9 lattice that is used for illustration. The arrows depict the 18 or 8 velocity vectors that are pointing to the nearest and next nearest neighbors. Note that a large fraction of the particles does not move and therefore an additional **0**-velocity is needed.

distribution function is given by

$$\eta_i^{eq} = \zeta_i \eta \left[1 + \frac{\mathbf{c}_i \cdot \mathbf{u}}{c_s^2} + \frac{(\mathbf{c}_i \cdot \mathbf{u})^2}{2c_s^4} - \frac{u^2}{2c_s^2} + \frac{(\mathbf{c}_i \cdot \mathbf{u})^3}{6c_s^6} - \frac{u^2(\mathbf{c}_i \cdot \mathbf{u})}{2c_s^4}\right], \tag{4.9}$$

which is a polynomial expansion of the Maxwell distribution. $c_s = 1/\sqrt{3}$ is the speed of sound for the D3Q19 lattice, $\mathbf{u}(\mathbf{x}, t)$ is the macroscopic velocity of the fluid. The second code uses a multi relaxation time collision operator as it is described in the following section.

4.2.3 Multi relaxation time approach and macroscopic values

The implementation used for the particle driven simulations originates to A. Ladd [82, 80]. It uses a multi relaxation time LB approach, where every moment of the distribution function relaxes with its own relaxation rate τ_m towards the local equilibrium m^{eq} [56]. The moments carry the physical properties of the fluid. Namely the local density

$$m_0 = \rho = \sum_i \eta_i,$$

the local momentum

$$m_{1,2,3} = j_{x,y,z} = \mathbf{e}_{x,y,z} \sum_i \eta_i \mathbf{c}_i,$$

and the momentum flux

$$m_{3...18} = \Pi = \sum_i \eta_i \mathbf{c}_i \mathbf{c}_i.$$

For simplicity the spatial and time dependencies are left out and for the velocity one writes $\eta(\mathbf{x}_i, \mathbf{c}_i, t)$ as η_i. By writing the distribution function η_i and the moments m_m in vector form $|\eta\rangle = T|m\rangle$, the lattice Boltzmann equation for the multi relaxation time approach can be written as

$$|\eta_{t+\delta t}\rangle - |\eta_t\rangle = T^{-1} S[|m_t\rangle - |m^{eq}\rangle]. \tag{4.10}$$

Vector form means that each population density $\eta(\mathbf{c}_i)$ with discrete velocity $\mathbf{c}_i$ makes one component of $|\eta\rangle = T|m\rangle$. T transforms a vector from the basis in density population space $|\eta\rangle$ into the basis of the moment space $|m\rangle$, and consists of eigenvectors of the collision rate matrix S. The density space vector $|\eta\rangle$ contains all 19 populations $\eta(\mathbf{x}, \mathbf{c}_{0,...,18})$ at a specific lattice site $\mathbf{x}$. Practical this scheme can be constructed by linearizing the collision operator around the local equilibrium η^{eq} [56]

$$\Omega_i = \sum_j \Lambda_{ij}(\eta_j - \eta_j^{eq}), \tag{4.11}$$

where Λ is the linear collision Matrix. It is not necessary to construct a particular collision operator and from this calculate Λ rather it is sufficient to consider the general principles of conservation and symmetry and then to construct the eigenvalues and eigenvectors of Λ. However, before one can do so the proper form for the equilibrium distribution function will be determined.

The equilibrium distribution η^{eq} is constructed such that it conserves local mass and momentum but changes the viscous (or non-equilibrium) part of the momentum flux $\Pi^{neq} = \Pi - \Pi^{eq}$. It is realized by

$$\rho^{eq} = \sum_i \eta_i, \tag{4.12}$$

$$\mathbf{j}^{eq} = \sum_i \eta_i \mathbf{c}_i, \tag{4.13}$$

$$\Pi^{eq} = \sum_i \eta_i^{eq} \mathbf{c}_i \mathbf{c}_i = p\mathbf{1} + \rho \mathbf{u}\mathbf{u}. \tag{4.14}$$

The equation of state is given by $p = \rho c_s^2$, where the speed of sound is given by the advection as $c_s = \sqrt{1/3}$ lattice units per time step. If not stated otherwise all values are in dimensionless lattice units. The equilibrium part is unchanged by the collision. Further, in the simulation scheme only the shear modes survive the collision process. Therefore, only the non-equilibrium momentum flux changes. The post collision non-equilibrium momentum flux Π^{neq*} is given by

$$\Pi^{neq*} = (1+\lambda)\bar{\Pi^{neq}} + \frac{1}{3}(1+\lambda_v)(\Pi^{neq} : \mathbf{1})\mathbf{1}, \tag{4.15}$$

where the over bar indicates the traceless part of the momentum flux. The star indicates, that a value is post collision. The parameter λ is an eigenvalue of Λ and

i	c_{ix}	c_{iy}	c_{iz}	c_i	i	c_{ix}	c_{iy}	c_{iz}	c_i	i	c_{ix}	c_{iy}	c_{iz}	c_i
1	1	0	0	1	7	1	1	0	$\sqrt{2}$	13	1	0	-1	$\sqrt{2}$
2	1	0	0	1	8	-1	-1	0	$\sqrt{2}$	14	-1	0	1	$\sqrt{2}$
3	0	1	0	1	9	1	-1	0	$\sqrt{2}$	15	0	1	1	$\sqrt{2}$
4	0	-1	0	1	10	-1	1	0	$\sqrt{2}$	16	0	-1	-1	$\sqrt{2}$
5	0	0	1	1	11	1	0	1	$\sqrt{2}$	17	0	1	-1	$\sqrt{2}$
6	0	0	-1	1	12	-1	0	-1	$\sqrt{2}$	18	0	-1	1	$\sqrt{2}$

Table 4.1: Labeling of the 18-velocities. The 0-velocity is not shown. For each label i, the velocity vector and its speed are shown. All values are given in lattice units.

controls the rate of relaxation of the stress tensor. By this it as well regulates the shear viscosity

$$\mu = -\frac{1}{6}\rho(2/\lambda + 1). \tag{4.16}$$

For stability reasons λ has to be in the range $-2 < \lambda < 0$. The kinetic modes can also contribute to the post collision distribution but the eigenvalues of these modes were set to be 0 so they have no effect on the post collision distribution η_i^*. The post-collision distribution is given in terms of the mass-density ρ, the momentum-density $\mathbf{j}$ (or the velocity $\mathbf{u}$ and the updated post collision momentum flux Π^*)

$$\eta_i^* = \eta_i + \Omega_i(\eta) = a_0^{c_i}\rho + a_1^{c_i} j_\alpha c_{i\alpha} + a_2^{c_i}\Pi^*_{\alpha\beta} c_{i\alpha}\bar{c}_{i\beta} + a_3^{c_i}(\Pi^*_{\alpha\alpha} - 3\rho c_s^2). \tag{4.17}$$

The coefficients $a_n^{c_i}$ have their origin in the different length of the vectors $|\mathbf{c}_i|$, i.e. the absolute velocity needed to reach the neighbor cell in one time-step, depending whether it is a nearest neighbor or a diagonal neighbor. Those velocities are shown in Table 4.1. The equilibrium function used for the simulation now reads, written in the distribution space, as

$$\eta_i^{eq} = a^{c_i}\left[\rho + \frac{\mathbf{j}\cdot\mathbf{c}_i}{c_s^2} + \frac{\rho\mathbf{u}\mathbf{u} : (\mathbf{c}_i\mathbf{c}_i - c_s\mathbf{1})}{2c_s^4}\right] \tag{4.18}$$

The coefficients are given as $a^0 = \frac{1}{3}$,$a^1 = \frac{1}{18}$,$a^{\sqrt{2}} = \frac{1}{36}$. A further discussion of the equilibrium distribution will follow in the next chapter.

In case of the simpler L-BGK model, one does not need the transformation into the space of moments. However, to generate the equilibrium distribution the local mass density ρ and the local momentum $m_{1,2,3}$ are needed. The computational cost of the MRT model is moderate higher i.e., in theory a L-BGK model should be 18% faster [31]. The L-BGK model that is used in chapter 5 is used in further work and is well described in the literature [47, 102]. Since the differences between both codes is rather of technical nature than theoretical, I will not go into more details about the used L-BGK model. The advantage of the MRT model is the possibility to steer the bulk and shear viscosity independently. As well the numerical artefacts introduced by some boundary conditions is reduced. However the main advantage is the accessibility of the moments, which do carry the physical properties of the system, e.g. thermal fluctuations require a random noise on all modes [34].

4.2.4 From lattice Boltzmann to Navier-Stokes

After the presentation of the basic concept of the method it is now possible to show that such a simplified form of the Boltzmann equation will reproduce fluid behavior. In this case it should be possible to perform a Chapman Enskog procedure and derive the Navier-Stokes equations

$$\rho\left(\frac{\partial \mathbf{u}}{\partial t} + (\mathbf{u}\nabla\mathbf{u})\right) = -\Delta p + \mu\nabla\mathbf{u} + (\lambda+\mu)\nabla(\nabla\mathbf{u}), \tag{4.19}$$

which can also be written in components as

$$\partial_t j_a + \partial_\beta(\rho c_s^2\delta_{\alpha\beta} + \rho u_\alpha u_\beta)\partial_\beta = \sigma_{\alpha\beta}. \tag{4.20}$$

Einstein summation convention is in place, ∂_α stands for $\frac{\partial}{\partial\alpha}$, the $\delta_{\alpha\beta}$ denotes a Kronecker-δ. The viscous stress is given as

$$\sigma_{\alpha\beta} = \mu_{\alpha\beta\gamma\delta}\partial_\gamma u_\delta, \tag{4.21}$$

which in case of an isotropic fluid can be simplified by

$$\mu_{\alpha\beta\gamma\delta} = \mu(\delta_{\alpha\gamma}\delta_{\beta\delta} + \delta_{\alpha\delta}\delta_{\beta\gamma}) + \mu_v\delta_{\alpha\beta}\delta_{\gamma\delta} \tag{4.22}$$

with the shear viscosity μ and the bulk viscosity μ_v. We follow the standard asymptotic analysis [57], like it is described in [35, 34, 68] for the lattice Boltzmann method. At first one introduces a dimensionless scaling parameter $\epsilon \ll 1$ and writes

$$\mathbf{x}_1 = \epsilon\mathbf{x}. \tag{4.23}$$

The idea behind this is to introduce a coarse-grained spatial resolution. In the same way a coarse-grained time

$$t_1 = \epsilon t \tag{4.24}$$

is introduced. The reason to use the same ϵ for space and time is the wave-like propagation of sound waves. However, to cover the momentum diffusion a second coarse-grained time scale

$$t_2 = \epsilon^2 t \tag{4.25}$$

has to be introduced. Commonly ϵ is associated with the Knudsen number Kn that depicts the ratio of the mean free path of a molecule and the typical length scale of the system. Another equivalent definition would be that the Knudsen number is the ratio between the mean collision time of a molecule and the typical time scale of the hydrodynamic system. It is now possible to distinguish between the hydrodynamical short time scale $t_s = t_1/\epsilon$ and the hydrodynamical long time scale $t_l = t_2/\epsilon^2$. Note that both time scales t_l and t_s are implicitly large on the lattice scale, as it is the coarse-grained space. The hydrodynamic limit is reached for $\epsilon \to 0$ meaning that the lattice space becomes much smaller than the typical length scale. However, it was shown that even a few lattice nodes are sufficient to reproduce fluid mechanic behavior [81, 105]. In this "multi-time scale" analysis, the population density function η can be written in the coarse-grained coordinates

$$\eta_i \equiv \eta_i(\mathbf{x}_1, t_1, t_2) \tag{4.26}$$

and the proceeding of the algorithm by a time step $t \rightarrow t + \delta t$ can be written as $t_1 \rightarrow t_1 + \epsilon\delta t$ and $t_2 \rightarrow t_2 + \epsilon^2\delta t$. Thus, the LB-equation reads as

$$\eta_i(\mathbf{x}_1 + \epsilon t_1 \mathbf{c}_i, t_1 + \epsilon\delta t, t_2 + \epsilon^2\delta t) - \eta_i(\mathbf{x}_1, t_1, t_2) = \Omega_i \tag{4.27}$$

It is assumed that the population density is a slowly varying function of the coarse-grained variables $\xi = [\mathbf{x}_1, t_1, t_2]$. A Taylor expansion of Eq. 4.27 reads as

$$\eta_i(\xi + \delta\xi) = \eta_i(\xi) + \sum_k \frac{\partial \eta_i}{\partial \xi_k}\delta\xi_k + \frac{1}{2}\sum_{kl}\frac{\partial^2\eta_i}{\partial\xi_k\partial\xi_l} + ... \tag{4.28}$$

Since the collision operator $\Omega(\eta_i)$ depends on the distribution function η_i one has to take into account its ϵ dependence

$$\eta_i = \eta_i^{(0)} + \epsilon\eta_i^{(1)} + O(\epsilon^2) \tag{4.29}$$

$$\Omega_i = \Omega_i^{(0)} + \epsilon\Omega_i^{(1)} + \epsilon^2\Omega_i^{(2)} + O(\epsilon^3). \tag{4.30}$$

One can now apply the conservation laws that must hold independently of ϵ and therefore on any order k one concludes that

$$\sum_i \Omega_i^{(k)} = \sum_i \Omega_i^{(k)}\mathbf{c}_i = 0. \tag{4.31}$$

By collecting the different orders of ϵ and implementing these relations to Eq. 4.27 one obtains

$$\Omega_i^0 = 0, \tag{4.32}$$

$$(\partial_{t_1} + \mathbf{c}_i \cdot \partial_{\mathbf{x}_1})\eta_i^{(0)} = \frac{1}{\delta t}\Omega_i^{(1)}, \tag{4.33}$$

$$\partial_{t_2}\eta_i^{(0)} + \frac{\delta t}{2}(\partial_{t_1} + \mathbf{c}_i \cdot \partial_{\mathbf{x}_1})^2\eta_i^{(0)} + (\partial_{t_1} + \mathbf{c}_i \cdot \partial_{\mathbf{x}_1})\eta_i^{(1)} = \frac{1}{\delta t}\Omega_i^2. \tag{4.34}$$

Using Eq. 4.33 one can now eliminate the second $\eta_i^{(0)}$ in Eq. 4.34 so that

$$\partial_{t_2}\eta_i^{(0)} + \frac{1}{2}(\partial_{t_1} + \mathbf{c}_i \cdot \partial_{\mathbf{x}_1})(\eta_i^{*(1)} + \eta_i^{(1)}) = \frac{1}{\delta t}\Omega_i^{(2)}. \tag{4.35}$$

with $\eta_i^* = \eta_i + \Omega_i$ being the post collision population in direction $\mathbf{c}_i$. The equations above imply that the relaxation time scale of the collisions $t \sim \delta t$, the sound propagation $t \sim \delta t/\epsilon$, and the momentum diffusion $t \sim \delta t/\epsilon^2$, are separated and therefore it is possible to calculate the collision operator of a higher order from the lower order one. One can as well conclude that the zeroth order of the collision operator $\Omega_i^{(0)}$ does only depend on $\eta_i^{(0)}$. Further, Eq. 4.32 shows that $\eta_i^{(0)}$ is invariant under collisions and therefore has to be the equilibrium distribution η_i^{eq}. This implies that the equilibrium distribution should depend only on conserved quantities, namely the mass density ρ and the momentum density $\mathbf{j}$. Otherwise, the algorithm would conserve physically not conserved quantities. Since there is no contribution from higher orders to the mass density ρ and the momentum density $\mathbf{j}$ one can express these quantities in terms of the equilibrium function

$$\sum_i \eta_i^{eq} = \rho \tag{4.36}$$

and

$$\sum_i \eta_i^{eq} \mathbf{c}_i = \mathbf{j}. \tag{4.37}$$

This is concluded from the vanishing of the higher orders in mass and momentum density

$$0 = \rho^{(1)} = \rho^{(0)} ...$$

and

$$0 = \mathbf{j}^{(1)} = \mathbf{j}^{(2)} ...$$

The higher orders vanish because otherwise $\eta_i^{(0)}$ would have ϵ-dependent components which would contradict Eq. 4.32.

The dynamics of the LB-model on the longer time scales can now be gained by analysing the moments of Eq. 4.33 and Eq. 4.35 with respect to the discrete velocity set $\mathbf{c}_i$. From the previous chapter we know that the moments are carrying the physical properties, so their dynamics are the point of interest. Hereby some conditions towards the collision operator Ω_i become obvious. From the zeroth moment of Eq. 4.33 one obtains the continuum equation on the time scale t_1:

$$\sum_i (\partial_{t_1} + \mathbf{c}_i \cdot \partial_{\mathbf{x}_1}) \eta_i^{(0)} = \sum_i \frac{1}{\delta t} \Omega_i^{(1)} = \tag{4.38}$$

$$\partial_{t_1} + \partial_{\mathbf{x}_1 \alpha} j_\alpha = 0 \tag{4.39}$$

and incompressibility on the time scale t_2

$$\begin{aligned} \sum_i \left[\partial_{t_2} \eta_i^{(0)} + \frac{1}{2} (\partial_{t_1} + \mathbf{c}_i \cdot \partial_{\mathbf{x}_1}) (\eta_i^{*(1)} + \eta_i^{(1)}) \right] &= \sum_i \frac{1}{\delta t} \Omega_i^{(2)} = \\ \partial_{t_2} \rho + \sum_i \frac{1}{2} (\partial_{t_1} + \mathbf{c}_i \cdot \partial_{\mathbf{x}_1}) (\eta_i^{*(1)} + \eta_i^{(1)}) &= 0 = \\ \partial_{t_2} \rho &= 0 \end{aligned} \tag{4.40}$$

Here one uses the condition that the collision operator may not change mass and momentum density, and therefore each order of the collision operator $\Omega^{(n)} = 0$ may not change the mass and momentum density. The first moment gives us the momentum conservation. Starting with Eq. 4.33 on the first time scale t_1

$$\begin{aligned} \sum_i \mathbf{c}_i \left[(\partial_{t_1} + \mathbf{c}_j \cdot \partial_{\mathbf{x}_1}) \eta_i^{(0)} \right] &= \sum_i \mathbf{c}_i \frac{1}{\delta t} \Omega_i^{(1)} = \\ \partial_{t_1} \mathbf{j} + \partial_{\mathbf{x}_1} \sum_i \mathbf{c}_i \mathbf{c}_j \eta_i^0 &= 0 \end{aligned} \tag{4.41}$$

and writing this in components $c_{i\alpha}$ and with the momentum flux

$$\Pi_{\alpha,\beta} = \sum_i \eta_i c_{i\alpha} c_{i\beta}$$

one can write the momentum as

$$\partial_{t_1} j_\alpha + \partial_{\mathbf{x}_1} \beta \Pi_{\alpha\beta}^{(0)} = 0. \tag{4.42}$$

On the time scale t_2 the momentum reads as

$$\begin{aligned}\sum_i \mathbf{c}_i \left[\partial_{t_2}\eta_i^{(0)} + \frac{1}{2}(\partial_{t_1} + \mathbf{c}_j \cdot \partial_{\mathbf{x}_1})(\eta_i^{*(1)} + \eta_i^{(1)})\right] &= \sum_i \mathbf{c}_i \frac{1}{\delta t}\Omega_i^{(2)} = \\ \partial_{t_2}\mathbf{j}^{(0)} + \frac{1}{2}\left(\partial_{t_1}(\mathbf{j}^{*(1)} + \mathbf{j}^{(1)}) + (\sum_i \mathbf{c}_i\mathbf{c}_j\partial(\eta_i^{*(1)} + \eta_i^{(1)})\right) &= 0, \end{aligned} \tag{4.43}$$

with $j^{(1)} = 0$ and the definition of the momentum flux Π and written in components

$$\partial_{t_2} j_\alpha + \frac{1}{2}\partial_{\mathbf{x}_1\beta}\left(\Pi_{\alpha\beta}^{*(1)} + \Pi_{\alpha\beta}^{(1)}\right) = 0. \tag{4.44}$$

To reproduce the Navier Stokes equation 4.20 one needs to rewrite Eq. 4.42 and Eq 4.44 as a combination in terms of the lattice-scale coordinates $\mathbf{x} = \mathbf{x}_1/\epsilon$, $t = t_1/\epsilon = t_2/\epsilon^2$. By using ∂_α as component of $\partial_{\mathbf{x}}$ one gets for the spatial derivatives

$$\partial_\alpha = \epsilon\partial_{\mathbf{x}_1\alpha}$$

and for the time derivative

$$\partial_t = \epsilon\partial_{t_1} + \epsilon^2\partial_{t_2}.$$

Mass and momentum density in a combination reads on the lattice spacing as

$$\partial_t\rho + \partial_\alpha j_\alpha = 0, \tag{4.45}$$

$$\partial_t j_\alpha + \partial_\beta\Pi_{\alpha\beta}^{(0)} + \frac{1}{2}\partial_\beta\left(\Pi_{\alpha\beta}^{*(1)} + \Pi_{\alpha\beta}^{(1)}\right) = 0. \tag{4.46}$$

Looking at Eq. 4.46 it is possible to identify the different terms in the Navier-Stokes equation 4.20

$$\partial_t j_\alpha + \partial_\beta(\rho c_s^2\delta_{\alpha\beta} + \rho u_\alpha u_\beta) = \partial_\beta\sigma_{\alpha\beta}$$

The time derivative $\partial_t j_\alpha$ is obvious. Further, $\Pi_{\alpha\beta}^{(0)}$ is the equilibrium momentum flux $\Pi_{\alpha\beta}^{eq}$ and therefore unchanged by the collision operator and does depend only on ρ and $\mathbf{j}$. Therefore, it can be identified as the Euler stress

$$\Pi_{\alpha\beta}^{(0)} = \Pi_{\alpha\beta}^{eq} = \rho c_s^2\delta_{\alpha\beta} + \rho u_\alpha u_\beta. \tag{4.47}$$

Here the ideal gas equation of state is implemented in the code (c.f. Eq. 4.14). All that is left is to identify the remaining non-equilibrium part with the viscous stress

$$\frac{1}{2}\left(\Pi_{\alpha\beta}^{*(1)} + \Pi_{\alpha\beta}^{(1)}\right) = -\sigma_{\alpha\beta}, \tag{4.48}$$

which leads under the postulation of an isotropic liquid and with the definition from Eq 4.15 to a shear viscosity of

$$\mu = \rho c_s^2\delta t\left(\frac{1}{\lambda} + \frac{1}{2}\right) \tag{4.49}$$

and a bulk viscosity of

$$\mu_v = \rho c_s^2\delta t\left(\frac{2}{3\lambda_v} + \frac{1}{3}\right). \tag{4.50}$$

Since the time step δt is the natural time unit of the method it is commonly set to 1 and is not written in a lot of publications. The same applies for the distance between two lattice sites or the volume of one lattice node. For other collision operators or equilibrium functions several steps of this Chapman Enskog procedure have to be redone in an analogue way. Further, one can impose non ideal equations of state or fluctuations, which makes the analysis more complicated. However, one can see that the conservation of mass and momentum is inherently included in the lattice Boltzmann scheme and one only has to make sure that the viscous damping is done in a correct way.

4.2.5 External forces

External forces $\mathbf{f}$ are crucial to simulate fluid flow. In principal an external force changes the momentum of the fluid so one could naively just add it to the momentum $\mathbf{j}_{\text{new}} = \mathbf{j}_{\text{old}} + \mathbf{f}\delta t$ in every time step δt. In the lattice Boltzmann scheme with discrete time this would rise the question at which time one has to add the forces or if it can be done at any time. Therefore, it is useful to see the external forces as an additional collision operator Ω', so the lattice Boltzmann equation reads as

$$\eta_i^* - \eta_i = \sum_j L_{ij}(\eta_j - \eta_j^{eq}) + \Omega_i'. \tag{4.51}$$

The additional collision operator Ω' may not change the mass

$$\sum_i \Omega_i' = 0, \tag{4.52}$$

but has to change the momentum

$$\sum_i \Omega' \mathbf{c}_i = \delta t \mathbf{f}. \tag{4.53}$$

A consequence of this is that the momentum $\mathbf{j}$ is not any longer unique and any value between $\sum_i \mathbf{c}_i\eta_i$ and $\sum_i \mathbf{c}_i\eta_i + \delta t\mathbf{f}$ could be correct. However, it was shown that a wrongly assumed force could lead to unphysical behavior like negative permeabilities in porous-media [100]. Numerical [80] and theoretical [145] analysis have shown that the optimum value is the arithmetic mean of pre and post collision momentum. Therefore, one **defines** the momentum density as

$$\mathbf{j} = \sum_i \mathbf{c}_i\eta_i + \mathbf{f}\frac{\delta t}{2}. \tag{4.54}$$

This has two consequences. First one has to keep this in mind when creating an output of the velocity. The second is that one needs the right flow velocity to construct the equilibrium function η^{eq}, so that the equilibrium momentum density is equal to the defined one

$$\sum_i \eta_i^{eq}\mathbf{c}_i = \mathbf{j}, \tag{4.55}$$

but the non-equilibrium part does not include the momentum change so that,

$$\sum_i \eta_i^{neq}\mathbf{c}_i = -\mathbf{f}\frac{\delta t}{2}. \tag{4.56}$$

If one would leave out the latter term and would just impose $\sum_i \eta_i^{neq} \mathbf{c}_i = 0$ as done in [145] one would add a small error of order f^2 to the distribution. This leads to spurious terms in the Chapman-Enskog analysis, like a force dependent viscosity. This might become important in the case of strongly inhomogeneous forces but the differences vanish in the low Reynolds number limit. To be consistent with the force-free case, one needs to adapt the relaxation of the non-equilibrium momentum flux in such a way that the resulting viscosity is the same as in the force free case. The resulting additional force collision operator with $c_{i\alpha} = \mathbf{c}_i \cdot \mathbf{e}_\alpha$ then reads as

$$\Omega' = a^{c_i} \left[\frac{\delta t}{c_s^2} f_a c_{i\alpha} + \frac{\delta t}{2c_s^4} \Sigma_{\alpha\beta} (c_{i\alpha} c_{i\beta} - c_s^2 \delta_{\alpha\beta}) \right], \tag{4.57}$$

with $\Sigma_{\alpha\beta}$ containing the adaption of the non-equilibrium momentum flux. In the code this is realized by adding half the force to the momentum then calculate the equilibrium distribution in the momentum space, relax the moments towards this equilibrium and in the end add the remaining half of the force $\frac{\mathbf{f}}{2}$ and the momentum flux correction

$$c_{\alpha\beta} = \frac{1+\lambda}{2\rho} (j_\alpha f_\beta + j_\beta f_\alpha) \tag{4.58}$$

to the corresponding moments.

4.2.6 Multi-phase models in lattice Boltzmann

One strength of the lattice Boltzmann method is the possibility to implement multi-phase and multi-component flow. For clarification the two cases will be distinguished in this thesis as follows. Multi-component flow should be flow that contains many (usually two) distinguished liquids with potentially different chemical properties like water and oil. Multi-phase (usually two phase) flow is a flow with distinguishable phases of the same component like liquid and vapor. It should be noted that for this work the actual phase transition is not of interest and a two phase model is used to simulate bubbles attached to a surface or to model the wetting behavior of the boundary.

The Oxford model

The Oxford or free energy model was developed by Swift, Osborn and Yeomans [134, 133]. The main idea of the model is to have a well defined isothermal equation of state and force the system to equilibrate towards the desired state. Therefore, one defines a free energy as that of a van der Waals fluid

$$\Psi[\rho] = \int \left[\frac{k}{2} |\nabla \rho(\mathbf{r})|^2 + \psi(\rho(\mathbf{r}, T)) \right] dr, \tag{4.59}$$

with $\psi(\rho, T)$ being the bulk free-energy density at temperature T

$$\psi(\rho, T) = \eta T \ln \left(\frac{\rho}{1 - \rho b} \right) - a\rho^2 \tag{4.60}$$

while the second term gives the free-energy contribution from the density gradients in an inhomogeneous system. $\rho = \sum_i \eta_i$ indicates the number of particles. Here, a is a measure for the attraction between the particles and b is the excluded volume.

With this free energy one is now able to construct an equilibrium distribution function η_i^{eq} that does not have an ideal gas equation of state. Therefore, the pressure tensor is related to the free energy

$$P_{\alpha\beta}(\mathbf{x}) = p(\mathbf{x})\delta_{\alpha\beta} + \kappa \frac{\partial \rho}{\partial x_\alpha}\frac{\partial \rho}{\partial x_\beta}, \tag{4.61}$$

with

$$p(\mathbf{x}) = p_0 - \kappa\eta\nabla^2\rho - \frac{\kappa}{2}|\nabla\rho|^2, \tag{4.62}$$

where

$$p_0 = \rho\frac{d\psi(\rho)}{d\rho} - \psi(\rho)$$

is the equation of state of the fluid. The actual equilibrium function depends on the type of lattice and collision operator. Since the equation of state is forced on the system from top one calls such a method a top down method. In the same way one can find a free energy for a two component model or for the fluid-boundary interaction. Besides the studies of phase separation, Varnik et al. used such a model to investigate the behavior of droplets on a surface [46].

The Shan-Chen model

Instead of imposing an equation of state and force the system towards it, it is possible to introduce an internal force that models the intermolecular interactions. Such a model was developed by Shan and Chen [124, 125, 126]. This force should simulate the long range interactions between the particles. Therefore, one considers at a system with S components and defines a potential of the form

$$V(\mathbf{x}, \mathbf{x}') = \sum_{\sigma}^{S}\sum_{\bar{\sigma}}^{S} G_{\sigma\bar{\sigma}}(\mathbf{x}, \mathbf{x}')\Psi^{\sigma}(\rho^{\sigma}(\mathbf{x}))\Psi^{\bar{\sigma}}(\rho^{\bar{\sigma}}(\mathbf{x}')) \tag{4.63}$$

where ρ^{σ} and $\rho^{\bar{\sigma}}$ are the number density of component σ and $\bar{\sigma}$. Since the distance between two lattice points is fixed the number density determines the average particle particle distance. Therefore, the potential is made to be the product of the local so-called effective masses $\Psi^{\sigma}(\rho^{\sigma})$ which are a function of the local densities ρ^{σ} only. The exact form of Ψ is discussed latter. It determines the detailed interaction and the equation of state. The strength of the interaction is controlled by the Greens function $G_{\sigma\bar{\sigma}}(\mathbf{x}, \mathbf{x}')$. In case of a homogeneous system this is reduced to $G_{\sigma\bar{\sigma}}(|\mathbf{x} - \mathbf{x}'|)$. In case one takes into account only nearest and next nearest-neighbours one can reduce the Greens function in a one component system to a single number g. In case of a multi-component system one needs a symmetric tensor $g_{\sigma\bar{\sigma}}$ to steer the interaction between each component. Depending whether $g_{\sigma\bar{\sigma}}$ is positive or negative the interaction is repulsive or attractive. From the potential one can now derive a local force

$$\mathbf{f}^{\sigma\bar{\sigma}} = \Psi^{\sigma}(\rho^{\sigma}(\mathbf{x}))g_{\sigma\bar{\sigma}}\sum_i \mathbf{c}_i\Psi^{\bar{\sigma}}(\rho(\mathbf{x} + \mathbf{c}_i)). \tag{4.64}$$

This force can now be included in a similar manner as external forces in the previous section. Note that the force does not conserve the local momentum but in total no momentum change is induced due to the symmetry of $g_{\sigma\bar{\sigma}}$. Shan and Chen showed by performing a Chapman Enskog procedure that in case of a one component system one can reproduce a Van der Waals like equation of state [124]. Here, it has to be noted that their analysis was done on a different lattice Boltzmann model than the two ones that are used in this thesis. However they showed that an effective mass of

$$\Psi(\rho) = 1 - e^{-\frac{\rho}{\rho_0}}, \tag{4.65}$$

with the reference density ρ_0 can produce a non-monotonic pressure in dependence of ρ. Therefore, a negative $\frac{dp}{d\eta}$ appears in the equation of state, which corresponds with a thermodynamic instability and the system segregates into a dense (liquid) and a light (gas) phase. However, typical density ratios between the dense and the light phase are $\frac{\rho_{\text{dense}}}{\rho_{\text{light}}} = 40$, so they are still far away from the ratio in real systems where a typical density ratio would be $\frac{\rho_{\text{dense}}}{\rho_{\text{light}}} = 1000$.

Nevertheless, one can achieve a phase separation between two components like water and oil. To do so one needs an equilibrium function that includes the combined velocities of both species. The interaction Eq. 4.64 has the same form as for one component but instead of $g_{\sigma\sigma}$ one needs the non diagonal parts of $g_{\sigma\bar{\sigma}}$. Since one has only two components and one needs the symmetry this simply reads as a single value g_{ow} which steers the interaction between the two species. Later it is shown that such a force can as well be used to describe the wetting behavior of a solid boundary.

4.2.7 Solid-fluid boundary conditions

To simulate fluid flow in the presence of any solid object one needs to define boundary conditions at the interface between them. Further, it is a challenging task to implement moving objects in a fluid solver like it has to be done for the simulation of the AFM based slip experiments. In the lattice Boltzmann scheme, finding a boundary condition means to find unknown population densities η_i that are not defined because prior to the collision step they are lacking corresponding neighbors. This is depicted in Fig. 4.2 for a D2Q9 model.

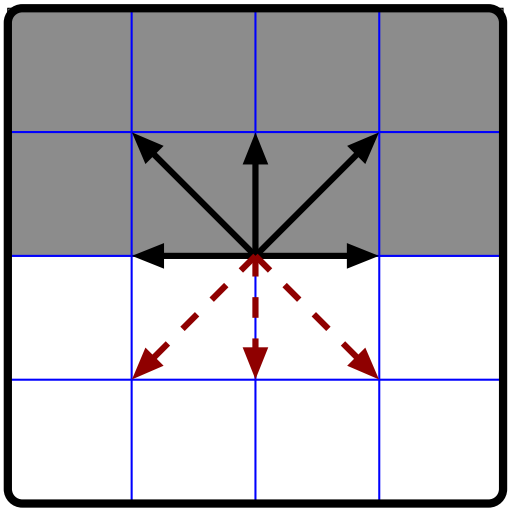

Figure 4.2: Boundary node on the top row of a grid. The gray region, located outside the simulated fluid volume, does not participate in the simulation. Population densities η_i on the boundary node are represented by their lattice vectors. The dashed vectors stand for unknown populations.

This problem does not occur in the case of periodic boundary conditions. Here it is easy to gain the "unknown" population densities since one simply has to identify the "outgoing" population densities with the incoming ones $\eta_i(x_{\max}) = \eta_i(0)$ and vice versa. At solid surfaces this is more complicated since here one needs to find new populations on the boundary nodes that are consistent with the dynamics of the method and satisfy the desired macroscopic behavior. Besides the implementation of hydrophobic slip surfaces the general fluid-surface boundary condition is no-slip

$$\mathbf{u}(x = 0) = \mathbf{v}_{\text{boundary}}$$

saying that the velocity of the fluid at the boundary is the same as the one of the solid, which is 0 in case of a non-moving boundary like it is usually assumed. Since a wrong implementation of the boundary condition can cause serious errors a lot of analyses have been done on the different types of boundary conditions [85, 68, 52].

Bounce-back boundary condition

A very simple but effective way of implementing a no-slip boundary condition is the so-called bounce back rule. Here, every population is reflected back to the boundary node it is coming from (c.f. Fig. 4.3)

$$\eta(\mathbf{x}_b, -\mathbf{c}_i) = \eta(\mathbf{x}_b, \mathbf{c}_i), \tag{4.66}$$

for all $\mathbf{x}_b + \mathbf{c}_i$ being on a boundary node. By this procedure the density is transferred to the original boundary node in the next advection step.

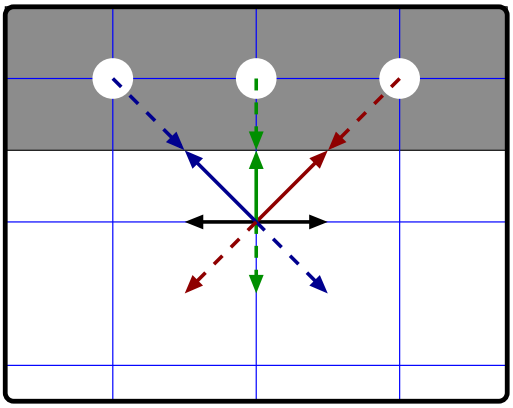

Figure 4.3: Scheme of the bounce back rule. The population densities η_i that are unknown are set to the same value as the population density that points to the boundary node from where the population should come from. The dashed arrows indicate the values that are set by this rule, thus same color indicates the same value.

It has to be noted that the hydrodynamic boundary created by this procedure is not on the boundary node itself but between the boundary node and the closest fluid node. In addition, the actual position of the hydrodynamic boundary depends on the relaxation rate $\lambda = \frac{-1}{\tau}$ and therefore on the viscosity. One can show that in case of a BGK model and $\tau \approx 1$ the boundary position is right in the middle between the fluid and the boundary node [52]. However, the shift of the boundary position is proportional to the square of the relaxation time τ^2. In case of a MRT model one can tune the relaxation of the non hydrodynamic nodes in such a way that the divergence of the boundary position scales only linearly with τ. Beside its simplicity the bounce back method gives the direct possibility to access the momentum transfered by the fluid towards the boundary since it is given by the sum over all reflected population densities

$$\mathbf{j}_{\text{transfered}} = \sum_{\text{surface}} \mathbf{c}_i \eta_i^{\text{reflected}} \delta t. \tag{4.67}$$

A further advantage is that it can be implemented straight forward for arbitrarily shaped surfaces since one only needs to bounce back those population densities η_i which end up inside the boundary[1]. Due to the intermediate boundary position and the lattice structure it is in case of arbitrarily shaped surfaces not possible to determine the exact hydrodynamic boundary position analytically so one either needs an estimate or a numerical test, e.g. one can determine the effective radius of a sphere by measuring the Stokes force acting on it. However those deviations are small and can be well controlled.

Moving boundaries

When simulating moving particles in the fluid it is necessary to implement moving boundaries. In this case the velocity of the fluid at the boundary should not be zero

[1]Since all surfaces in this method consist of lattice notes on a cubic lattice, the geometries in the lattice Boltzmann method are often referred to as Lego world [129].

compared to the lattice but be the velocity of the boundary. In the given simulation this is realized by a generalization of the bounce back boundary condition, which takes into account the momentum of the moving object. The method was developed by Ladd et al. and described extensively in the literature [145]. The picture one should have in mind is that an ensemble of particles moving with the velocity $\mathbf{c}_i$ is hitting a perpendicular wall which is moving with velocity $v_b \ll c_i$. After the particles hit the wall their velocity is $-\mathbf{c}_i + 2\mathbf{v}_b$ and the force exerted on the wall is proportional to $\mathbf{c}_i - \mathbf{v}_b$. Since the velocities in the lattice Boltzmann scheme are discrete, such a scheme cannot be implemented directly but one has to modify the density of the bounced back particles such that the transfered momentum equals the same as in the continuous case.

At first one takes into account those population densities $\eta(\mathbf{x}_b, \mathbf{c}_b, t)$ close to the boundary of the object for those $\mathbf{c}_b$ that $\mathbf{x}_b + \mathbf{c}_b\delta t$ is a solid node. This is the same as in the normal bounce back method. One now defines a simple rule for the unknown "bounced back" particles $\eta(\mathbf{x}_b, -\mathbf{c}_b, t + \delta t)$ that takes into account the movement of the boundary

$$\eta(\mathbf{x}_b, -\mathbf{c}_b, t + \delta t) = \eta^*(\mathbf{x}_b, \mathbf{c}_b, t) - \frac{2a^{\mathbf{c}_b}\rho\mathbf{v}_b \cdot \mathbf{c}_b}{c_s^2}. \tag{4.68}$$

$\eta^*(\mathbf{x}_b, \mathbf{c}_b, t)$ is the post collision distribution population. The local velocity of the surface is $\mathbf{v}_b$, which takes into account the center of mass velocity and the angular velocity of the particle. However, in the cases that are of interest in this thesis the angular velocity is kept to 0 so that $\mathbf{v}_b$ is the center of mass velocity of the object. The force acting on the object can be calculated from the total momentum exchange between the fluid and all of its boundary nodes.

Due to the lattice nature of the lattice Boltzmann method one needs to place particles on the grid. Therefore, the shape of the particle is estimated by the lattice nodes that are mainly inside the particle. Such an approximation seams very rough but even at small radii like 2.5 lattice units, the error in the hydrodynamic interaction can be kept within 1% of an exact numerical solution [22]. This will be validated latter in this thesis.

Particle motion

The movement of the particles themselves is realized like in a molecular dynamics (MD) simulation, i.e., one calculates the forces acting on the particle and changes its velocity afterwards. In contrast to a classical MD simulation the force is not coming from pairwise potentials but from the hydrodynamic interaction. The implementation of such potentials would be straightforward but so far only a hard sphere potential between particles is implemented. Further, it should be noted that the velocity in the presented simulations is kept constant by setting the mass of the particle to infinity. The infinite mass is important for the force measurement because in this case the velocity in Eq. 4.68 is $\mathbf{v}_b(t + \frac{\delta t}{2})$ as it is used in the underlying velocity Verlet integration[2]. One has to make sure that $\mathbf{v}_b(t + \frac{\delta t}{2})$ is constant even if a force acts on the sphere. After the center of mass movement is calculated one might have to change the occupied lattice nodes. This update of nodes is not a

[2]sounds easy but can cost you one year...

continuous motion but a discrete jumping over the lattice. Due to this jumping the flow field (and therefore the forces) around the particles need some time to come to an quasi-equilibrium. For the practical use this means that one has to average forces over several time steps. Further, it limits this method to low Mach numbers, since one should change the boundary node configuration only after one has a well averaged value for the given configuration. However, the equilibration takes only about 10 time steps so that this condition is relatively easy to be fulfilled.

Hydrophobic boundaries

It is known from MD-simulations that the interaction between the boundary and the fluid causing a slip phenomenon usually takes place within a few molecular layers of the liquid along the boundary surface [136, 135, 71, 23, 72, 24, 5].

The implementation of solid hydrophobic boundaries contains two parts. Since such a boundary consists of a solid wall one implements a bounce back boundary condition. The second part covers the hydrophobic interaction between the boundary and the fluid. It is realized in the same way as the interaction between two components in a multi-component system (c.f. the previous section). In our case a Shan Chen like force f_{wf} between the fluid nodes close to the boundary and the boundary nodes itself is implemented. Such a force reads as

$$f_{wf}(\mathbf{x}) = \Psi^{\text{fluid}}(\mathbf{x}) \sum_i \mathbf{c}_i g_{wf} \Psi^{\text{wall}}(\mathbf{x} + \mathbf{c}_i). \tag{4.69}$$

The force is in full analogy to Eq: 4.64. The effective mass of the boundary $\Psi^{\text{wall}} = 1 - \exp(-\rho^{\text{wall}}/\rho_0)$ is a local parameter that indicates how strong the local hydrophobic interaction is while g_{wf} is a global coupling parameter. It is as well possible to assign a virtual "fluid density" to a boundary node. By this one can use a one component multi-phase Shan Chen model to simulate the solid-fluid interactions and a possible phase-transition close to the boundary as it happens at super-hydrophobic surfaces.

Further, a hydrophobic interaction like the presented one can be utilized to model apparent slip [48, 76, 49, 117]. Due to the repellent hydrodynamic force, a depletion layer close to the boundary is formed where the fluid density ρ and therefore the viscosity μ is reduced. This viscosity reduction finally leads to apparent slip. The dependences are discussed in section 4.2.8.

Alternative boundary conditions

Besides the presented boundary conditions there are many other possible implementations. Most of them have a higher precision than the simple bounce back rule but might have to take into account more boundary nodes, which makes them non-local, or they are not able to handle arbitrary geometries. Further, not all proposed boundary conditions can be applied on a 3D lattice. An overview over different boundaries was recently published by Latt et al. [85].

One possible solution is to create the missing populations by assuming that they follow the equilibrium distribution with the given velocity. In this case one still has to find a corresponding pressure (or density) at the close boundary nodes [62].

Latt and Chopard [84] proposed a "regularized method". The basic idea is to keep the non-equilibrium momentum flux Π^{neq} but regulate the velocity. Therefore, Π^{neq} is calculated utilizing the bounced back densities. The equilibrium parts Π^{eq} of the population density $\eta(\mathbf{x}_b)$ are determined in such a way that they correspond to the correct velocity at the boundary.

Other methods use a finite difference scheme to obtain the non-equilibrium stress from the neighboring lattice nodes [127]. Such an approach needs non-local information which makes it less efficient when it comes to parallelization.

Slip boundary conditions could be generated in different ways as well. The most common one is a so-called spectral bounce back scheme [129]. The idea behind this method is the same as for the Maxwell [96] theory for rarefied gases close to a boundary (c.f. Eq. 3.7). For the lattice Boltzmann scheme not all the incoming population densities η_i are bounced back to where they came from but only a fraction $\eta_i(1-p)$. The remaining density $\eta_i p$ is reflected, thus in summation it is similar to the moving boundary condition where the bounced back density is reduced or increased by a factor proportional to the boundary velocity. By this method one creates a shear independent slip velocity.

Another possibility is to change the relaxation time (and therefore the viscosity) close to the boundary. By such a scheme one generates again a low viscosity layer but with the same density and the same pressure [106].

4.2.8 Poiseuille flow

The lattice Boltzmann method was facing some criticism. It can be shown that the boundary conditions might lead to some slip phenomena where this is not desired. Further, it is necessary to understand the dependencies of the used slip model as it was presented [75, 48]. In those publications the slip was determined by fitting a Poiseuille flow profile

$$u_x(y) = \frac{1}{2\mu}\frac{\partial P}{\partial x}\left[d^2 - y^2 - 2d\beta\right] \tag{4.70}$$

between two infinite walls that are at a distance $2d$, via the slip length β. The flow can be generated either by a body force or by applying a pressure gradient $\frac{\partial P}{\partial x}$. The latter is realized by setting all population densities η_i on the in and out flow nodes to a fixed value. A typical flow profile of such a simulation can be seen in Fig. 4.4. Symbols show the simulation data, the line for the no slip curve is an exact analytical solution while the curve for the slip case is a fit with the slip length $\beta = 1.33$. In this case the flow is generated by an constant body force $f = 10^{-6}$ and the viscosity is set to 0.1. All values are given in lattice units if not stated otherwise.

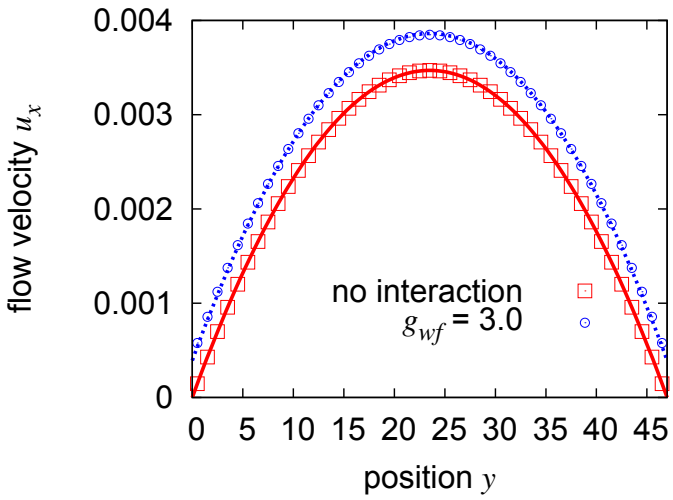

Figure 4.4: A typical flow profile $u_x(y)$ in a Poiseuille flow with no-slip and slip boundary condition. Symbols show the simulation data. The doted line is a best fit via the slip length $\beta = 1.33$ and the solid red line is the analytic no slip solution.

A Poiseuille setup was used to investigate the dependency of the slip length on different parameters [48]. To conclude this work it can be said that the slip length is independent of the flow velocity over several orders of magnitude and therefore independent of the shear rate. The slip length grows exponentially with the interaction parameter g_{wf} but due to the truncation of the effective mass Ψ has only limited influence on the slip length. Further, the slip length depends on the bulk pressure (or bulk density). The reason for this is that there is a force equilibrium in the depletion layer. The pressure from the bulk has to be equal to the pressure in the layer plus the hydrophobic interaction. Thus, the depletion layer pressure and therefore its viscosity depends on the bulk pressure. The maximum achievable slip length is $\beta_{max} = 5$ lattice units. Larger slip length are not possible because of computational instabilities. In this case some population densities η_i close to the boundary could become negative, which causes the code to fail. In addition, the stability of the code at slip length higher than $\beta > 3$ is very critical and needs a fine tuning of the parameters.

Chapter 5

Poiseuille flow over rough surfaces

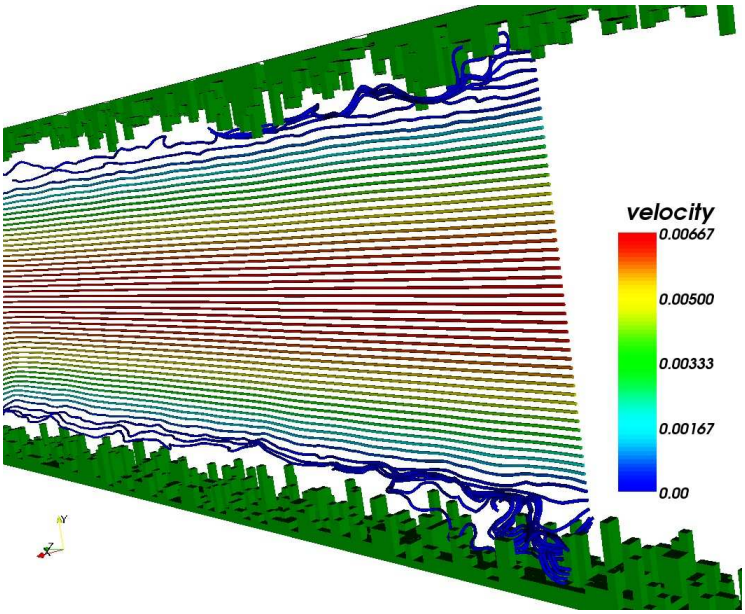

Figure 5.1: Visualisation of the geometry and the simulated streamlines for a typical system with a random-height roughness. The colors of the streamlines indicate the flow velocity. Between the roughness elements the flow-field is highly influenced by the boundary profile, however, outside it rapidly relaxes towards a normal Poiseuille flow.

Surface roughness becomes a relevant parameter if typical length scales of a system are comparable to the topographical variations as it can be the case in microfluidic setups. Here, an apparent slip is often detected which can have its origin in the misleading assumption of perfectly smooth boundaries. In this chapter the concept of an "effective no-slip plane" at an intermediate position between peaks and valleys of the surface, is introduced. The averaged flow behaves such as in a channel with a no slip boundary condition located at this virtual flat surface.

As first system, LB-Simulations of Poiseuille flow over rough surfaces, as depicted in Fig. 5.1, are performed. After introducing the setup a comparison with the analytical results by Panzer et al. is given. Finally, different surface geometries and their effective boundary positions are discussed. It is also shown that a few small

peaks can have a large influence on the effective boundary position. Parts of the presented data and results have been published in [74, 76, 49].

A Poiseuille setup is chosen since it is an easy model for an micro-channel as they are used in most micro-PIV experiments. Some the basic ideas for this thesis are already derived in such a setup but latter the more complex lubrication force measurement will follow.

5.1 The setup

In this chapter Poiseuille flow between two infinite rough boundaries as, depicted in Fig. 5.1, is modeled. Simulation lattices are 512 lattice nodes long in flow direction and the channel walls are separated by 128 nodes between the lowest points of the roughness elements $r_{\min}$ as illustrated in Fig 5.2. Periodic boundary conditions are imposed in the remaining direction allowing it to keep the resolution as low as 16 lattice units. A pressure gradient is obtained by setting the pressure to fixed values at the in- and outflow boundary. The local roughness height is $r(\mathbf{x})$. The height of the roughness r is defined as its highest point, while the average roughness is given by $r_{\text{av}} = \frac{1}{A}\int_A r(\mathbf{x})dA$, with A being the projected wall surface. Due to the discretization the integral can be calculated as a summation. All values are measured from the lowest point of the roughness $r_{\mathbf{min}} = 0$. In the case of symmetrical distributions the average roughness is $r_{\text{av}} = r/2$.

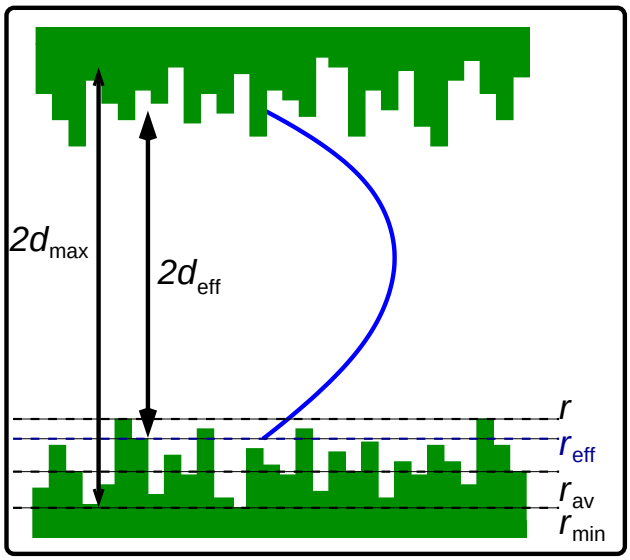

Figure 5.2: The effective boundary height r_{eff} is found to be located between the deepest valley at $r_{\min}$ and the highest peak at r. It corresponds to an effective channel width d_{eff}. For most geometries in this chapter the average roughness is equal to half the maximum height and therefore $r_{\text{av}} = r/2$. The maximum distance between the plates $d_{\max}$ is kept constant at 128 lattice sites.

An effective boundary position can be found by fitting the parabolic flow profile

$$u_x(y) = \frac{1}{2\mu}\frac{\partial P}{\partial x}\left[d^2 - y^2 - 2d\beta\right] \tag{5.1}$$

via the distance $d = d_{\text{eff}}$. With β set to 0 the no-slip case is obtained. The viscosity μ and the pressure gradient $\frac{\partial P}{\partial x}$ are given by the simulation. To obtain an average value for d_{eff}, a sufficient number of individual profiles at different positions z are taken into account. In case of a periodic roughness this corresponds to one complete period. Alternatively, the mass flow $\int u(x)\rho\,\mathrm{d}x$ can be computed and compared with the theoretical value to obtain d_{eff}. Both methods are equivalent and result in identical positions d_{eff} of the effective boundary. The effective height r_{eff} of the surface roughness is given by $r_{\text{eff}} = (d_{\max} - d_{\text{eff}})/2$ (c.f. Fig. 5.2).

5.1.1 Description of roughness

Four different types of topography with an average roughness of $r_{\text{av}} = r/2$ are used in this chapter. Three of the surfaces consist of periodic, transverse stripes, as illustrated in Fig. 5.3 for a square cross-section. The remaining surface displays a random or uncorrelated topography.

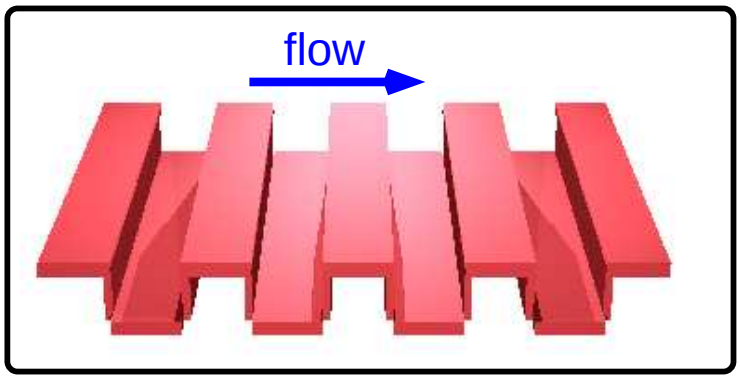

Figure 5.3: A picture of the square cross-section roughness.

The periodically rough surfaces have different cross-sections that are illustrated in Fig. 8.4. The cosine-shaped boundaries are given by $r(x) = r/2 + r/2\cos(qx)$, squares have a height of r and are separated by r lattice sites. Triangular structures are $2r$ wide and r high as is shown in Fig. 8.4. Random surface structures are created by choosing for every lattice position of the boundary the roughness height $r(x)$ as a random integer between 0 and r. For determining r_{eff} in such a geometry the single flow profiles of 5 surfaces generated with different sequences of uniformly distributed random numbers are averaged. All walls are geometrically similar, i.e., the effective height r_{eff} scales linearly with $r_{\max}$. The average height of such a distribution is $r_{\max}/2$ and the root mean square roughness is given by $r_{RMS} = 1/6\sqrt{3(r_{\max}+2)r_{\max}}$.

5.1.2 Validation of the simulation method

Panzer et al. analytically calculated the slip length β for Poiseuille flow with rough walls by performing a Fourier expansion of the streaming function Ψ containing the solution of the Navier-Stokes equations in the laminar case [108]. Ψ is obtained by a Fourier expansion of the boundary surface and the pressure field. Its solution

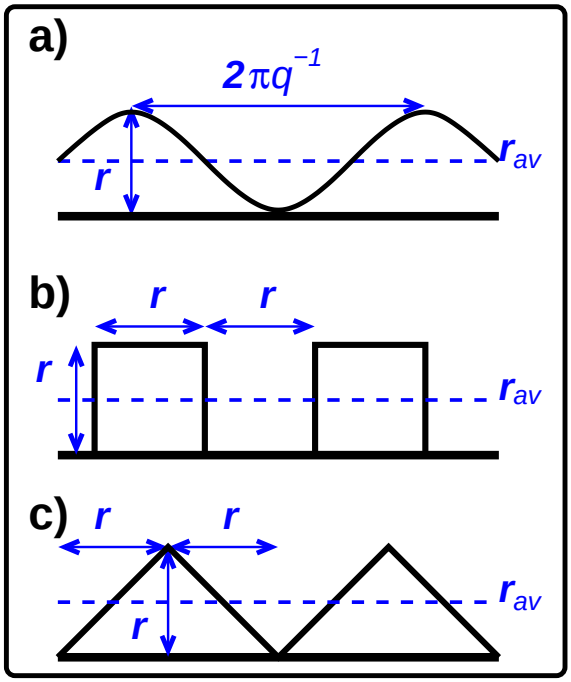

Figure 5.4: Periodic surfaces: a) cosines, b) squares with height and separation given by r, c) triangles, r high and $2r$ wide.

contains information about the effective boundary. The problem of such an approach is that it is limited to small wave numbers. An infinite number of terms would have to be taken into account to obtain a correct result for arbitrary geometries. Panzer et al. gave an analytical equation for the slip-length β in the case of small cosine-shaped surface variations [108]. It is applicable to the case of two infinite planes separated by a distance $2d$, being much larger than the height of the highest peaks r. Surface variations are determined by peaks of height r, valleys at $r_{\min}$ and given by $r(x) = 2r + r/2\cos(qx)$. Here, q is the wave number. Since the surfaces are separated by a large distance, the calculated slip length is equal to the negative[1] effective boundary r_{eff} that now can be expressed in terms of $k = qr/2$ as

$$r_{\text{eff}} = -\beta = \frac{r}{2}\left(1 + k\frac{1 - \frac{1}{4}k^2 + \frac{19}{64}k^4 + \mathcal{O}(k^6)}{1 + k^2(1 - \frac{1}{2}k^2) + \mathcal{O}(k^6)}\right). \tag{5.2}$$

The first term is k independent and shows linear behavior of the effective height r_{eff} on the average roughness $r_{\text{av}} = r/2$. Higher order terms cannot easily be calculated analytically and are neglected. Thus, Eq. 5.2 is valid only for $k = qr/2 \ll 1$. However, for realistic surfaces, k can become substantially larger than 1 causing the theoretical approach to fail. In this case, only numerical simulations can be applied to describe arbitrary boundaries.

To test the simulation method the results are compared to the theoretical model of Panzer and Liu (5.2) and with the results by Lecoq and coworkers [88]. In Fig. 5.5

[1] In this case β is measured from $r_{\min}$. Therefore, an effective boundary position inside the system appears to be a negative slip length. Typically, the slip length is measured from the top of the roughness r.

the effective height r_{eff}, obtained from simulations, is plotted versus r_{av} for cosine shaped surfaces with $qr/2 = k = 1, \frac{1}{2}, \frac{1}{3}$ (symbols). Error bars would be smaller than the symbols and are therefore not shown. Lines are given by the analytical solution of Eq. 5.2. In the inset of Fig. 5.5 the normalized effective height $r_{\text{eff}}/r_{\text{av}}$ obtained from simulations is plotted versus k for cosine shaped surfaces with $r/2 = k = 1, \frac{1}{2}, \frac{1}{3}$ (symbols). The line is given by the analytical solution of Eq. 5.2. For $k < 1$ the simulated data agrees within 2.5% with Panzer's prediction. However, for $k = 1$ a substantial deviation between numerical and analytical solutions can be observed which is expected since Eq. 5.2 is valid for small values of $k << 1$ only. In the case of large $k > 1$, the analytical approach is not able to correctly reproduce the increase of r_{eff} with increasing k anymore. Instead, r_{eff} becomes smaller again due to missing higher order contributions in Eq. 5.2. Our simulations do not suffer from such limitations allowing us to study arbitrarily complex surface geometries [74, 76].

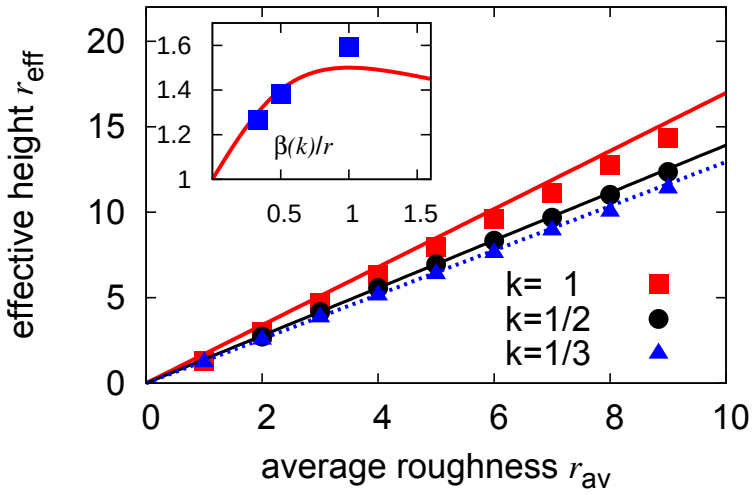

Figure 5.5: Effective height r_{eff} over average roughness r_{av} for a cosine geometry and different variables k. Symbols denote numerical data and lines are given by Eq. 5.2. The inset shows $\beta(k)/r$ according to equation (5.2) and our corresponding simulation data. For $k > 1$ the slope becomes negative, demonstrating that the theory fails for more complex surface structures [74, 76].

Lecoq and coworkers performed experiments with well defined boundary roughnesses, and developed a theory to predict the position of the effective boundary [88]. In the experiments they utilised a laser interferometer to measure the trajectory of a colloidal sphere, and thereby determined the lubrication force and an effective boundary position. The used geometry consists of grooves with a triangular profile. For a theoretical description the boundary is expressed in a Fourier series that gives the boundary condition for the Laplace equation. From this an effective boundary position can be derived by a fast converting series. The roughness that was chosen for their analysis was an array of truncated triangular grooves, similar to the ones in Fig8.4 c). In Fig 5.6 the effective boundary positions for such a geometry is plotted. The results match with the theoretical value of Lecoq et al. [88] for a similar

geometry.

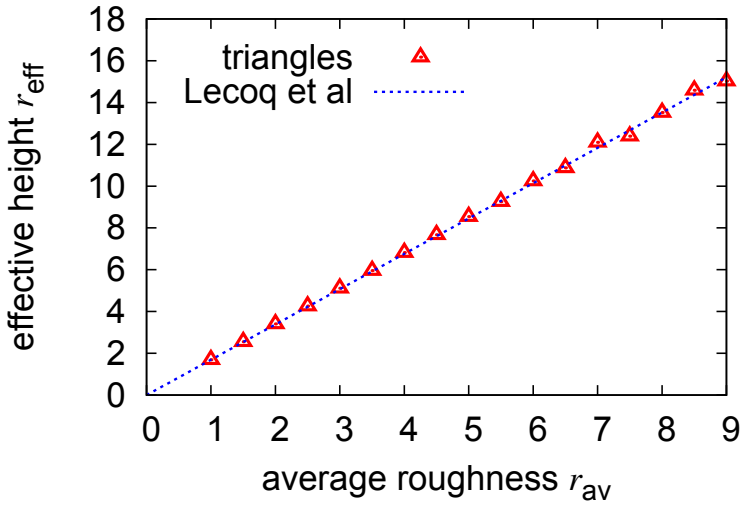

Figure 5.6: Simulated effective height r_{eff} versus r_{av} for triangular shaped grooves. The triangular shape matches the theoretical and experimentally validated results of Lecoq et al. [88] for a similar geometry that is plotted as dotted line [49].

A major problem of an analytical approach is that it can only be applied for surfaces that can be well expressed by Fourier-series. Since one needs an infinitely high orders, to describe arbitrary surfaces, it is not possible to express them analytically and thus numerical solutions are needed [83].

5.2 Results

5.2.1 Model roughness

In Fig. 5.7 r_{eff} is plotted versus r_{av} for the different types of roughness discussed in the previous section. By performing a linear fit to the data as given by the lines one finds for the uniformly randomly distributed roughness that the position of the effective wall is at $r_{\text{eff}} = 1.84 r_{\text{av}}$ with $r_{\text{av}} = r/2$ or in other words at 92% of the maximum height r.

For squares and triangular structures the constants of proportionality are found to be $c = 1.90$ and $c = 1.69$ indicating that the shape of the surface variations indeed affects the position of the effective boundary. However, the effect of the shape is small compared to the effect of the height of the variations. All surface structures are geometrically similar causing the linear dependence between r_{eff} and $r_{\text{av}} = r/2$ and c to be independent of the lattice resolution.

When converting the 3D random roughness into a purely 2D structure, the difference in the measured constant of proportionality c is in the range of the error of the fit algorithm. This is a surprising result since in 3D the flow can pass sidewise around a roughness element. The measured r_{eff} is found to be independent of the

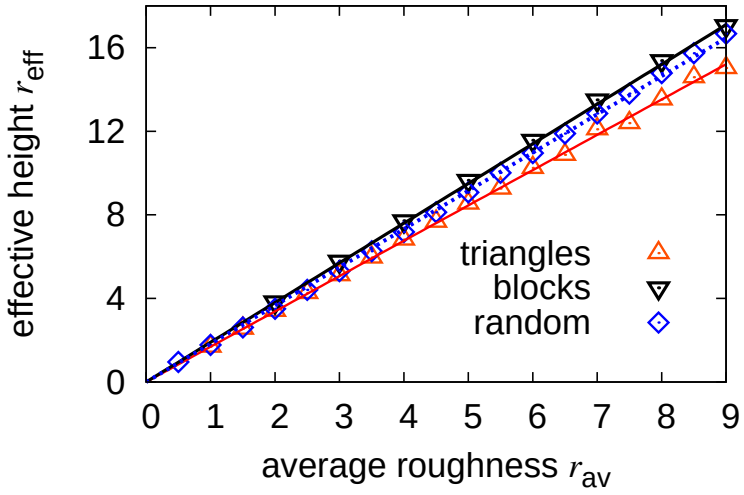

Figure 5.7: Effective height r_{eff} versus r_{av} for triangles, blocks (see Fig. 8.4), and an equally distributed random roughness. Lines are a linear fit to the simulated data with slopes 1.90, 1.69, and 1.84.

flow velocity over more than 3 decades and does not depend on pressure either, i.e., r_{eff} is independent of the Reynolds number.

Non symmetric surface topology

In reality high spikes on a smooth surface may occur, so that the average roughness r_{av} is much smaller than half the maximum height $r/2$. This can be modeled by a triangular geometry with additional void space a between the roughness elements. As shown in the previous paragraph, the actual shape of the roughness elements has only a minor influence. However, the ratio a/r should have an influence, as long as a is sufficiently large. In this paragraph values of $r = 5$ and $r = 10$ lattice sites are chosen to be the maximum height of the roughness. Similarly to Fig. 5.7 the effective surface height r_{eff} over the average roughness r_{av} is plotted in Fig. 5.8. It is apparent that the average roughness is smaller than one half of the maximum height $r/2$, i.e., $r_{\text{av}} = \frac{r^2}{2r+a} \leq r/2$. The values of $r = 5$ are scaled by a factor of two to be comparable with the values of $r = 10$. Due to the geometrical similarity of the surface structure this scaling is possible. For comparison with Fig. 5.7 the linear fit with slope $c = 1.69$ is plotted. As can be seen in Fig. 5.8, for spaced roughness elements, the maximum height r has a strong influence on the effective height r_{eff} while the spacing a does not. For small values of r_{av} (due to large additional distance a), which is corresponding to a flat surface, the effective height r_{eff} converges to zero. For small a the effective height r_{eff} converges to the same value as the triangle geometry, as given in Fig. 5.7. For intermediate values of $a \approx 2h_{\text{max}}$ the effective boundary position is still in the range of 75% of the maximum height r. This is an important result, since it demonstrates that the distance between the effective boundary position r_{eff} and the lowest surface parts r_{min} can be much larger than the average roughness height r_{av}. In such cases $r_{\text{eff}} > 6 \cdot r_{\text{av}}$ can be obtained. On the

other hand, for large a this results in $h_{\text{eff}} < 0.7 \cdot r$. Therefore, in the case of large $a \approx 2r$, the effective height r_{eff} cannot be approximated by the maximum height $r_{\max}$ nor by the average roughness r_{av}.

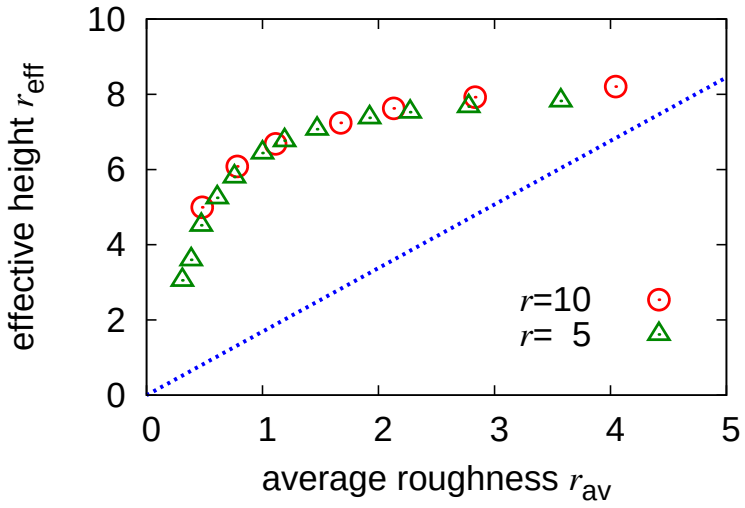

Figure 5.8: r_{eff} versus r_{av} for triangles with $r = 5$ and 10. The distance between triangles a is varied to obtain the given r_{av}. Values of $r = 5$ are scaled by a factor of 2 so one would see possible discretization effects. The fitted values for a triangle geometry are shown as dotted line.

5.2.2 Flow over a realistic surface

An advantage of the lattice Boltzmann method over other CFD-methods is that non-trivial boundary-structures can easily be implemented. It is for example possible to use experimentally measured surfaces like the ones obtained from AFM data of a gold coated glass surface which have been used in microflow experiments by O.I. Vinogradova and G.E. Yakubov [150]. The sample size is $1\mu\text{m}^2$ represented by 512×512 data points with a maximum peak to valley distance of 64nm. The lattice constant of the LB simulation can be scaled to 1.9nm by setting the relaxation time τ to 1.15 and by mapping the speed of sound and the kinematic viscosity to the values for water ($c_s = 1.5 \cdot 10^3\text{m/s}$, $\nu = 1.02 \cdot 10^{-6}\text{m}^2/\text{s}$). r_{eff} can then be measured as described in the previous paragraphs by loading the AFM data onto our simulation lattice. For the simulations presented in this paragraph, the channel width is set to 128 lattice units. The effective height, obtained by the simulation of Poiseuile flow over the gold surface, is depicted by the square at r_{av}=21nm in Fig. 5.9. Data points at $r_{\text{av}} = 4$ and 8 are obtained by downscaling the original data set with a constant factor. By analysing the surface data it is found that the distribution of surface heights follows a Gaussian distribution. This distribution is used to generate an artificial random surface with identical height distribution. To generate this height distribution a Gaussian-distributed random height for every lattice point on the surface is obtained from a Box-Müller based algorithm [14]. The width of the distribution σ and the average height r_{av} can be set. By using the same sequence of

random numbers and scaling σ with r_{av} one obtains geometrically similar geometries. This similarity is important because the effective height h_{eff} scales with the average roughness in the case of geometrical similarity [74]. In contrast to the AFM data, the random-surface data points are fully uncorrelated, while the gold surface shows distinct structural properties as can be observed in the left background image of Fig. 5.9. For artificial surfaces, the average roughness r_{av} can be scaled by varying the width of the Gaussian distribution of random numbers that allows to determine r_{eff} for r_{av} up to 40nm. As indicated by the dotted line, the measured r_{eff} linearly depends on r_{av} with a constant of proportionality of $c = 1.43$. The data obtained from the gold coated surface follows the same linear dependence demonstrating that the actual surface shape does not influence its effective position, but only the distribution of heights needs to be known, as long, as the correlation length of the heights is sufficiently small.

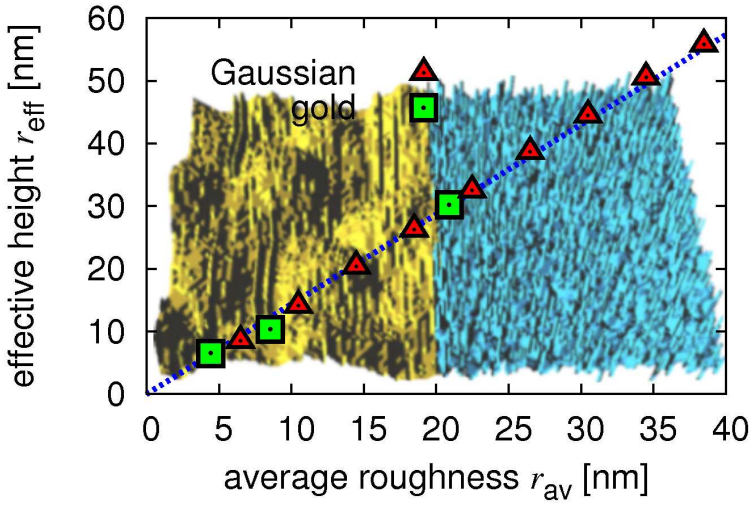

Figure 5.9: Simulated r_{eff} versus r_{av} for gold coated glass and a randomly generated surface with Gaussian distributed heights. The background image shows the gold surface (left) and the artificially generated structure (right).

As an extension of the distribution from one sample, Gaussian distributed heights with different widths σ are investigated. In Fig. 5.10 the effective height r_{eff} is plotted versus the average height r_{av} for $0.054 < \sigma/r_{\text{av}} < 0.135$. The height of the effective wall depends linearly on σ in the observed range as it can be seen in the inset. The effective height r_{eff} can be fitted by

$$h_{\text{eff}} = 1 + 3.1\sigma. \tag{5.3}$$

The range of distributions is limited by the resolution of the lattice. If σ becomes too small, the surface is nearly a flat wall, while a too large σ results in a porous medium instead of a channel because the possible simulation volume is limited by the available computer power.

The effective height r_{eff} ranges from $1.15r_{\text{av}}$ to $1.45r_{\text{av}}$. These values are lower than the effective heights for an equally distributed roughness ($1.84r_{\text{av}}$). Previous

studies showed that experimentally available surfaces commonly have Gaussian distributed roughness. Therefore, the results shown here can help to estimate r_{eff} in real microchannels.

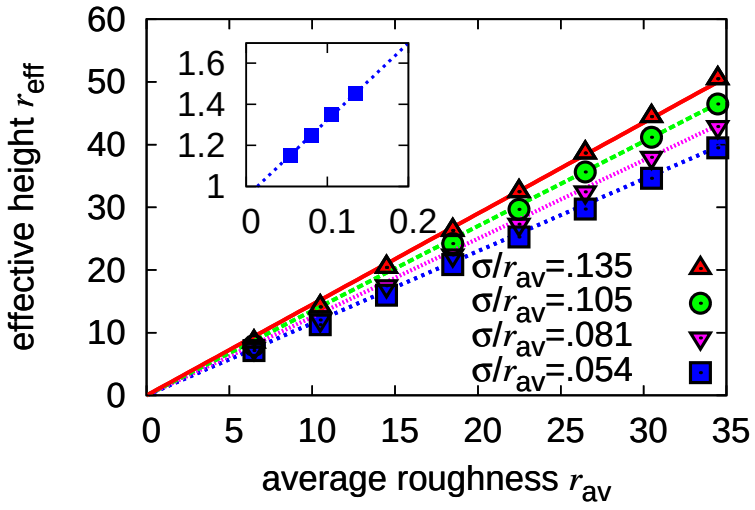

Figure 5.10: Effective height r_{eff} over average roughness r_{av} for Gaussian distributed height elements with different width of the distribution σ. Symbols are the simulation results, lines are a linear fit to the data. In the inset the slope of the fitted lines is plotted over σ/r_{av}. It shows the linear dependence of the effective height on σ.

5.2.3 Influence of roughness on the slip length

The most important question to be answered in this chapter is the effect of a wrongly assumed position of a surface on experimental measurements. As mentioned in the introduction many groups use an approaching method to measure the slip length β. Here, a colloidal sphere at the tip of a cantilever immersed in a fluid is oscillated in the vicinity of a surface, or the cylinders of a surface force apparatus (SFA) are brought close to each other. The distance between the surfaces can become very small – even down to contact. To study the influence of the roughness on an apparent slip effect, it can be assumed that the surface is placed at r, as it is commonly done in experiments [13]. Then, the slip length β is measured by fitting Eq. 5.1 via β. The wrong position of the surface causes a substantial error in the detected slip as can be inferred from Fig. 5.11. Here, β is given versus the average roughness height r_{av} for randomly generated boundaries with the heights of the surface obstacles following the Gaussian distribution given by the AFM data of the gold surface. For small r_{av} (and thus large separation of the plates) β is in the range of $r - r_{\text{eff}}$ and can be neglected in most practical cases. However, the detected slip diverges if r_{av} becomes larger. Here, a large r_{av} is equivalent to the channel width becoming very small – an effect also common in typical surface approaching experiments or microchannel flows. For curved surfaces, as they are utilized in SFA or AFM based slip measurements, the detected β can be even larger due to higher

order components of the flow field. This might explain experiments reporting large slip lengths of $\beta \approx 100$nm [86, 104].

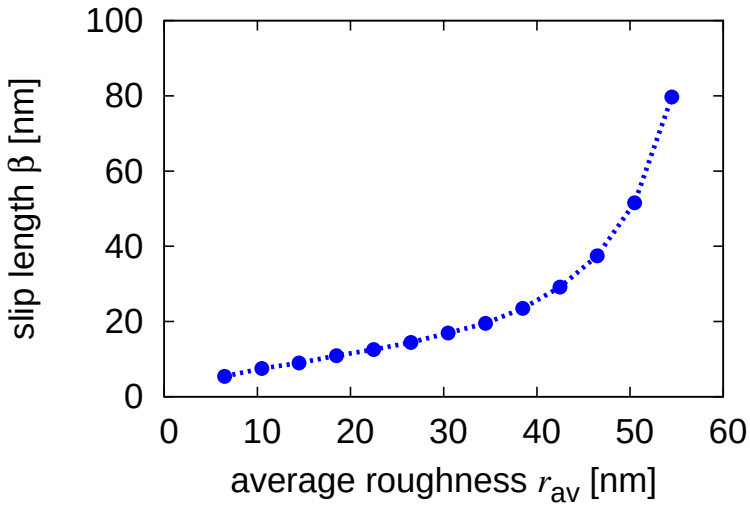

Figure 5.11: β versus r_{av} for water and randomly distributed roughness. By assuming $r_{\text{eff}} = r$, β is in the range of $r - r_{\text{eff}}$ for small r_{av}, but diverges for large r_{av}.

5.3 Rough hydrophobic surfaces

A further interesting point in this chapter is how roughness and the surface wettability act together. In order to study this interplay, simulation results are presented for a setup of rough channels including a fluid-wall interaction force. This force is similar to a Shan-Chen force, as presented in chapter 4. As reminder it is stated here that the Shan-Chen force is a repulsive force

$$f_{w,f}(\mathbf{x}_j) = \Psi\left(\rho(\mathbf{x}_j)\right) g_{wf} \mathbf{c_i} \sum \Psi\left(\rho_w(\mathbf{x}_j + \mathbf{c}_i)\right),$$

which leads to a depletion zone on the fluid nodes neighboring the boundary. Due to this depletion the dynamic viscosity in this zone is lowered and therefore an apparent slip can be measured. The steering parameters of the slip length are the local wall density ρ_w and the global interaction parameter which is kept constant at $g_{wf} = 0.08$. For a more detailed explanation see chapter 4 or the literature [48]. For the wall density values of ρ_{wall} 0.5, 1, and 5 are chosen. For these values and perfectly smooth surfaces the slip length β has been determined to be 0.65, 1.13, and 1.3, respectively. The roughness is composed of equally distributed random heights, so that $r_{\text{av}} = r/2$. In order to obtain better results the values obtained from four different seeds of the random number generator are averaged. The seed determines the sequence of random numbers and therefore the actual shape of the boundary but not the macroscopic properties, since the averaged parameters are left constant.

When analysing the effective height of rough hydrophobic walls in dependence of the average roughness r_{av} we find for $r_{\text{av}} > 4$ a linear dependence between the

average roughness r_{av} and the effective height r_{eff}. An interesting point however is that the slope for different ρ_{wall} is different. That means that the fluid-surface interaction does not result in a simple offset on the effective height r_{eff} but rather in a non linear effect.

To decouple the effect of roughness and wettability the slip length is determined by setting the effective distance d_{eff} in equation (5.1) to the effective distance for a rough no-slip wall that is determined according to the procedure described in the section above. It is then possible to fit the corresponding velocity profile via the slip length β. By this procedure a slip length can be obtained which is not based on a falsely assumed surface position but rather caused by the interplay of surface forces and roughness.

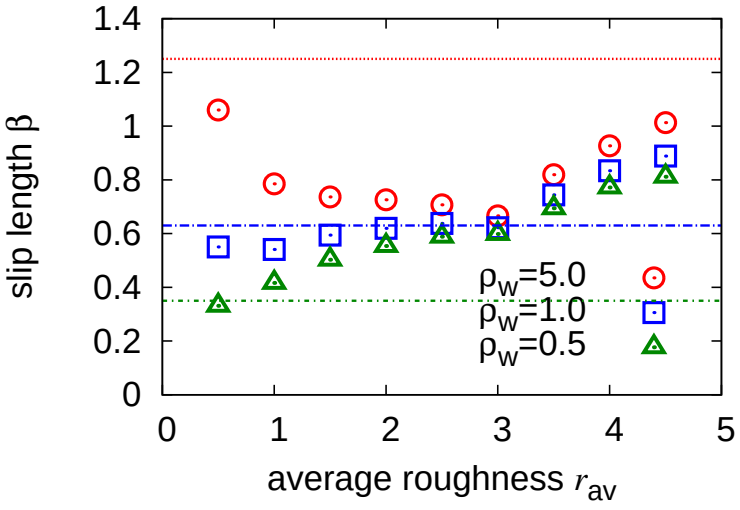

Figure 5.12: Slip length β over average roughness r_{av} for equally distributed random height elements for different fluid-wall interaction $\rho_w = 0.5$, 1.0, 5.0. The position of the effective height h_{eff} is chosen as the value for a non-interacting wall. The lines show the slip length for smooth boundaries ($r_{\text{av}} = 0$).

In Fig. 5.12 it can be seen that the slip length β for strong fluid-wall interactions ($\rho_w = 5$) first decreases with the average roughness and then rises. For a lower interaction with $\rho_w = 0.5$, the slip length is constantly growing and leads to an increase of the slip length by a factor of more than three. There are two opposing effects present in this system and their interplay can explain the observed behavior. The decrease of the slip length β for moderate roughness is due to an increased friction near the boundary. The increase has its reason in the increased total surface area and therefore a stronger reduced density near the hydrophobic rough surface. Due to this low density which is trapped in the asperities of the surface, the fluid "feels" a smoothed effective surface. Unlike the implementation of Sbragaglia et al. [117] the L-BGK model used for the simulations in this chapter is not able to model the liquid-gas transition near the surface. The model implements only a density difference between the bulk fluid and the lattice site directly next to a surface site. Further, unlike the implementation of Schmieschek and Harting There is no third component (gas or oil) [121]. Therefore, one cannot easily calculate the

contact angle in the presented simulations in contrast to the results presented by Benzi et al. [8]. This is due to the fact, that for a contact angle three phases (typical gas, droplet and wall) are needed. However, the general effect of a pressure drop near a hydrophobic surface is the same as in the model used by Sbragaglia [117]. It can therefore be used to explain the behavior of polymer melts close to rough hydrophobic surfaces. In such a system the shorter polymer chains are enriched close to the boundary leading to a low viscous layer [6]. For a more detailed study on super-hydrophobic surfaces, the strong surface variation as well as the liquid-gas transitions have to be taken into account.

Resume

In this chapter Poiseuille flow between two rough surfaces is studied. The concept of an effective boundary position is introduced. Further, the effective boundary position for different surface geometries is investigated. A key result is that the effective boundary position mainly depends on the maximum roughness height r and the distribution of the roughness height. The actual shape of the roughness elements or the average roughness height have only a minor influence on the position of the effective boundary. Furthermore, it was shown that the interplay of roughness and surface wettability can lead to non-linear effects regarding the value of the slip length.

Chapter 6

Lubrication force on a sphere approaching a flat surface

The main part of this work concentrates on the simulation of the AFM based slip experiments. Therefore, it is necessary that the simulation method is tested well and the best simulation volume which is small enough to keep finite size effects below an acceptable limit but still allows fast simulations is found. Further, it has to be assured that the simulation method is able to reproduce the well established theoretical solutions for cases where analytical solutions exist. One of them which is applicable, is the theory of Brenner and Maude for the case of a sphere submerged in a Newtonian liquid that is approached towards a surface. In this chapter it will be assured that this theory is reproduced by the simulation method and that finite size effects can be avoided by choosing the correct boundary condition.

6.1 Discretization effects without boundaries

Finite size effects commonly occur in computer simulations because one has limited resources, thus the simulated systems are small compared to experiments. Therefore, the boundaries of the system are much closer to the region of interest than in experiments and in contrast to most theories which typically assume an infinite volume. A typical approach to limit finite size effects is to use periodic boundary conditions. However, in such a system the region of interest then interacts with its periodic images. Hasimoto gives a theoretical solution for the drag force of a sphere in a periodic array as it appears in a simulation where all boundaries are periodic [51]:

$$\mathbf{F}_{\mathrm{Ha}} = \frac{\mathbf{F}_{\mathrm{St}}}{1 - 2.83a + 4.19a^3 - 27.4a^7 + O(a^9)} \tag{6.1}$$

Here, $a = R/n$ is the ratio between the radius of the sphere R and the system length n. The Stokes force is given by

$$\mathbf{F}_{\mathrm{St}} = 6\pi\mu R\mathbf{v}, \tag{6.2}$$

with μ being the viscosity of the liquid and $\mathbf{v}$ the velocity of the sphere.

Besides a finite simulated volume most simulation methods utilize a finite discretization of the simulated objects, i.e., the sphere in our case consists of many

blocks instead of being a perfect sphere. This means that the finite size and the resolution influence the result of a simulation. However, it is usually possible to limit the influence of finite size effects and the loss of accuracy due to discretization if those errors are known and taken into account properly.

It is known from previous studies that the discretization of the sphere results in a deviation of the Stokes force F_{St} or in case of periodic boundaries from the Hasimoto correction [80, 82, 143]. Therefore, simulations are performed of a moving sphere in a liquid with periodic boundary conditions what makes it possible to compare the drag force for different radii with Eq. 6.1.

In table 6.1 the measured force F, the theoretical force F_{Ha}, the radius R_{set} set in the simulation, and the resulting effective radius R_{eff} are shown. Since all movement is in y-direction, from here on only the y component of the force and velocity is shown if not stated otherwise. For a better comparison the ratio of $R_{\mathrm{set}}/R_{\mathrm{eff}}$ is shown as well. In all simulations the system size is chosen to be $n/R = 5$. The shear viscosity is set to $\mu = 0.1$ and the velocity is set to 10^{-3} lattice units per time-step. The simulations have been performed with an older simulation code and only the first order in Eq.6.1 was taken into account. Besides this the table shows that the deviation between the set radius and the effective radius shrinks with increasing radius but seems to stay constant at $1.04R_{\mathrm{set}}$. Latter implementations of the sphere do not suffer from such large deviations.

F_{Ha}	F	R_{set}	R_{eff}	$R_{\mathrm{eff}}/R_{\mathrm{set}}$
0.625	0.704	4.0	3.5	1.13
1.251	1.205	8.0	3.3	1.04
1.876	1.769	12.0	12.7	1.06
2.501	2.389	16.0	16.7	1.04

Table 6.1: Investigation of the effective radius in a small confined system.

6.2 The Brenner-Maude theory

The case that is of interest here, however, is different and more complex due to a broken symmetry caused by the approached surface. In this section the commonly used theory is recapitulated. In most of the experiments the relative velocity v of the sphere with the radius R is so small that the simple Reynolds theory as it is presented in chapter 3 for the lubrication force

$$F_{\mathrm{Re}} = -6\pi\mu v R^2/d, \tag{6.3}$$

can be applied. Here, μ is the dynamic viscosity of the fluid [79]. Note that for larger distances d between the surface of the sphere and the approached boundary the force in Eq. 6.3 does not converge towards the Stokes drag force $F_{\mathrm{St}} = -6\pi\mu v R$ which is valid for a sphere moving freely in a fluid. Therefore, this simple Reynolds lubrication fails in case of a larger velocity v or greater separations d, where the Stokes force is not sufficiently small to be neglected. The system can be described

accurately by the theory of Maude [95]. The base of the theory is a solution for two spheres approaching each other with the same rate, similar to the simple approach in chapter 3 but taking into account higher order terms in the parameterization of the surface. By transforming the coordinates, applying symmetry arguments and setting the radius of one of the spheres to infinity one ends up with a fast converging sum for the drag force acting on the sphere:

$$F_{\text{Maude}} = 6\pi\mu v R\lambda_1, \tag{6.4}$$

with

$$\begin{aligned}\lambda_1 &= -\tfrac{1}{3}\sinh\xi \\ &\times \left(\sum_{n=1}^{\infty} \frac{n(n+1)\left[8e^{(2n+1)\xi}+2(2n+3)(2n-1)\right]}{(2n-1)(2n+3)[4\sinh^2(n+\frac{1}{2})\xi-(2n+1)^2\sinh^2\xi]}\right. \\ &\left. -\sum_{n=1}^{\infty} \frac{n(n+1)\left[(2n+1)(2n-1)e^{2\xi}-(2n+1)(2n+3)e^{-2\xi}\right]}{(2n-1)(2n+3)[4\sinh^2(n+\frac{1}{2})\xi-(2n+1)^2\sinh^2\xi]}\right),\end{aligned}$$

where $\cosh\xi = (d-R)/R$. The term given by λ_1 cannot be treated analytically. Thus, λ_1 is evaluated numerically with a convergence of 10^{-10}. A more practical approximation of (6.4) is given in the same paper [95]:

$$F(h) = 6\pi\mu R v\left(\frac{9}{8}\frac{R}{d}+1\right) \tag{6.5}$$

Here, one can easily see that the force converges towards the Stokes force for an infinite distance d and approaches the Reynolds lubrication Eq. 6.3 for small separations d. This theory is applicable for a perfect sphere approaching a surface with an arbitrary approaching velocity v as long as the Reynolds number is low enough to keep the fluid in the laminar flow regime. In the following sections simulations that can be compared to this theory are presented and the influence of different sources of error is investigated.

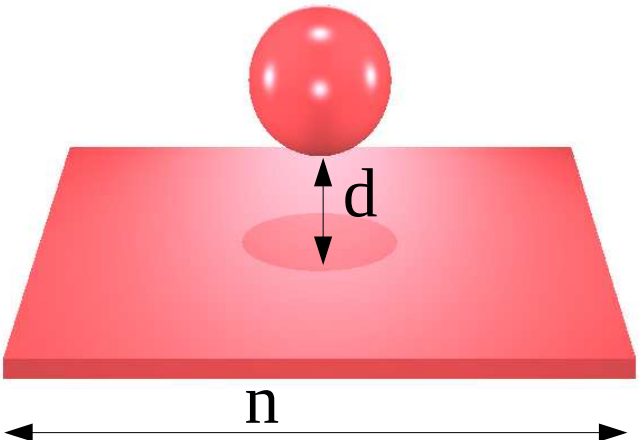

Figure 6.1: A sketch of the simulated system. The distance between the surface and the sphere is d and the system length is n. The surrounding fluid is not shown.

In Fig. 6.1 a sketch of the simulated system is shown. A sphere embedded in a surrounding fluid is simulated. While the sphere approaches a surface the force

acting on it is recorded. Due to the jump-like movement of the sphere the force shows a significant noise from time-step to time-step which makes it necessary to average the force and to keep the velocity low so that the fluid can relax after a reformation of the boundary nodes. Simulations with different sphere radii R and different system width n are performed to investigate finite size effects. For simplicity the x and z dimensions are set to the same value n and the propagation dimension y is kept constant at 512 lattice units. If not stated otherwise the simulation parameters are $\mathbf{v} = 0.001$, $\mu = 0.1$, and the radius is varied between $R = 4$ and $R = 16$. The typical force averaging is done over 333 time-steps. It is assured that the averaging does not influence the results, i.e. the results for averaging over 99 up to 999 time steps are compared and no significant deviation is found. 333 time steps reduce the noise strongly while the spatial coarse -graining due to the constant velocity is over 0.3 lattice sites which is a good spatial resolution. For a better visibility of the data points only a fraction of them is plotted. The approached boundary is a plain no-slip wall which is realized by a mid-grid bounce back boundary condition. Along the open sides periodic boundary conditions are applied so that the sphere can interact with its mirror images leading to undesired finite size effects.

6.3 Finite size effects with boundaries

A major contribution to the finite size effects is the interaction of the sphere with its periodic image. Therefore, a larger system length should reduce this effect dramatically. However, when the hydrodynamic influence of the wall becomes larger, finite size effects become smaller. This can be explained by the fact that the friction at the boundary suppresses the hydrodynamic interaction of the particle with its periodic image. Instead, the dominant interaction is between the particle and the surface. It is mandatory for a better understanding of the system to learn how these finite size effects can be described, quantified, and controlled.

6.3.1 Large test

First, a run of a large 512^3 system assures that the method really shows the desired asymptotic behavior, i.e., it is able to reproduce the theory Maude. Further it has to be checked that the force scales with the velocity. To demonstrate this behavior a long run with a smaller $R = 8$ sphere in a 256^3 system is performed as well but with a velocity of $v = 10^{-4}$ instead of the usual 10^{-3} lattice nodes per time-step. Since the sphere is smaller by a factor of 2 it consumes a factor of 16 less computer power to run a simulation in which all lengths are scaled by the radius. A factor of 8 in the computer power is due to the smaller simulation volume and an additional factor of 2 due to the shorter length the sphere has to travel at the constant speed to travel the same fraction of its radius i.e. twice as many time steps have to be performed. That is why the velocity independence is shown with $R = 8$. In addition intermediate velocities $10^{-4} < v < 10^{-3}$ are tested to assure the results but are not shown here for a better visibility of the main results.

The simulated data are plotted together with the first order approximation and the theoretical values by Maude in Fig. 6.2. If not stated otherwise values in this

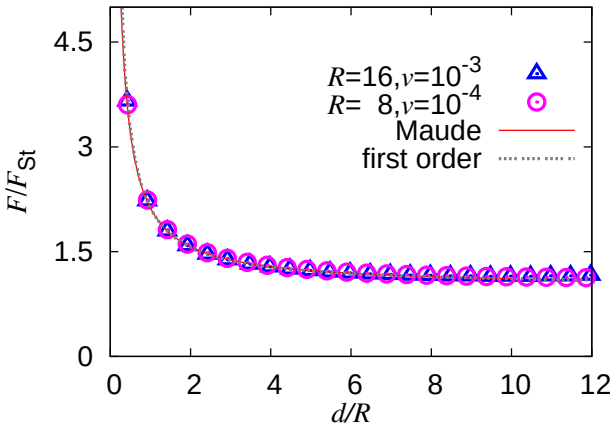

Figure 6.2: Normalized force F/F_{St} versus normalized separation d/R for large separations for a sphere of $R = 16$ lattice units at an approaching velocity of $v = 10^{-3}$ lattice units per time step and a sphere of $R = 8$ with approaching velocity $v = 10^{-4}$. Further, the theoretical values by Maude and the first order approximation are shown. All data show good agreement.

thesis are normalized by a characteristic value of the system, for example the force is normalized by the Stokes force

$$F_{\mathrm{St}} = -6\pi\mu v R$$

and the separation d is normalized by the radius of the sphere R. This is done for better comparability. The data of Fig. 6.2 shows good agreement with the theory of Maude and the first order approximation but for a better visibility of possible errors it is helpful to use different scales for plotting the data.

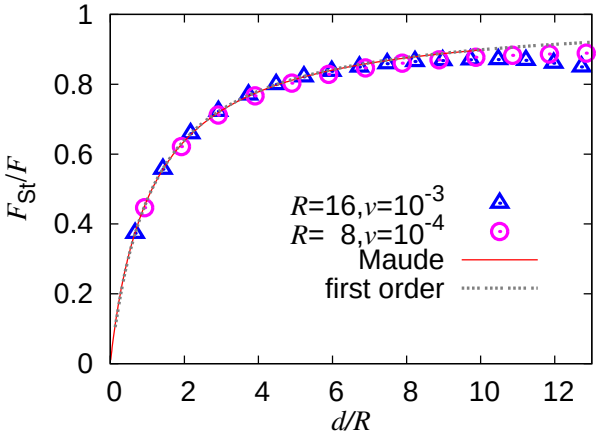

Figure 6.3: Inverted normalized force F_{St}/F versus normalized separation d/R. The plot shows the same data as Fig. 6.2. Due to the way of plotting the data a deviation near the Stokes force becomes obvious. At $d > 12R$ the force deviates due to the influence of the far side boundary.

In case the area of interest lies in the approximation towards the Stokes force at large separations d, the best way to plot the data is to plot the inverted force $\frac{1}{F}$

versus the distance d. Such a plot is shown in Fig 6.3. Here, only a small deviation at large separations d is seen that origins in the influence of the opposite boundary, but in later plots deviations become more visible.

In case the area of interest lies close to the boundary as it is the case in the presented studies, it is favorable to plot the force F versus the inverse separation $\frac{1}{d}$ as shown in Fig. 6.4. Since the distance is inverted one never reaches the actual boundary in such a plot, but has a good resolution of the area close to the boundary as it is desired in most cases of this thesis. In the plot one sees the asymptotic behavior and that both radii/velocities do not show significant deviations. Further, the data rather follow the first order approximation (see Eq. 6.5) than the actual Maude solution. The reason lies in the jump-like movement and is discussed later.

It is shown that the simulation method used is able do reproduce the theoretical values, but still the ideal simulation volume has to be found in order to achieve good results with reasonable computational costs.

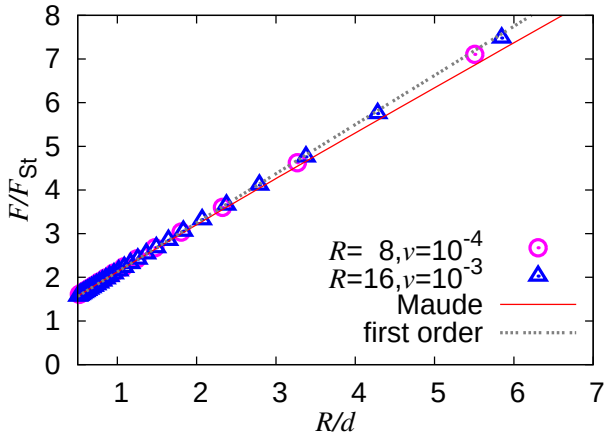

Figure 6.4: Normalized force F/F_{St} versus normalized inverted separation R/d. The plot shows the same data as Fig. 6.2. Due to the way of plotting deviations near the boundary become obvious. Interestingly, the simulation follows the first order approximation rather than the Brenner Maude solution.

6.3.2 Influence of the system size

First, a system with a constant sphere radius $R = 16$ is studied and the system length n is varied. As shown above and validated later, a sphere of $R = 16$ reduces discretization effects sufficiently so they are much smaller than the influence of the periodic image. In Fig. 6.5 the drag force F normalized by the Stokes force F_{St} and the inverse normalized drag force are plotted. In the inverse case the deviations for the larger distance d can be seen more clearly. Fig. 6.5 shows that the deviation for the small system $n = 192$ close to the wall is very small, however the force does not converge to the Stokes force F_{St}. Here, effects similar to the ones reported by Hasimoto (Eq. 6.1) appear. For small separations d the force decays with $\frac{1}{d}$ while it approaches a constant value for large d. The constant values should be given by the Stokes force F_{St}, but can be larger due to the interaction with the periodic image.

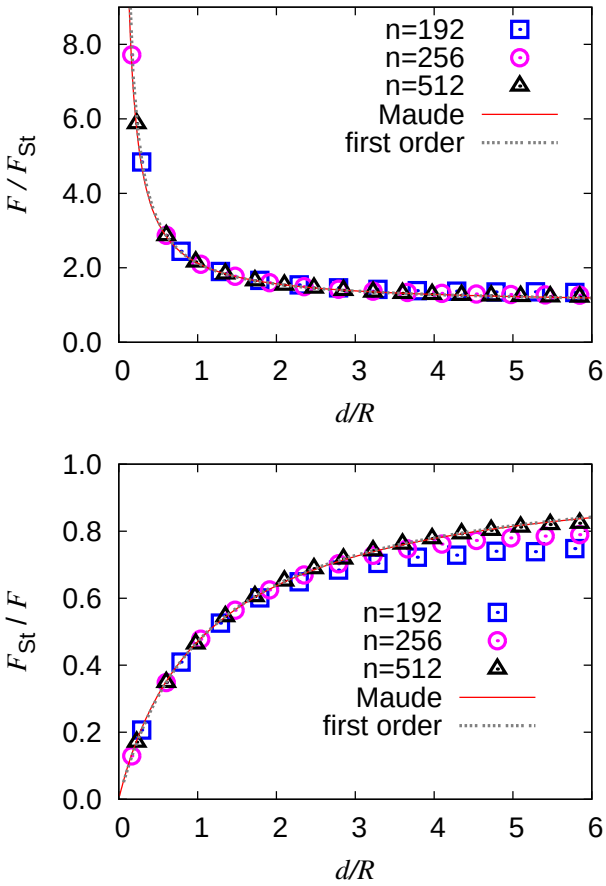

Figure 6.5: Normalized lubrication force $\frac{F}{F_{St}}$ and the inverted normalized lubrication force $\frac{F_{St}}{F}$ versus the normalized distance d/R for different system lengths n. The radius of the sphere is fixed at $R = 16$. The deviation for $n = 192$ is significant at larger radii, but can be neglected for small distances. For $n = 512$ there is nearly no deviation from the exact solution of Maude (6.4). In addition, the deviation of the first order approximation (6.5) is below 1% for $d > R/2$.

In the $1/F$ plots it can be seen that the deviation is not a constant offset or factor but rather starts at a critical value of d/R. From there, the force quickly starts to approach a constant value.

In Fig. 6.6 the relative error $E = \frac{F - F_{Maude}}{F}$ is plotted for different system sizes n and a constant radius R. The error for the largest system $n = 512$ in Fig 6.6 is constantly below 1% for larger distances $d > R/2$. At distances less than $d < R/2$ the error rises due to the insufficient resolution of the fluid filled volume between the surface of the sphere and the boundary. Another possible effect is the fact that the sphere rather jumps over the lattice than it performs a continuous movement. Additionally, it can be seen that for distances less than $d = R$ the error for the different system sizes n collapses. The reason is that for smaller distances the lubrication effect which is independent of the system length n dominates the free flow and therefore suppresses finite size effects due to the periodic image. The deviation for the $n = 512$ system that can be seen at large d has its origin in the transient.

Since the fluid is at rest at the start of the simulation and it takes some time to reach a steady state this can only be avoided by longer simulations. An interesting fact is that the deviation between the Maude solution and the first order approximation is below 1% and that the simulation follows rather the first order approximation than the Maude theory. A possible explanation is that the higher terms of the Maude theory have its origin in the non static behavior of the system, while the first order term would describe a sphere in a quasi static case. I.e., the sphere stays still with a boundary velocity but neglects its change of position. This is similar to the simulation and its-jump like behavior described in chapter 4.

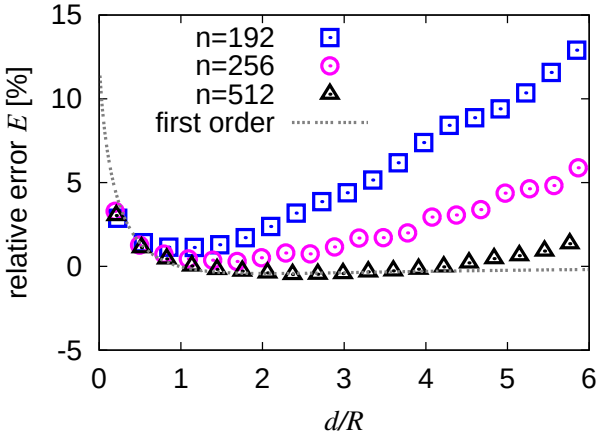

Figure 6.6: Symbols denote the relative error $E = \frac{F - F_{Maude}}{F_{Maude}}$ in % versus the normalized distance d/R for different system sizes n. The line shows the first order approximation. As expected, the error close to the wall deviates due to the discretization of the small distance d. The error becomes larger for large d due to the influence of the periodic image.

6.3.3 Influence of the radius

Since the sphere is discretized on the lattice it is important to understand if this discretization has an effect on the lubrication force. Therefore, simulations with a radius of $R = 4, 8, 16$ are performed at a constant ratio $R/n = 1/32$ of the radius and the system length. Fig. 6.7 depicts the normalized lubrication force $\frac{F}{F_{\mathrm{St}}}$ and the inverted normalized lubrication force $\frac{F_{\mathrm{St}}}{F}$ versus the normalized distance d/R for different radii R. It can be seen that the discretization of the sphere has little influence on the measured force. Fig. 6.8 shows the relative error E for different radii. For all radii the finite size effects due to the periodic image are negligible since the ratio R/n is sufficiently small. The deviation from the Maude theory for separations $d > R$ are below 2% for all radii. Therefore, one has to concentrate on small distances d where significant deviations appear. In our case this distance is better resolved for larger R (note that in the plot the normalized distance is shown). In addition, the resolution of the sphere is better for larger R. For $R = 4$ the deviation is more noisy and here the discretization really has an effect on the drag force F. Additionally, there should be three or more lattice sites between the

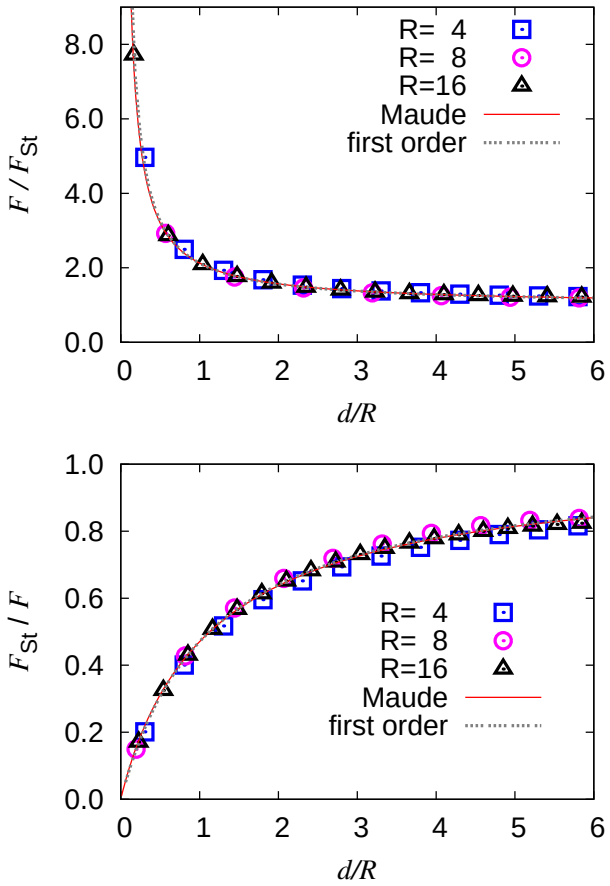

Figure 6.7: Normalized lubrication force $\frac{F}{F_{\mathrm{St}}}$ and the inverted normalized lubrication force $\frac{F_{\mathrm{St}}}{F}$ versus the normalized distance d/R for different radii R but constant ratio $R/n = 1/32$. For $R = 4$ a deviation at small distances can be seen.

surface of the sphere and the boundary. If that is not the case the hydrodynamic interaction is not resolved sufficiently. If the distance between surface and sphere is smaller than half a lattice spacing the two surfaces merge and the method fails. Hence, it it advantageous to choose a large radius in order to be able to reduce the relative distance to the boundary (in units of the sphere radius) or to resolve a possible surface structure. For $R \geq 8$ the deviations have a regular shape and follow the deviation for the first order approximation. The trend to follow the first order approximation is stronger for $R = 16$ but here the noise is reduced further and all errors seem to be systematic. Therefore, the deviation has to be described as a systematic error of the method that has its origin in the jump-like movement of the sphere. The first order approximation is a quasi-static approximation and rather represents the actual simulated case than the theory of Maude does.

It should be noted that the finite size effects for $R = 16$ and $R/n = 1/16$ due to the interaction with the periodic image are much more significant than the discretization effect. By choosing a large simulation volume, a radius $R > 8$ and focusing on the force for separations $d < 2R$ one can reduce those effects to a deviation of the measured force from the theoretically predicted value of less than 1%.

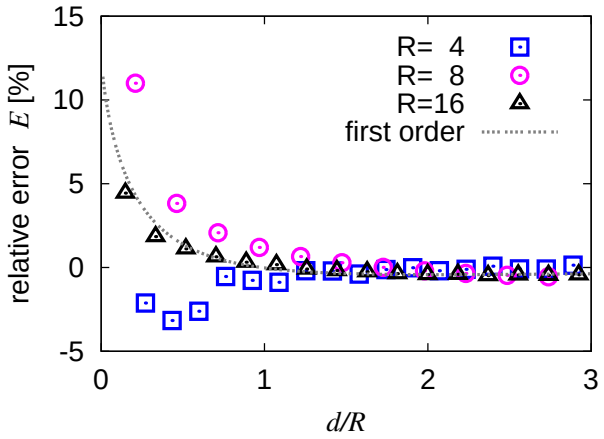

Figure 6.8: Relative error $E = \frac{F - F_{\text{Maude}}}{F_{\text{Maude}}}$ in percent versus the normalized distance d/R for different radii n at a constant ratio $R/n = \frac{4}{128}$ (symbols). As expected the error close to the wall deviates due to the discretization of the small distance d. For $R = 4$ the deviation fluctuates due to the low resolution but for $R = 16$ it follows the first order approximation. The line corresponds to the first order approximation of the Maude solution.

6.4 Slip at hydrophobic boundaries

6.4.1 Setup

By implementing hydrophobic fluid-wall interaction as described in chapter 4 it is possible to simulate hydrophobic surfaces. For Poiseuille flow this method was intensely tested but a validation for the lubrication force measurement method is missing [48, 8]. Since no surface structure has to be resolved one can use a small $R = 8$ sphere in a 128^3 system, which reduces the required computer power by a factor of 16. In all slip measuring simulations the average fluid density is set to $\eta_{\text{fluid}} = 0.8$, the wall interaction parameter is set to $\rho_w = 1.0$ and the approaching velocity is set to 10^{-3}. The global coupling constant g_{wf} is be varied to steer the fluid-boundary interaction.

6.4.2 Results

Fig 6.9 shows a typical plot of the force F normalized by the Stokes force F_{St} versus the inverse separation R/d normalized by the radius of the sphere. Such a graph suits best to investigate the behavior next to the boundary. The plot shows the asymptotic behavior of the force near the boundary. The black solid line shows the theoretical no-slip curve following Eq. 6.3. The red line shows a fit assuming a slip boundary with the slip length β, by adding the slip correction of Eq. 3.6 to Eq. 6.3.

$$F = \frac{1}{4}\left(1 + 6\frac{d}{4\beta}\left[\left(1 + \frac{d}{4\beta}\right)\ln\left(1 + \frac{4\beta}{d}\right) - 1\right]\right)\left(F_{\text{St}}\left[1 + \frac{9}{8}\frac{1}{d}\right]\right). \tag{6.6}$$

In addition, a fitted force curve is shown that assumes a different boundary position. This boundary is shifted by s. Such a force reads as

$$F = F_{\mathrm{St}} \left(1 + \frac{9}{8} \frac{1}{d - s}\right). \tag{6.7}$$

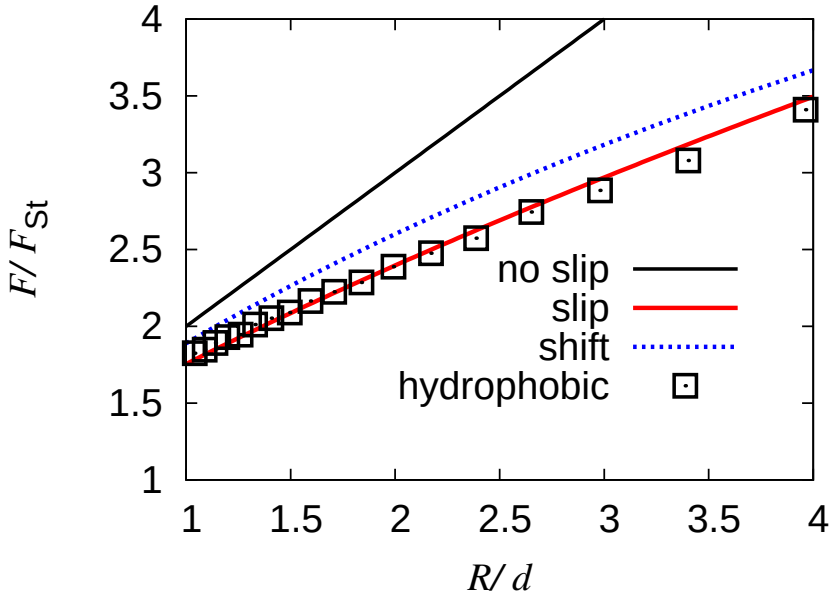

Figure 6.9: Force F versus inverse distance R/d for a hydrophobic surface (squares) The dotted line shows a theoretical curve assuming a no-slip effective boundary inside the wall. The red line shows a fit with a slip assumption. The no-slip curve is shown for comparison.

It is now possible to investigate the influence of different parameters on the lubrication force and on the slip length. Here, we concentrate on the question whether the flow pattern has an influence on the slip length or if it is a more universal parameter to characterize a surface. Therefore, the global interaction parameter g_{wf} is varied and the measured slip length β is compared to the results from a Poiseuille flow geometry, similar to those in [48]. Here, it has to be noted that those methods are absolutely independent from each other. In one case one applies a body force to drive the fluid and measures the flow field, in the second case an object is moved through the fluid and the force on this object is measured. The mechanism to implement the apparent slip does not interact directly, neither with the driving mechanism nor with the measured value. In Fig. 6.10 we plot the slip length β versus the interaction parameter g_{wf}. As shown in a previous publication [48] the slip length increases exponentially. Since the relevant parameters like pressure and hydrophobicity are equal, one can now compare the two methods and find similar results. Beside the influence of the fluid-surface interaction g_{wf} the pressure influences the slip length. A bulk pressure of more than 1.0 only allows slip lengths $\beta < 0.1$ while a pressure of less than 0.8 causes serious numerical instabilities in the lubrication force simulations, because the density fluctuations induced by the jump like movement are to large. Therefore, a deeper observation of the pressure

dependency is not possible. Since the shear independency was shown in Poiseiulle flow, the velocity independency is only checked but not investigated in detail.

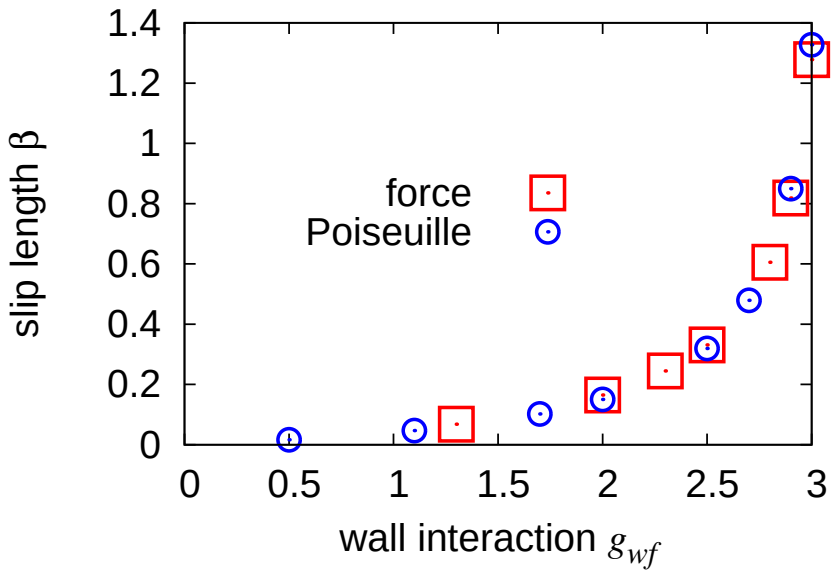

Figure 6.10: Slip length β versus interaction parameter g_{wf}. The plot shows the slip length β measured for a Poiseuille geometry (circles) and the force based measurement (squares). In both cases the slip increases exponentially and gives the same values.

Resume

It was shown that the solution of Maude (6.4) can be reproduced and that at a ratio $R/n = 1/16$ finite size effects are below 2% and can be neglected near the boundary. The findings for the finite size effects are consistent with the findings by Lecoq et al. for a similar system [89]. Further, it was demonstrated that a sphere radius of $R = 8$ provides a sufficient resolution in the case of a plane surface so for further simulations of a flat surface a $128 \times 128 \times 256$ grid is sufficient as long as the region of interest $d \leq 2R$ is less than two times the radius of the sphere. For the simulations of a sphere approaching a rough surface as presented in chapter 7, the spatial resolution becomes more important and therefore a larger sphere is required. The best compromise between computational costs and resolution is a sphere of radius $R = 16$ and a 256^3 grid while keeping the region of interest at $d \leq 2R$.

Based on this calibration the slip generated by a flat hydrophobic boundary was investigated. It was shown that the slip length β measured by different models shows the same dependencies. Further, it is now possible to investigate the influence of a rough surface as it is done in the next chapter.

Chapter 7

Lubrication force on a sphere approaching a rough surface

After the presentation of simulations of a flat surface in the previous chapter which showed that the common theories for Lubrication flow can be reproduced, simulations of a sphere approaching a rough surface are presented in this chapter. Since real surfaces are never perfectly smooth this work has an influence on the interpretation of slip experiments. In tis chapter it are shown that the lubrication force on a sphere approaching a rough boundary cannot be described by a slip correction f^* Eq: 3.6 but by a shift of the effective boundary in a manner similar to chapter 5.

7.1 Setup

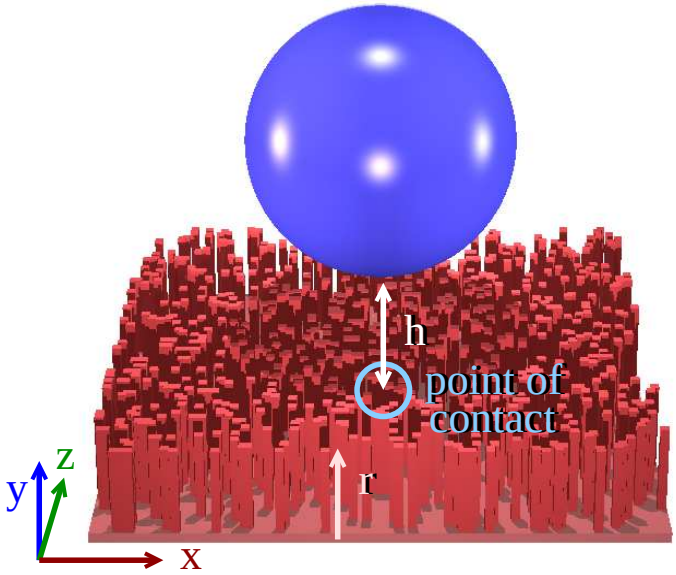

Figure 7.1: Sketch of the system: a sphere with radius R approaches a rough surface where a fixed area fraction ϕ is covered by roughness elements. The separation h is defined on top of the surface roughness at position $y = r$.

Computer simulations provide the opportunity to vary different parameters and

to use different degrees of idealisation. Since the interest lies in lubrication experiments, a sphere that is approaching a rough boundary is simulated, while recording the force acting on this sphere, as depicted in Fig 7.1. Since the separation between the surface of the sphere and the approached boundary is not well defined the following notation is introduced: the distance between the sphere and the highest asperities should be h. The distance measured between the surface of the sphere and the lowest point on the approached surface is d. Further, the roughness heights are measured from the bottom of our roughness as shown in Fig 7.2.

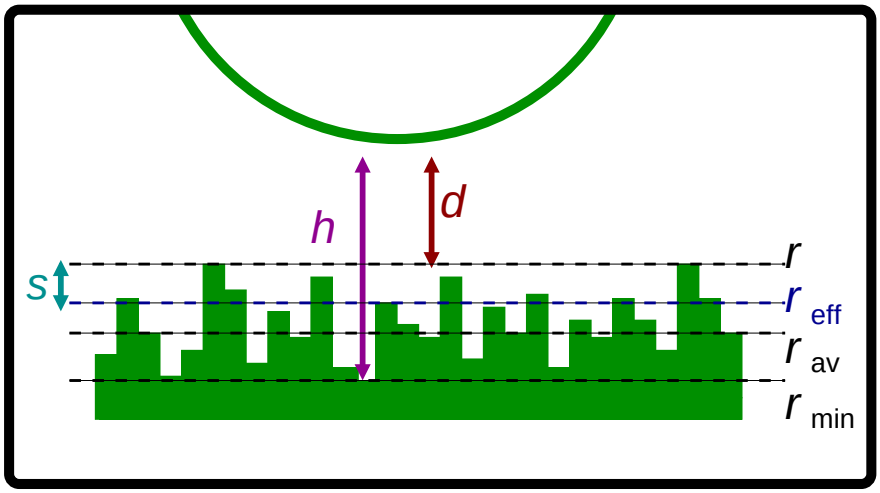

Figure 7.2: Illustration of the different height descriptions. r is the height of the highest peak, $r_{\min}$ the value of the lowest valley of the surface. The average height r_{av} is given by the arithmetic average of all surface positions. The effective height r_{eff} depends on the actual geometry [74].

The interested in this work lies in the influence of roughness on the lubrication force. Some model surfaces are constructed. The chosen roughness variants in the presented study are depicted in Fig.: 7.3. The possible surfaces are elements with an equally distributed random height between 0 and r Fig. 7.3 a, randomly distributed elements of a constant height r with a given surface coverage ϕ, Fig. 7.3 b and grooves with a square cross section so that the width is equal to r Fig.: 7.3 c. The basic idea to describe the boundary is the concept of an effective boundary position were the no-slip assumption holds [74, 78].

As shown in chapter 5 and depicted in Fig. 5.2 the effective boundary is located between the maximum height r and the average height r_{av}, but the actual position has to be determined for each individual geometry. For Poiseuille flow the behavior of the effective boundary position is described in chapter 5 [74] but it is an open question if the previous findings can be applied to the lubrication problem. Here, introducing an effective boundary causes a shift of the force curve. Thus the force acting on a sphere with the velocity v and the fluid viscosity μ is given by

$$F = -6\pi\mu R v \left(1 + \frac{9}{8}\frac{R}{h+s}\right). \tag{7.1}$$

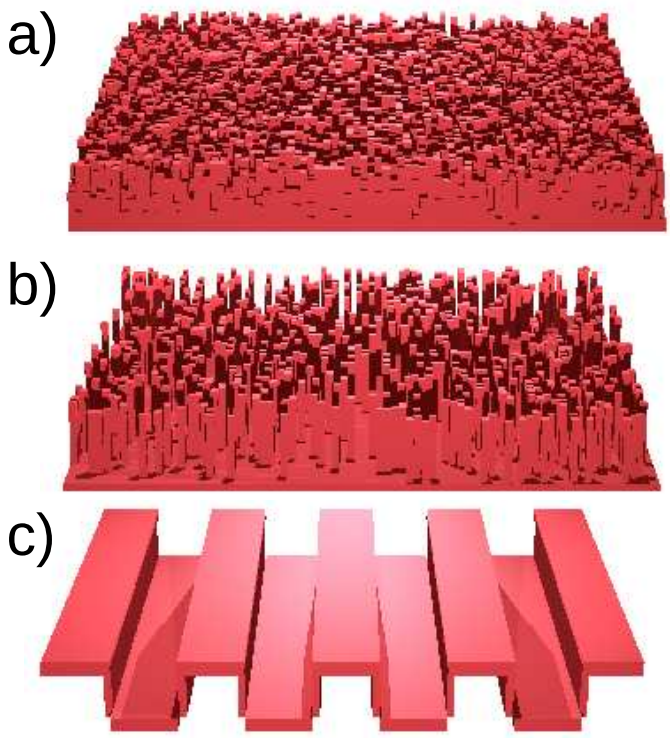

Figure 7.3: The three used surfaces. a) surface with random roughness heights, equally distributed between 0 and r, b) randomly distributed roughness elements with a height r and a roughness density of $\phi = 4\%$. c) grooves with a square cross section and a roughness height of r.

Here, $s = r - r_{\text{eff}}$ is the position of the effective boundary measured from the top of the roughness. For a more clear presentation the distance between the effective boundary and the surface of the sphere is expressed as $d^* = h + s$. Since the force curve is well recorded and only r_{eff} is unknown in our system, it is easy to fit the effective height. As explained in the previous chapter, finite size effects can be handled well if the ratio between system width n and the radius of the sphere R is $n/R \geq 12$. This keeps finite size effects below an acceptable minimum. In the vicinity of the approached surface finite size effects are reduced to less then 1% relative error. Thus, a lattice size of $256 \times 256 \times 256$ with $R = 16$ lattice units is used, if not stated otherwise, in order to keep the computational effort and finite size effects within acceptable limits. All values are in lattice units. The fluid viscosity is fixed at $\mu = 0.1$. The approaching velocity is chosen to be 0.001 lattice sites per time-step. The Reynolds number of this system is therefore $Re = 1.6$ which is high for a micro flow application but is owed to the high velocity that is needed to keep the computational effort acceptable. However, besides that the Reynolds-number is high for microfluidic the flow is still in the laminar regime.

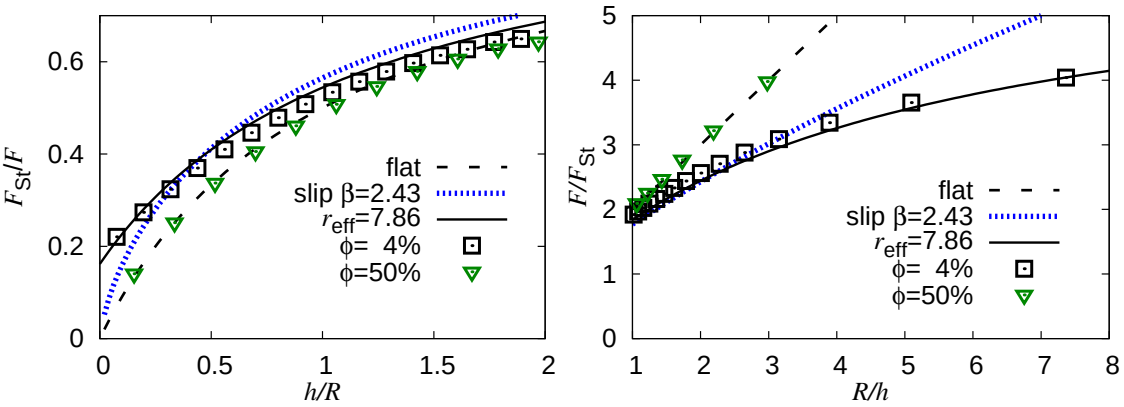

Figure 7.4: Drag force F versus separation h plotted in different coordinates. On the left hand side the inverse force F_{St}/F versus the normalised separation h/R and on the right the normalised force F/F_{St} versus the inverse distance R/h is plotted. They show the measured force for two rough surfaces with $r = 11$, $\phi = 4\%$ and $\phi = 50\%$. For $\phi = 4\%$ the asymptotic behavior for small h cannot be fitted with a slip, but the assumption of an effective boundary position holds. The values for $\phi = 50\%$ nearly recover the case of a flat surface at r. For comparison a fit with a slip theory a boundary shift and a flat surface at the top of the asperities is plotted as well.

7.2 Results

First the effect of roughness is compared with the effect of apparent slip as presented in the previous chapter and it is shown that the assumption of an effective boundary position can be distinguished from a slip surface assumption. Then, it is investigated to what extend the effective boundary assumption holds and whether it differs from the previous results in a Poiseuille flow geometry,

7.3 Comparison of roughness and slip

The focus of this section is on drag force measurements near surfaces with randomly distributed roughness elements as shown in Fig. 7.3 b, where the chosen roughness is characterized by the two parameters r and ϕ. Such a roughness mimic some experiment ally used surfaces, like those utilizing a carbon-nano-tube forest [66]. Further, one is able to generate a well controlled surface with only two parameters, namely the roughness density ϕ and the roughness height r. Since it was shown in chapter 6 that for a hydrophobic surface the theoretical expectations (like Eq. 3.6) are fulfilled simulations of a sphere that approaches a rough surface are presented now.

In Fig. 7.4 left the inverse normalized lubrication force F_{St}/F versus the normalized separation h/R is shown for surfaces with $\phi = 4\%$, $\phi = 50\%$, and $r = 11$, while in Fig. 7.4 right the normalized hydrodynamic resistance force F/F_{St} versus the inverse separation R/h is plotted. Also shown in both plots are the theory for a

flat surface at the highest asperities $r_{\text{eff}} = r$, a fit with a slip theory (Eq. 6.6)

$$\mathbf{F} = \frac{1}{4}\left(1 + 6\frac{d}{4\beta}\left[\left(1 + \frac{d}{4\beta}\right)\ln\left(1 + \frac{4\beta}{d}\right) - 1\right]\right)\left(\mathbf{F}_{\text{St}}\left[1 + \frac{9}{8}\frac{1}{d}\right]\right)$$

, and a fit corresponding to an effective boundary position r_{eff} (Eq. 7.1).

A clear impact of roughness on the film drainage can be observed, but for large separations all data converge towards the Stokes force F_{St}. At smaller separations h, however, substantial differences have to be noted: while for $\phi = 4\%$ the measured forces deviate strongly from the flat surface case, for $\phi = 50\%$ almost no deviation can be observed. The $\phi = 4\%$ case nicely follows a fit with an effective boundary position at $r_{\text{eff}} = 7.86$. Figs. 7.4 also demonstrate that a fit following the assumption of a boundary slip is not able to explain the measured forces. The best possible fit with $\beta = 2.43$ shows a different asymptotic behavior than our simulation data for $\phi = 4\%$. It is still notable that the fitted slip length β is close to the shift $s = r - r_{\text{eff}} = 2.14 \approx \beta$ but shows a significant deviation. The quantified total deviation is small, but the curves shows a different behavior, what leads to the significance of the deviation. Thus, it can be conclude that roughness cannot be treated using a slip correction like Eq. 6.6, but can be treated well by an effective boundary position. Or simply:
slippage and roughness are two different phenomena that have to be treated differently.

7.4 Influence of different parameters

After showing that roughness should be treated by assuming an effective boundary position now the most important dependencies are investigated. The focus lies on the questions weather this has an effect in "realistic" structures and to what extend the assumption of an effective boundary holds. Thereby, the boundary position is characterized as in the chapters before by the effective height r_{eff}.

7.4.1 Resolution

Since it is known from previous sections that there is a principle difference between slip and effective the boundary position, the next interesting question is: at which distance $d^* = h - s$ the theory given by equation 7.1 does break down? This question is very important since the distance between the surface and the sphere comes down to contact in the slip experiments that are tried to cover. It is doubtful weather Eq. 7.1 is applicable for such small distances d, because it assumes an averaged boundary position and local deviations of the surface should have an influence on the local flow field and thus on the force. To investigate this effect simulations with an increasing roughness are performed. This allows to study the behavior of the effective height r_{eff} and one can compare the deviation of the force from the theory (7.1). The chosen standard roughness is a random roughness, where the height at each lattice point is chosen randomly between 0 and r (see Fig 7.3a) and randomly distributed roughness elements with a given height r and a roughness density of $\phi = 8\%$ (Fig 7.3b).

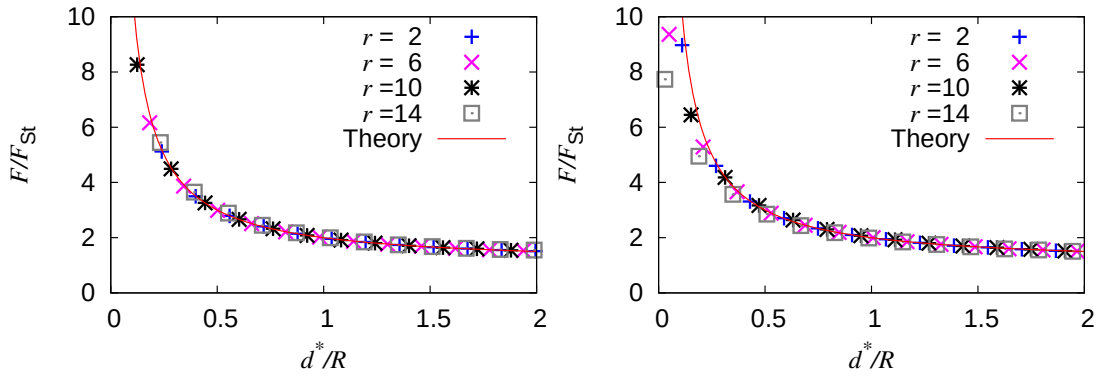

Figure 7.5: Lubrication force F normalized by F_{St} versus the normalized distance d^*/R between the surface of the sphere and the effective boundary for different maximum heights r in a system with random heights (left) and randomly distributed roughness elements $\phi = 8\%$ (right) for different maximum heights r. The theory is given by Eq. 7.1. A deviation of the force from the theory is not found up to $d < 3$ lattice sites. Below this discretization is to strong to give quantitative results.

In Fig. 7.5 the lubrication force F/F_{St} versus the normalized distance d^*/R between the effective height and the surface of the sphere is shown for different roughness heights. The lubrication force F is normalized by the Stokes force F_{St}. The theoretical curve for a plain surface is plotted as well. The force increases rapidly for small distances and converges slowly towards the Stokes force F_{St} for longer distances. This convergence is not shown in the plot since only short distances where the surface-fluid interaction has its main influence, are plotted. The deviation from the theory (7.1) is below 2% at a distance less then $d^* > 3$ lattice sites. Here, it has to be noted that a minimum distance of three lattice nodes is needed to resolve the fluid flow correctly. The error for smaller distances than $d < 2$ lattice sites becomes large but since the fluid field away from the point of contact is resolved sufficiently the strong increase of the force for < 2 lattice sites is still covered by the simulation.

Similar to previous plots the deviations are more obvious in a force versus the inverted distance plot as shown in Fig. 7.6. This can be seen at the error for a flat boundary $r = 0$ in Fig. 7.7. However the astonishing result is that the deviation starts very close to the boundary, so the concept of an effective boundary can be applied for small distances as well.

For a better illustration of the error, the relative deviation δF between the theory (7.1) and the simulation data, is plotted over the effective distance d^* in Fig. 7.7. Note that in this case the distance is given in lattice units and is not normalized by the radius. This is done in order to distinguish weather the deviation origins in a discretization effect or if the physical background does not hold in this case. By plotting the distance in lattice units one can see how strongly the space between the surfaces is discretized. Further it is known from the previous chapter what is the effect of the discretization.

For both kinds of roughness the plots are similar. For the moderate roughnesses of $r < 10$ the relative error of the measured force F towards equation 7.1 is below 2% down to a distance of $d^* > 5x$. At smaller distances the error starts to increase

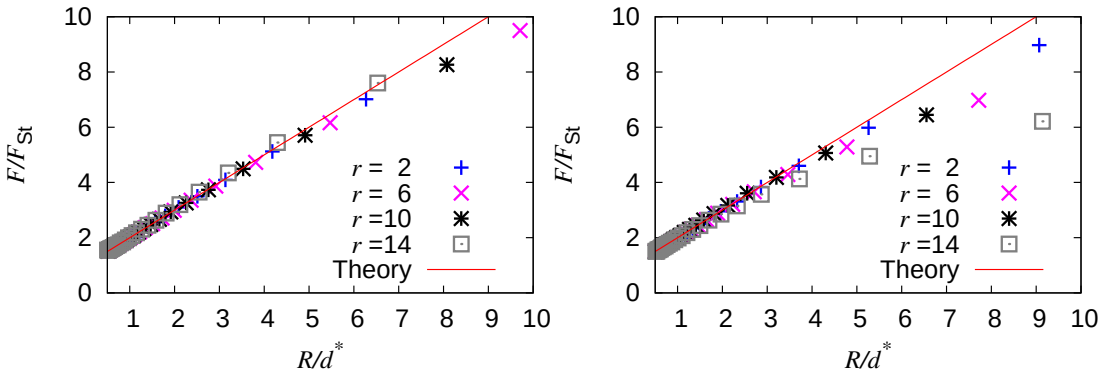

Figure 7.6: lubrication force F/F_{St} versus the inversed distance $1/d^*$ between the surface of the sphere and the effective boundary for different maximum heights r for a system with random heights (left) and randomly distributed roughness elements (right). The asymptotic behavior can be seen better in those coordinates.

significantly. However in this region the influence of the discrete computational lattice become very significant. In addition the distance between the highest asperities and the surface is already below the limit of the simulation method. For the large roughness of $r = 14$ the deviation is more significant. But even in this case the deviation stays under 5% for a distance larger then half the radius of the sphere ($d^* > R/2$) which is below the height of the roughness r. Thus we can conclude that equation Eq. 7.1 holds down to an effective distance $d^* > r/2$ of half the distance within an acceptable limit of 5% deviation, which leads to the next question weather there is an influence of the radius on the validity of Eq. 7.1.

7.4.2 Radius of the sphere

In the case of a flat surface the radius is simply a scaling factor to the force. For a rough surface, however, the ratio between the radius and the height of the roughness R/r changes and therefore similarity arguments do not hold any longer. Thus, it is necessary to investigate the influence of the radius R on the effective height r_{eff}. The two extreme cases are a sphere with an infinitely large radius corresponding to a Poiseuille setup with two infinite planes. The other case is a sphere with a radius smaller than the typical roughness. In the second case it is obvious that the lubrication should depend strongly on the actual shape of the surface at the point of contact and the surface cannot be seen as an averaged effective boundary. To investigate for which parameters the averaging holds we perform simulations with different radii R ranging from $R = 4$ up to $R = 40$. At smaller radii the discretization of the sphere becomes to strong, thus an additional fit parameter for the radius of the sphere is needed. The runs have been performed in a large simulation volume $512 \times 512 \times 512$ to avoid finite size effects and to keep the same geometry. A surface with randomly distributed roughness elements with a height of $r = 10$ and a roughness density of $\phi = 8\%$ is chosen. In Fig. 7.8 one can see that the effective height r_{eff} converges very fast with increasing radius R. Finite size effects might come into play because the ratio R/n becomes too large, so the maximum radius is

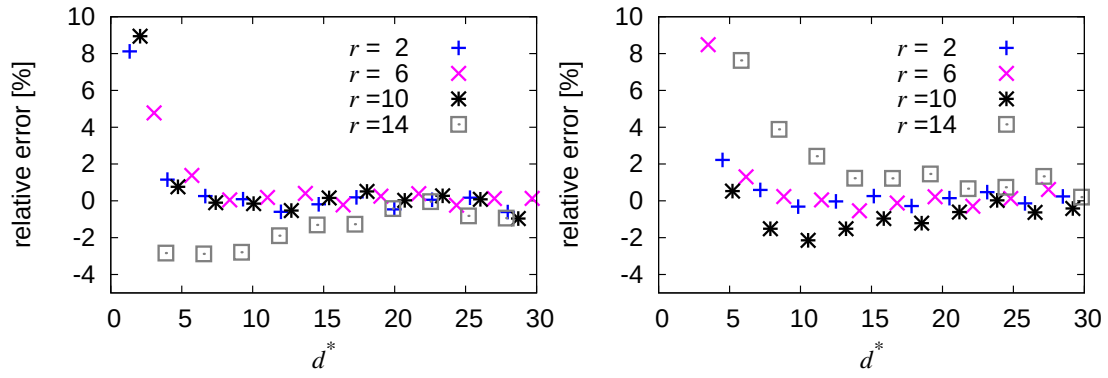

Figure 7.7: Relative error of the lubrication force towards the theory (7.1) over distance d^* in lattice units δx between the surface of the sphere and the effective boundary for different maximum heights r for a system with random heights. The radius of the sphere is 16. For a distance smaller than $d < 3$ discretization effects dominate over the physical deviation

$R = 40$. To avoid errors due to the stochastic nature of the surface, simulations are performed with different points of contact for the smaller radii. In Fig. 7.8 they are displayed with open blue symbols. Due to the periodic boundaries one can choose the x- and z-coordinate arbitrarily, so the averaged values stay the same but the local probabilities of the surface change. This has a stronger influence on the small radii since here the relative deviation towards the average is larger. For a radius of $R > 16$ the effective height is changing within less than 0.1 lattice units, which is about the accuracy of the simulation method. The effective height is increased for smaller radii, but this is independent of the point of contact as one can see in the open symbols in Fig. 7.8. Later in Fig. 7.11 it is shown that the converged effective height r_{eff} for the lubrication is within a tolerance of less then 5% at the same position as the effective height for a Poiseuille flow [74].

7.4.3 Roughness density

The next focus lies on randomly distributed roughness elements as depicted in Fig 7.3b). The influence of the roughness density ϕ is investigated in more detail and the height of the roughness elements is varied from $r = 11$ to $r = 21$ as well. This is done to overcome possible problems with the resolution of the surface. Fig. 7.9 depicts the effective boundary height r_{eff} normalised by the maximum height r versus the covering percentage ϕ. The effective boundary position increases rapidly with increasing ϕ and reaches $r_{\text{eff}} > 0.9r$ for $\phi > 20\%$. For higher ϕ the effective boundary converges slowly towards the height of the elements r. r_{eff} is almost converged at $\phi = 50\%$ which confirms the good agreement of the $\phi = 50\%$ case with a flat surface fit in Fig. 7.4. The fact that the boundary position for $\phi = 50\%$ is already $r_{\text{eff}} > 0.95r$ is only surprising on the first look. It is known from percolation-theory that in case of 50% porosity in 2D there exists no path from one end to the other. Therefore, in the observed case of $\phi = 50\%$ the fluid might not flow within the roughness but must flow over an element in one point.

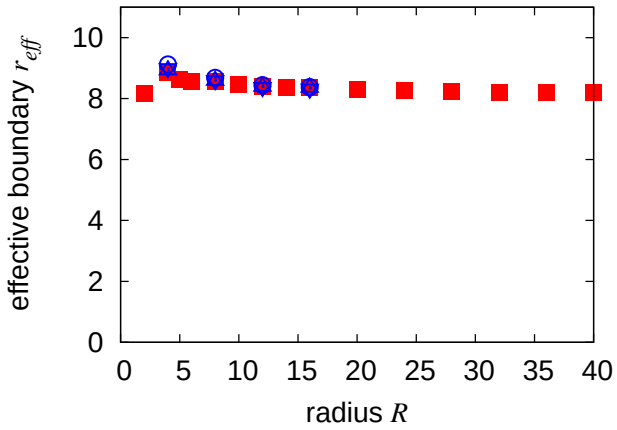

Figure 7.8: Effective height r_{eff} versus the radius of the sphere R for a randomly distributed roughness, at $r = 10$ and $\phi = 8\%$. The blue and open symbols show different points of contact. For radii larger then 16 the effective height is converged. At a radius of $R > 40$ finite size- and transient effects start to disturb the result.

A good agreement between the two values for r can be seen, demonstrating that the resolution has only little influence on the behavior of the measured boundary position. Most notably, this even holds if r is larger than the radius of the approached sphere $R = 16$. The deviation for the low densities has its origin in the strong variation of the local roughness density and the fact that here the flow within the roughness layer is much more dependent on the lower boundary than on the roughness itself. The result shows that a small number of high roughness elements can have a great influence on the lubrication and leads to the conclusion that the influence of surface shape variations has to be very well controlled for high precision microfluidic experiments. This has to be kept in mind when constructing surfaces such as nanotube forests [66, 37, 7], or generally when dealing with roughness in microfluidic systems.

7.4.4 Point of contact

In the following sections systems with a grooved surface are investigated, as depicted in Fig. 7.3c. The main difference between grooves and the random surfaces is that grooves are not isotropic. For a Poiseuille flow setup, this means that there are two possible flow directions, either in the direction of the grooves (longitudinal) or transversal to the groove structure. For sphere drainage this means that the rotational symmetry is broken. A second effect is that the point of contact should become important now due to the anisotropy, i.e. whether the point of contact is in a "valley" or on a "hill". For the simulations grooves with a squared cross section are used. Therefore, the maximum height r and the groove width are identical. To investigate the influence of the variation of the point of contact, simulations are performed with a constant geometry, but the sphere is moved away from the center by a distance δ in steps of one lattice unit. As surface grooves with $r = 10$ are chosen.

Fig. 7.10 right shows the relative deviation $\delta F = F - F_{\text{Maude}}/F_{\text{Maude}}$ between the

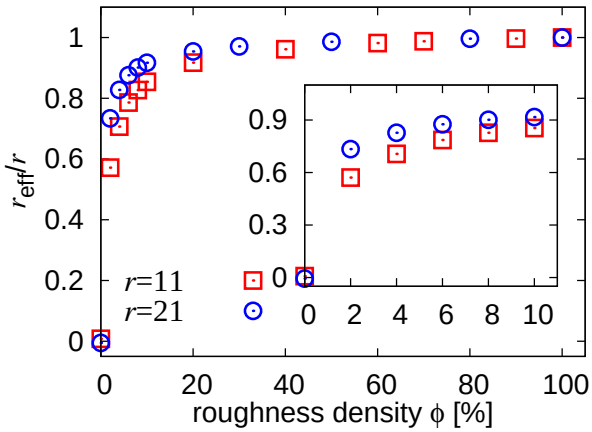

Figure 7.9: Effective height r_{eff} normalized by the maximum height r versus the surface coverage percentage ϕ for $r = 11$ and $r = 21$. The effective height raises quickly with increasing ϕ and converges towards the maximum height r. Due to the geometrical similarity the curves behave identically. The inset shows a magnification of $0\% < \phi < 10\%$

measured simulated force and the theory according to Eq. 7.1 over the distance d^* between the averaged effective height r_{eff} and the surface of the sphere. The average effective height is calculated as the average of each effective height for the different points of contact. The plot shows that at a distance of 6 the deviation becomes smaller than 2%. In addition the plot shows that one single r_{eff} is able to cover all points of contact on this geometry. Here, it has to be noted that the roughness with $r = 10$ is not small compared to the distance d^* and the radius $R = 16$. However, only a small effect of the roughness is seen when it is treated in this way. Therefore, it can be concluded that for the AFM experiments roughness can be treated as a virtual smooth plane as it is suggested by Vinogradova [150] and Kunert [74].

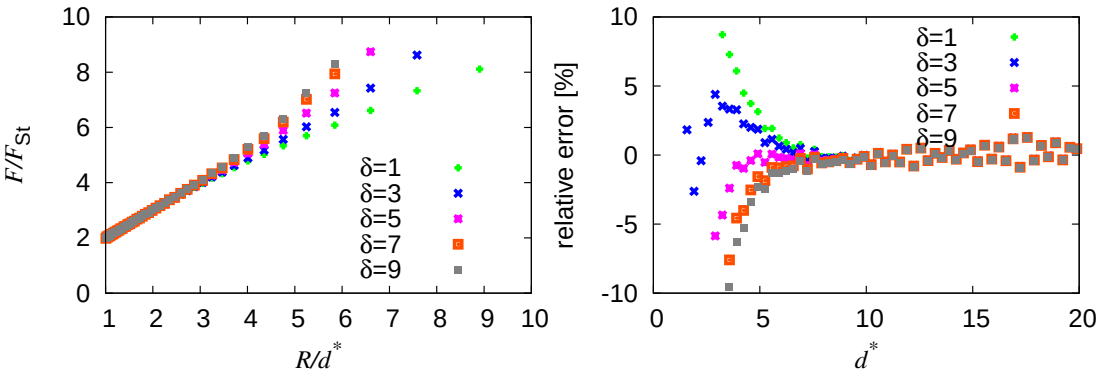

Figure 7.10: Force F/F_{St} versus the inverse distance R/d^* and the relative error of the lubrication force versus distance d^* between the surface of the sphere and the averaged effective boundary for different distances δ towards the center. The height of the grooves is $r = 10$. The plot shows that an averaged effective boundary is applicable, and that the deviation starts shortly before the boundary.

7.4.5 Heights

The position of the boundary as found in our current simulations can be compared to the results for Poiseuille flow [74]. The behavior of r_{eff} with increasing roughness r is investigated,i.e., a geometrically similar boundary with increasing height r is simulated, but the sphere has a constant radius $R = 16$. Since it was showed earlier that the actual point of impact and the radius can be neglected in the cases we are interested in, it is sufficient to perform a single simulation for each height only. As geometries different types of isotropic and anisotropic roughness are chosen. The isotropic ones are random roughness heights between 0 and r as depicted in Fig 7.3 a and randomly distributed roughness elements with a roughness density $\phi = 8\%$ (Fig. 7.3b). Further groved surfaces with a square crossection (Fig. 7.3c) and a triangular crossection are used. Fig. 7.11 shows that the effective height r_{eff} depends linearly on the maximum height r as it is expected and predicted by the Poiseuille simulations presented in [74]. For a comparison, the results generated from Poiseuille flow for a random heights geometry ($r_{\text{eff}} = 0.92r$) is plotted as line into the same plot. The results show that for a random surface geometry the results fit very well within error bars, which are of the size of the symbols. At the non-isotropic groove surface, the results for the lubrication method are between the values for longitudinal and the transversal Poiseuille flow, which are not shown in order to keep the visibility. The lubrication flow has components in both directions thus it is obvious that the position of its effective boundary is in between the effective boundary for the both extreme cases. The actual position of r_{eff} is slightly higher than the average between the longitudinal r_{eff} and the transversal effective boundary height r_{eff}.

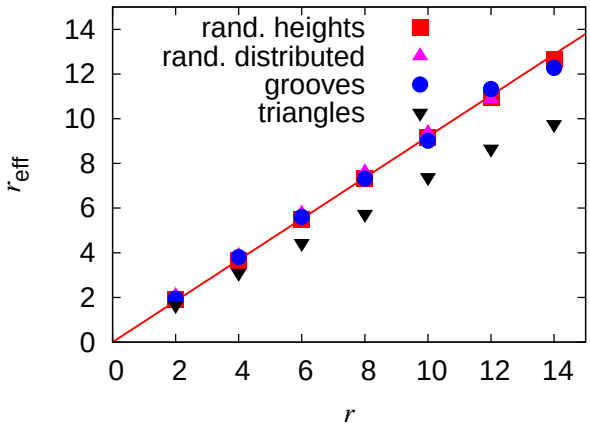

Figure 7.11: Effective height r_{eff} versus the maximum height r for different surface geometries. The line is for Poiseuille flow, points for lubrication flow. In the case of an isotropic random surface both methods lead to the same effective height while the non isotropic grooves lead to an intermediate result.

Resume

In this chapter it is shown that the idea of an effective boundary is applicable even for roughness that is not small compared to the radius of the sphere R or the effective distance d^* between the surface of the sphere and the boundary. Further, it is shown that the effective height r_{eff} of the lubrication-based simulations is in good agreement with the results from Poiseuille flow simulations in chapter 5. Further it was shown that only a small fraction of roughness elements can result in an effective boundary close to the highest point of the asperities.

The results show that surface roughness plays an issue in AFM-based slip experiments but it can be treated in an easy manner by shifting the boundary and surface position.

Chapter 8

Super-hydrophobic surfaces

As shown in chapter 3, the combination of hydrophobicity and roughness can lead to so-called super-hydrophobicity. The understanding of this effect is very limited and, both, experimental and analytical approaches, are difficult. Since a large reduction of the friction close to the boundary is expected at super-hydrophobic surfaces, they are technologically interesting. In the previous chapters the influence of roughness on the flow close to the surface was discussed. The next step is to investigate which effect the combination of roughness and hydrophobicity has on the slip length β. Therefore, it is of interest to investigate the flow over bubbles that are trapped in the surface topology. In this chapter the construction of super-hydrophobic cells is presented. A whole surface can be formed by an array of such cells that is realized by applying periodic boundaries. This enables the discussion of preliminary results of fluid flow in the vicinity of such an array of unit cells. A slip effect is found, and compared to analytical and experimental results.

8.1 Creation of a super-hydrophobic surface in the lattice Boltzmann method

Before it is possible to investigate the behavior of super-hydrophobic surfaces it is necessary to find a suitable setup. Due to the improved stability and the lower computational effort, a Poiseuille flow setup is chosen. The flow is driven by a force f_x in x direction, which is equivalent to a pressure gradient $\frac{\partial p}{\partial x}$. In z direction simple periodic boundary conditions are applied. Two surfaces, with a distance in between them of $2d$ in the y dimension, form the remaining boundary. The upper plane is hydrophilic (i.e. no slip BC) while the lower one consists of one super-hydrophobic unit cell of the length L in x direction. Due to the periodicity only one cell is needed to represent the whole surface. As described in chapter 4 a Shan-Chen model is able to model a liquid-gas phase-transition. As reminder, in the model a force that is directed opposed to the density gradient is applied to generate a phase separation between a lighter (gas) and a denser (liquid) phase. The Shan-Chen force $\mathbf{f}_{SC}$ in a single component system is given by Eq. 4.64

$$\mathbf{f}_{SC} = \Psi(\rho(\mathbf{x}))g\sum_i \mathbf{c}_i\Psi(\rho(\mathbf{x}+\mathbf{c}_i))$$

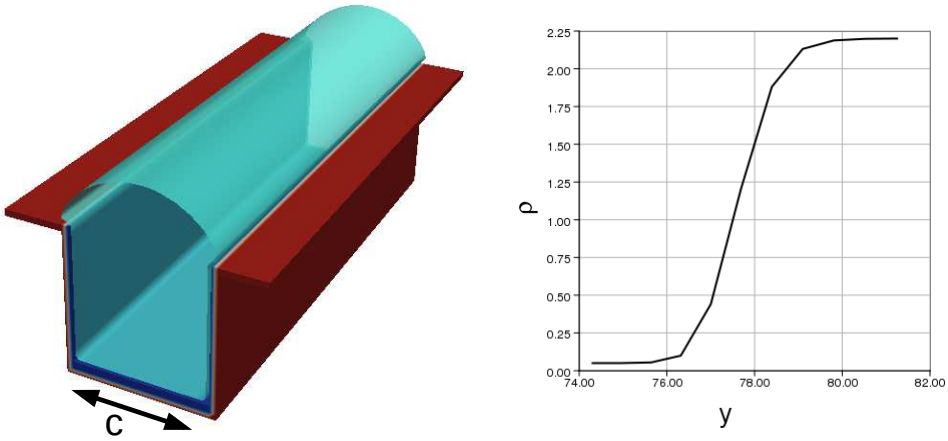

Figure 8.1: 3D visualization of a grooved surface. The width of the unit cell is L and the width of a groove is defined by c. The red surface shows the boundary, while the light blue bubble is given by an isosurface for $\rho = 0.1$, i.e., it lies in the interface layer between the liquid and the vapor phase. The right plot shows a density profile in the interface layer. Here, the density changes within five lattice sites from $\rho_{\text{gas}} = 0.05$ to $\rho_{\text{liq}} = 2.26$.

with the effective mass $\Psi(\rho) = 1 - \exp(\frac{-\rho}{\rho_0})$ being a function of the fluid density $\rho(\mathbf{x})$ at position $\mathbf{x}$. $\rho_0 = 1$ is a reference density. The coupling constant g has to be chosen carefully to achieve a large density difference between the dense (liquid) phase and the light (gas) phase. For this work it was set to a value of $g = 5.5$ which leads to a stable dense phase of $\rho_{\text{liq}} = 2.26$ and a stable low density of $\rho_{\text{gas}} = 0.05$ resulting in a density ratio of $\rho_{liq}/\rho_{gas} = 45.2$ which is close to the maximum that was reported for diffuse interface lattice Boltzmann methods (Shan and Chen only reported a density difference of $\rho_{liq}/\rho_{gas} = 10$ [124]). The interface layer requires five lattice sites as it is shown in the density profile in Fig. 8.1, right.

To model a phase transition close to the boundary it is necessary to introduce a fluid-boundary interaction, like it is done for the hydrophobicity in chapter 5. Unlike to that approach one now needs a single component system and therefore, the boundary now carries a virtual fluid-density $\rho^{w'}$. To induce a vapor phase close to the hydrophobic boundary, $\rho^{w'}$ should be set to a value close to the vapor density, i.e., $\rho^{w'} = 0.05$ for hydrophobic walls. Since the desired behavior is to have a vapor bubble attached at the surface, it is necessary to have hydrophilic parts in the system that keep the bubbles in place. They are realized by setting the virtual fluid density in the boundary to a very high value of $\rho^{w'} = 3.05$. This contact line pinning is needed to keep the bubble in place and not to simulate one that starts to move through the system.

To investigate the behavior of a gas phase pinned to the boundary two different geometries are investigated, which are proposed in the literature [42]. The first one consists of grooves as shown in Fig. 8.1. If not stated otherwise, the grooves have a width of $c = 20$ lattice notes, the inner part of the groove is hydrophobic ($\rho^{w'} = 0.05$) and therefore filled with vapor. The grooves occupy the whole width of the system, making them due to the periodic boundaries infinite cylinders, instead

of round spherical bubbles[1]. Depending on the bulk pressure a meniscus is formed as depicted in Fig. 8.2. The angle that is formed between the meniscus and the surface is called the protrusion angle φ. Note that the bulk density is kept constant, since there is a coexisting between the vapor and the liquid phase. The protrusion angle φ is measured by fitting a circle towards the bubble. By this one can determine the angle that is formed between the tangent on the circle and the surface. Since the bubble interface is diffuse, the actual circle and therefore the protrusion angle φ is not unique, which leads to an error in the protrusion angle measurement, which influence is discussed later.

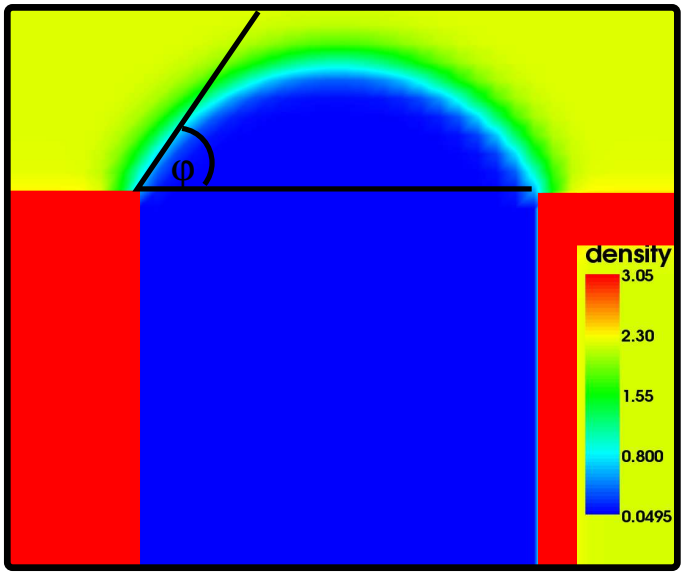

Figure 8.2: Cross-section of a grooved unit cell. The colors indicate the density ρ, i.e. blue stands for low density (vapor) and orange for high density (liquid). The solid boundary is red. The protrusion angle $\varphi = 30°$ is formed between the surface and the bubble.

Such a grooved system has the advantage that one needs only a small simulation volume when observing Poiseuille flow, since one can apply periodic boundary conditions to the non wall sides, which allows to keep the simulated system as small as $L = 40$ lattice nodes perpendicular to the grooves, $2d_{\max} = 134$ lattice nodes between the two planes in y direction, and a width of only $w = 4$ lattice nodes, since the system is a quasi 2D system. A similar system was investigated in the experiments by Tsai et al. [142]. They investigated the flow field over grooves filled with water, using the micro PIV technology and presented different flow profiles. The behavior of the slip length from different geometrical parameters was investigated and it was concluded that the behavior of the slip length β cannot be explained by the theory of Philip [109]. Their explanation is that due to the meniscus, formed at the grooves the no-shear (i.e. full-slip) parts develop an additional drag, similar to the effect reported by Richardson who showed that a rough no-shear surface creates sufficient drag to obtain macroscopically a no-slip boundary [114]. Further,

[1]for simplicity the infinite cylinders are called bubble as well.

Davis and Lauga developed a theoretical model valid for grooves covered with no-shear "bubbles", to describe the slip length β in dependence on the protrusion angle φ [32]. The main idea is that there is a no-shear meniscus on a no-slip plane. In such a system two opposing effects can be observed: the larger the meniscus gets, the longer the fluid is accelerated, but the stronger the drag becomes due to the surface roughness created by the bubble. Their main result can be summarized as follows: there exists a critical protrusion angle φ_c above which the effect of the wall-attached bubbles displays a transition from reduced to enhanced fraction, i.e. the slip length β becomes negative. They predict this angle to be $\varphi_c = 65°$. They predict as well a maximum protrusion angle $\varphi_{\max}$ at which the drag reduction is maximized. This angle depends on the ratio between the no-slip and the no-shear part, however, for equally long no-slip and no-shear parts the maximum protrusion angle is $\varphi_{\max} = 25°$. Interestingly, they predict as well that for negative protrusion angles there is no negative slip length.

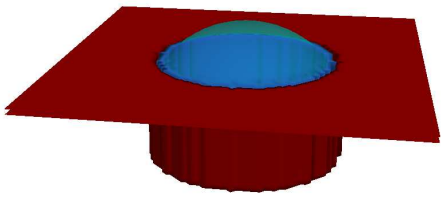

Figure 8.3: Illustration of a 3D unit cell for a large bubble. The red surface shows the boundary, while the light blue bubble is given by an isosurface for $\rho = 0.1$, i.e., it lies in the interface layer between the liquid and the vapor phase.

A different, three dimensional, super-hydrophobic cell is given by a circular cylindrical hole with hydrophobic inner walls. A bubble is formed inside the hole. In Fig. 8.3 the red surface shows the boundary of a cylindrical hole with an inner radius of $R = 18$ in a 80×80 lattice units large cell. The light blue bubble is created by showing an iso-surface for a density of $\rho = 0.1$, i.e., a value to depict the interface layer between the vapor bubble and the liquid. Such a model was investigated by Hyväluoma and Harting using lattice Boltzmann simulations of Couette flow in the vicinity of such a surface [59]. They found a shear dependent slip length, which has its origin in the deformation of the meniscus. In contrast to the results by Davis and Lauga they found the maximum slip length at a protrusion angle of $\varphi_{\max} = 0°$. However, the qualitative behavior is the same namely that at a critical protrusion angle $\varphi_c \approx 65°$ the slip length becomes negative. However, there is a principle difference between the works: Hyväluoma and Harting investigate 3D structures, while Davis and Lauga's calculations are valid for a quasi 2D structure.

To investigate the flow over the presented surfaces, a Poiseuille flow setup is chosen in this chapter. In contrast to the previous chapters one surface consist of a single super-hydrophobic unit cell and the other surface is a flat no-slip surface. The distance between the two surfaces is chosen as $2d = 134$. This distance has to be large compared to the height of the bubble, because otherwise the bubble disturbs the bulk flow strongly, making it impossible to define an averaged effect of the super-hydrophobicity. The flow is driven by a constant body force. This is a

difference towards a Couette flow setup since the body force f_x acts as well inside the bubble and additionally accelerates the vapor. The slip length is measured in the same way as in chapter 5, namely by fitting the theoretical flow profile, which includes the slip length, towards the simulated data. Since one plane has a no-slip boundary condition it is not possible to apply Eq. 5.1 where two equal slip-planes are assumed. Instead a flow profile is used, which assumes no slip $v(y = 2d) = 0$ at the upper boundary and a slip boundary condition $u(y = 0) = \beta \frac{\partial v}{\partial y}|_{y=0}$ at the lower surface. Such a profile reads as

$$u_x(y) = \frac{d^2}{2\mu} \frac{\partial p}{\partial x} \left[\frac{y^2}{2d^2} - \frac{y}{d+\beta} - \frac{\beta}{d+\beta} \right]. \tag{8.1}$$

The viscosity is kept at a value of $\mu = 0.1$. Since the cross-section of the channel is not constant, it is again necessary to average over many flow profiles. In this case it is possible to average over the length of a whole unit cell L what is, due to the periodic boundaries, the total average velocity.

8.2 Results

In this section the preliminary results of flow over an periodic array of the presented super-hydrophobic unit cells are presented and compared with experimental and analytical findings. A slip effect is detected and several dependencies are studied.

8.2.1 Flow profiles

A surface structure that has been studied both experimentally and theoretically in great detail consists of longitudinal grooves etched in a smooth surface. If such grooves are hydrophobic, they can be filled with vapor forming cylindrical bubbles that are surrounded by liquid. The surface between individual grooves is hydrophilic causing an effective pinning of the three-phase contact line.

A similar system was investigated in the experiments by Tsai et al. [142]. They studied the flow field over gas filled grooves oriented in flow direction by using micro particle image velocimetry (micro PIV). In [142] they presented measured flow profiles and the corresponding effective slip lengths. There work showed, that there is a significant difference between the flow over slip-no slip stripes and the flow over a bubble surface. As well there system shows a disturbance in the flow profile that is dumped quickly.

Following the work of Tsai et al. simulations of flow over grooves oriented in flow direction are presented. The width of the groove is chosen to be $c/L = 0.5$. The protrusion angle in the experiments and in the simulations is chosen to be $\varphi = -10°$, i.e., the liquid-gas interface forms a dimple rather than a bubble. The meniscus increases the vapor covered area (no-shear surface) but also introduces roughness that leads to a higher friction and therefore a reduced slip. In Fig. 8.4 the flow profile over one groove for different distances from the surface is shown. At a very close distance $x = 0.25c$ the bubble has a strong influence on the flow, since the velocity in the centre of the groove is more than twice as large as the

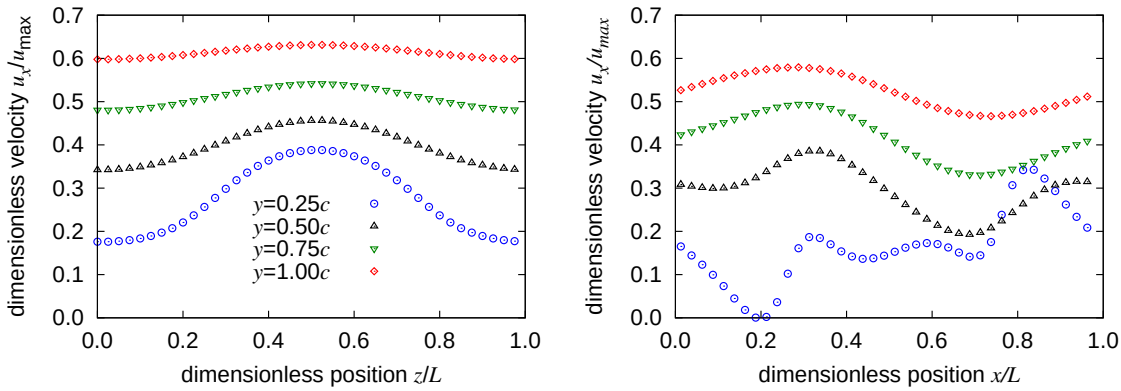

Figure 8.4: Flow profile perpendicular to the grooves for flow parallel (left) and perpendicular (right) to the grooves at different x positions over the surface. The groove is located in the centre of the system between $0.25L$ and $0.75L$. In the left panel a strong increase of the velocity in close vicinity to the bubble can be seen that relaxes within $1.0c$ to an almost undisturbed flow. The right plot demonstrates that flow perpendicular to the grooves causes more significant disturbances, which get still damped rather quickly.

velocity in the centre of the void space. This effect is damped very quickly, i.e., at $x = 1.0c$ the velocity increase in the area above the bubble is less than 10% compared to the undisturbed case. The strong damping allows the treatment of such a grooved surface as a surface with an effective boundary position as long as the typical channel width d is larger then the system length L. The flow profiles are consistent with the results of Tsai et al. who also found a strong increase of the velocity above the grooves that is damped strongly further in the bulk. Further, the measured and the simulated slip lengths β/L are of the order of half the theoretical prediction by Philip [109]. The reason for this is the assumption of a flat surface with stripes of no-slip and no-shear, while in the case of vapor filled grooves a meniscus is formed introducing an additional roughness that reduces the slip of the fluid over the surface.

In order to compare the results to the theoretical results of Lauga and Davis [32], grooves which are oriented perpendicular to the flow are considered. In the right panel of Fig. 8.4, the flow profile in the vicinity of a perpendicular groove as it is assumed by the theory is shown. Interestingly, here the flow velocity does not increase as strongly as in the aligned case above the groove but right after it. Again, a deceleration in front of the groove can be observed and the flow profiles are not symmetric towards the centre of a unit cell which is caused by the driving direction of the flow. The disturbances caused by the bubble are not damped as quickly as in the case of longitudinal grooves. For example, even at $y = 1.0c$ the flow velocity changes between $0.45u_{\max}$ and $0.59u_{\max}$. Further the disturbance close to the boundary is much stronger. At $x = 0.25c$ one can see a strong decrease of the velocity at the beginning of the groove and a strong increase at the end. The reason is the dimple shape of the meniscus. This leads to a compression of the streamlines at the end of the meniscus which is equivalent to an increased velocity. The dependence of the slip length on the orientation is consistent with the work of Bazant et al. who have

shown for flat stripes that a generalized tensor form would be required to describe the surface properly [7].

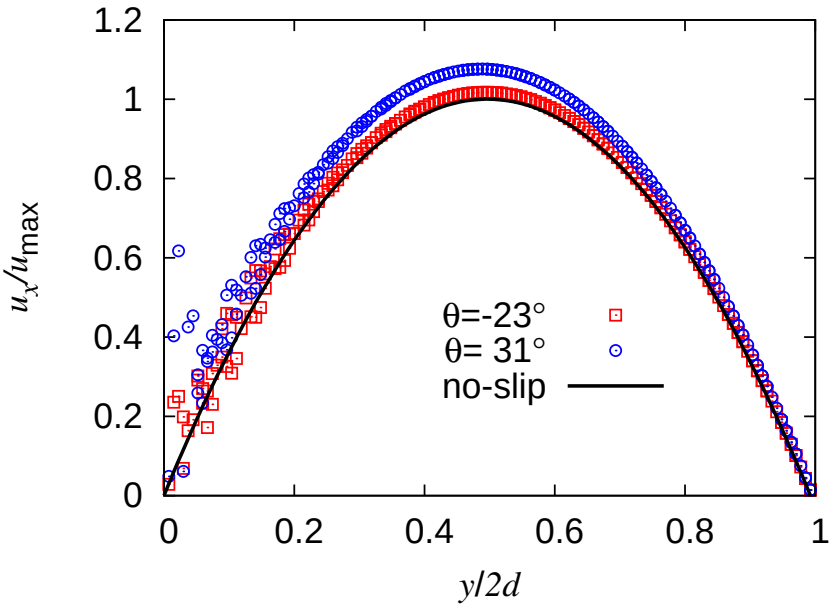

Figure 8.5: Flow velocity profiles perpendicular to the flow direction $u_x(y)$ for $\varphi = -23°$ (red) and $\varphi = 31°$ (blue). For comparison the theoretical no-slip profile is plotted as well. For each protrusion angle the cross-section at $y = \{0...20\}$ is plotted leading to the strong deviations close to the super-hydrophobic boundary. The protrusion angle has a strong influence on the maximum velocity which can be explained by a protrusion angle dependent slip length $\beta(\varphi)$.

After the flow profile in flow direction the cross-section perpendicular to the flow direction is investigated. In Fig. 8.5 the flow profiles for $\varphi = -23°$ and $\varphi = 31°$ are shown. The first one is chosen since it shows a similar protrusion angle as the experimental data from Tsai et al. The second value $\varphi = 31°$ is chosen because here the maximum slip can be detected. In the plots all x-positions in flow direction are plotted. Close to the bubble boundary the velocity shows strong variations which are a result of the acceleration and deceleration due to the bubble. The two velocity profiles follow a Poiseuille flow solution as shown in Eq. 8.1 but show different slip lengths β. Therefore, it is possible to determine the slip length β by a fit towards the flow profile. Further, the protrusion angle dependence of the slip length can be investigated.

8.2.2 Slip near super-hydrophobic surfaces

The shape of the meniscus has a significant influence on the slip length. The above mentioned analytical approach of Davis and Lauga described the effective slip length in dependence on the protrusion angle φ on a surface with grooves perpendicular to the flow direction [32]. The theory assumes rigid bubbles with a full-slip surface, which corresponds an infinitely thin liquid-gas interface and vanishing gas density.

In this case the slip length is given by

$$\frac{\beta}{c} = \pi \left(\frac{c}{L}\right) \int_0^\infty A(s)\mathrm{d}s, \tag{8.2}$$

with

$$A(s) = \frac{s}{\sinh 2s(\pi-\varphi) + s\sin 2\varphi} \times \left[\cos 2\varphi + \frac{s\sin 2\varphi \cosh s\pi + \sinh s(\pi - 2\varphi)}{\sinh s\pi}\right]. \tag{8.3}$$

The only parameters entering the calculation of the effective slip length β are the protrusion angle φ and the ratio between the width of a groove c and the length of a unit cell L. The actual values of the slip length have to be calculated numerically.

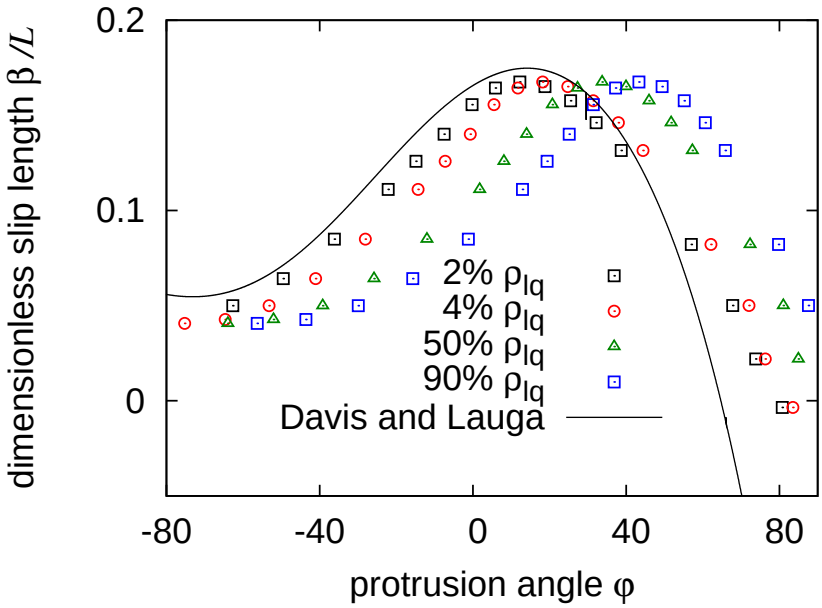

Figure 8.6: Slip length versus protrusion angle φ for different threshold values. The groove has a width of $c = 30$ and the system length is $L = 40$. Since the multiphase lattice Boltzmann model used is a diffuse interface model, the protrusion angle is not defined uniquely but depends on where the actual interface position is assumed, i.e. which threshold ρ_t is chosen. Due to the non perfect slip on the vapor phase the analytical solution by Lauga et al. is scaled down by a factor of 0.75.

In Fig. 8.6 the dimensionless slip length β/L versus the protrusion angle φ is shown as given by Eq. 8.2 and by the simulation. The system length in this case is $L = 40$ lattice units and the width of a groove is $c = 30$ lattice units. Since the interface between the vapor and the liquid is diffuse, the actual bubble position is not strictly defined. This is in contrast to the theoretical solution and renders the determination of the protrusion angle difficult. Therefore, different threshold values ρ_t for the fluid density at the interface are chosen to determine the protrusion angle. This value has to be somewhere between the high (liquid) density $\rho_{liq} = 2.2$ and the lower (gas) density $\rho_g = 0.05$. In Fig. 8.6 the effect of choosing different threshold values between $\rho_t = 0.02\rho_{\mathrm{liq}}$ and $0.9\rho_{\mathrm{liq}}$ is demonstrated. Here, it can be observed

that a variation of the threshold can lead to a shift in the protrusion angle of more than 20°.

A comparison of the simulation data to the results of Davis and Lauga Eq. 8.2, shows that the qualitative shape of the curve is well reproduced, i.e., the slip length first increases with rising φ up to a maximum at $\varphi_{\max}$ and then follows a steep decrease for high φ. It can even become negative. However, in addition to the possible variation of φ a second deviation between theory and simulation is found: the detected slip length b is lower than predicted by Davis and Lauga. To be able to compare theory and simulation, the theoretical values are scaled by a factor of 0.75 to fit the data. This can be explained by the fact that the diffuse interface must not be described by a smooth full slip cap. Instead it shows a finite slip due to the friction within the interface region. Further, the density ratio between liquid and vapor is limited in the lattice Boltzmann model used. In the presented case it is only 1/44. Therefore, the shear resistance on the bubble surface is only reduced by this factor, while in a real system consisting of, e.g., water and air, this ratio would be of the order of 1/1000 rendering the assumption of no shear more realistic. Apart from the shift due to the finite interface width, the simulation is able to recover the main conclusions from the theory, namely the strong dependence on the protrusion angle φ.

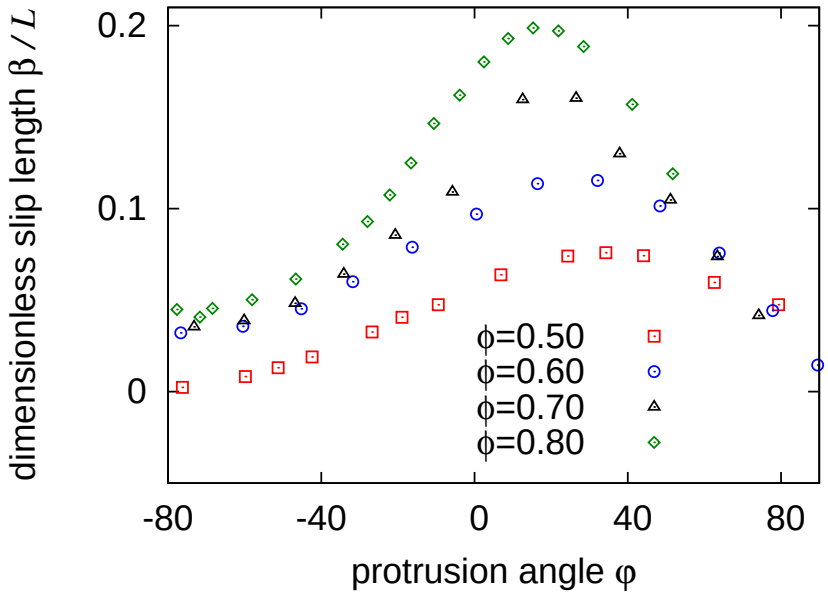

Figure 8.7: Normalized slip length b/L versus the protrusion angle φ, for different ratios between the width of the grooves c and the system length L. The behavior is similar to the prediction of Eq. 8.2. Further, a larger $\phi = c/L$ leads to a strong increase of the slip length.

Further the influence of the area covered by the bubble $\phi = c/L$ on the slip length is investigated. Different channel widths are considered for different protrusion angles φ. The threshold value determining the interface position was chosen to be $\rho_t = 0.04\rho_{liq}$. A lower threshold would be beneficial, but is hard to realize, since in some cases this leads to an undefined protrusion angle. Results are shown in

Fig. 8.7. The qualitative behavior of the results again follows Eq. 8.2. The maximum slip length is increased very strongly by increasing the relative width of the groove. An increase of the surface coverage from $\phi = 0.5$ to 0.8 leads to an increase of the dimensionless slip length where the values for the respective maxima range from $b/L = 0.07$ to 0.19. Such a strong increase is also predicted by Eq. 8.2. Further, due to the influence of the increased roughness for $\varphi > 60°$ the slip length becomes smaller for larger φ. Also for $\varphi < -40°$ the slip becomes smaller than $b < 0.05L$ and nearly independent on the surface coverage ϕ.

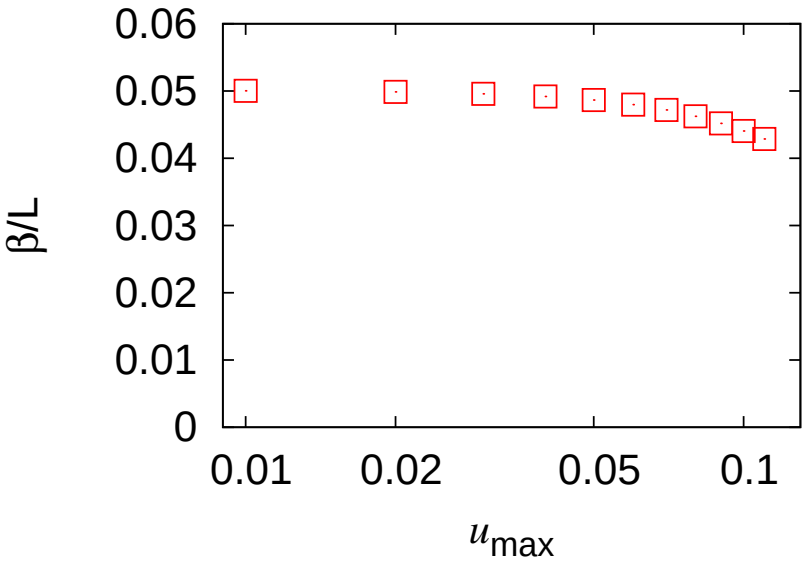

Figure 8.8: Normalized slip length β/L versus the maximum flow velocity $u_{\max}$ plotted on a logarithmic scale. Due to the deformation the slip length decreases at high velocities.

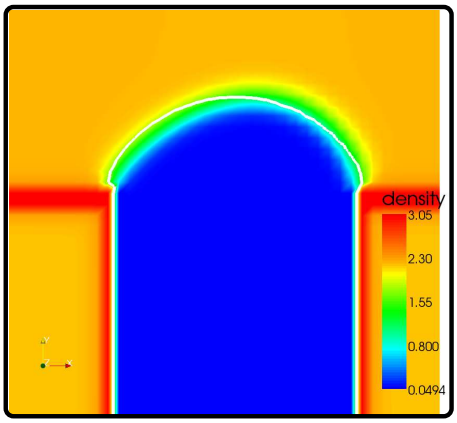

Figure 8.9: Density in a deformed bubble. The white line shows the contour of an undeformed bubble.

Finally, the shear rate dependency of the slip length is analyzed. Hyväluoma and Harting [59] found a shear dependency due to the deformation of the bubble under

shear, that results in a decreasing slip length. In the Poiseuille flow setup a shear dependency would mean a flow velocity dependency. Therefore, simulations on a groove geometry with different maximum flow velocities ranging from $v_{\max} = 0.0001$ to $v_{\max} = 0.12$ are performed. As protrusion angle $\varphi = 55°$ is chosen since the bubble has to range sufficiently far into the system in order to be deformed. Further, the slip length of $\beta/L = 0.05$ in this system is still sufficiently large to see any deviations[2]. The results are shown in Fig. 8.8. Here, the reduction of the slip length from $\beta/L = 0.05$ down to $\beta/L = 0.04$ is observed. A further reduction could not be observed for two reasons. The first is that a velocity of $u_{\max} > 0.12$ results in too high Mach numbers. Since the lattice Boltzmann method, as it is presented, is only valid for non compressible fluids, the simulation method could not be applied at higher Mach numbers. The second reason is the small deformability of the bubble. To increase it, a larger bubble should be simulated. To show the deformation in Fig. 8.9 the density profile for the bubble at $v_{\max} = 0.12$ is shown. For comparison, an isosurface of the boundary layer of an undeformed bubble is shown as a white line. As far as the results can be compared the shear dependency is consistent with the findings of Hyväluoma and Harting. In their work the reduction at higher shear rates is more dramatic, because the bubbles are less stiff since they are larger.

Resume

In this chapter Poiseuille flow over super-hydrophobic surfaces is applied to investigate the behavior of the slip length on different parameters. Mainly vapor filled grooves are investigated which can be compared to the theoretical work of Davis and Lauga [32] and the micro PIV experiments by Tsai et al. [142]. Further, a single bubble similar to the simulations of Hyväluoma and Harting [59] is investigated. It was shown that the flow profiles are in good agreement with the experimental findings of Tsai et al. [142]. Further, the dependence of the slip length on the protrusion angle is compared with the theoretical work. Here, a very good agreement in the critical protrusion angle φ_c and the angle of the maximum slip length $\varphi_{\max}$ was observed. Finally, it is possible to show that a deformation of the bubble under shear leads to a decreased slip length.

[2]Note that the absolute slip length is $\beta = 0.05 \times 40 = 2.0$ lattice units

Chapter 9

Conclusion

This thesis focuses on lattice Boltzmann simulations of the influence of roughness and hydrophobicity in microfluidic systems. Therefore, typical experimental setups like Poiseuille flow and a lubrication force measurement experiment are simulated. Unlike typical idealizations, the investigated surfaces can be randomly rough instead of being perfectly smooth or having only a simple periodic roughness. Due to this increased realism, this work gives a deeper insight, how roughness and hydrophobicity have to be treated in the data analysis of experiments.

In chapter 3, an overview on the slip phenomenon is given. It can be said that the field of microfluidics provides a variety of interesting physical phenomena that are hard to describe by analytical theories. Experimental results on slip phenomena are often inconsistent with each other, which makes a common understanding hard to achieve. Computer simulations can help to draw a clearer picture of slip phenomena. However, the simulation method has to be chosen carefully. Classical CFD methods need a founded analytical theory to model sub continuum effects. Since such a theory is missing, they are less helpful in the case of micro-fluidic slip phenomena. Molecular dynamics has the advantage that it can utilize first principles, but suffers form a large computational effort. Therefore, the time and length scales one can achieve by these methods are too small. A possible solution are so-called mesoscopic methods.

Chapter 4 gives an overview on the lattice Boltzmann (LB) method that is utilized in this thesis. By using a discretized version of Boltzmann's equation, the LB approach allows to fully resolve the hydrodynamics [129].

Massive particles are described by a continuously moving boundary which is discretized on the lattice. Momentum from the particle to the fluid is transferred such that the fluid velocity at the boundary equals the particle's surface velocity. Since the momentum transferred from the fluid to the particle is known, the hydrodynamic force can be recorded. Hydrophobic interactions and liquid-vapor phase separation are modeled by a Shan-Chen approach. In short, this is a force that is proportional to the local fluid density and the neighboring, or a virtual boundary density.

By applying a Poiseuille flow setup between rough boundaries, it is possible to demonstrate in chapter 5 that not properly taking into account surface structures of confining geometries can lead to substantial misinterpretations of measured flow properties. It is demonstrated that rough surfaces alone can lead to large apparent

slip if the distance between boundaries is small [74]. These findings show that the concept of an imaginary effective plane where the no-slip boundary condition is valid, is a good description of a rough boundary. The results are compared to analytical calculations of Panzer et al. and found to be in good agreement for small variations. Large and more realistic perturbations can only be covered by simulations as presented here. By simulating flow of water along a gold coated surface and a randomly generated one with identical height distribution, it is shown that the position of the effective plane is independent of the boundary structure and that only the height distribution is relevant. Further, these simulations depict the applicability of the lattice Boltzmann method to real surface data. Simulations of flow along surfaces generated from AFM data allow to determine how detected slip might have to be corrected to take surface structures into account. Further, it is shown that the interplay of roughness and hydrophobicity can lead to both, an increase as well as decrease of the measured slip length. This can explain the different experimental findings concerning the roughness dependency of the slip phenomenon[74, 76, 49].

In chapter 6, finite size and discretization effects of a sphere approaching a flat surface are investigated. This work is essential for the following investigation utilizing lubrication force measurements. As the solution of Maude (6.4) is reproducible, it demonstrates that at a ratio $R/n = 1/32$ finite size effects are below 2% and can be neglected near the boundary. It is also demonstrated that a sphere radius of $R = 8$ provides a sufficient resolution. Based on this calibration it is possible to investigate the influence of different surface properties. Further, the influence of a hydrophobic interaction between the approached surface and the fluid is investigated. It is shown that such an interaction leads to a slip with a slip length, which is equivalent to the one found in a Poiseuille flow setup. The chapter shows to what extent such an approach is valid. Further, it shows that such lattice Boltzmann simulations have enough resolution to cover the surface effects that are in the focus of this thesis [77].

Based on these results, it is possible to investigate the influence of roughness on the lubrication force in chapter 7. The main conclusion is that such a flow is fully equivalent to one which would be created past an effective no-slip smooth surface, located at the intermediate position between top and bottom of asperities. Its location is controlled by the density of roughness elements but independent on the flow properties. These results extend the findings of chapter 5.

It is shown that apparent slip created by a hydrophobic surface can be distinguished from roughness which should be treated as an effective boundary. The idea of an effective boundary is applicable even for roughness that is not small compared to the radius of the sphere R or the effective distance d^* between the surface of the sphere and the boundary. Further, it is shown that the effective height r_{eff} of the lubrication based simulations is in agreement with the results from Poiseuille flow simulations. The results show that surface roughness is an issue in AFM-based slip experiments, but it can be treated in an easy manner by shifting the boundary and surface position. The results could have a direct impact on the analysis of SFA/AFM data and other experimental configurations. In addition, they enable the detection of measurement artefacts that lead to erroneous conclusions [78].

In chapter 8, Poiseuille flow in the vicinity of super-hydrophobic surfaces is simulated. Preliminary results show that the simulated velocity profiles qualitatively

correspond with experimental data of Tsai et al. [142]. The slip length is found to depend on the protrusion angle as predicted from the analytic studies by Davis and Lauga [32]. Further, a reduction of the slip length due to the deformation of the bubble at high flow velocities is detected. It is therefore shown that the utilized simulation method is able to model super-hydrophobic systems.

For future work different super-hydrophobic surfaces should be investigated. Those could include a model of stiff rods like it is seen in carbon nanotube forests. Other geometries would include grooves with a larger vapor to solid surface ratio. Also more studies on the Wenzel state could be performed were the interplay of roughness and hydrophobicity is even more crucial. Further some experiments report of an increased slip length for increasing shear. It was argued that in this case the bubbles will not only be deformed, but the contact line will move over the surface. Therefore, a non pinned contact line would be a possible continuation of this work.

Further, it would be desirable to investigate the influence of a super-hydrophobic surface on the lubrication force. In such a case, the anisotropy of the grooved surface should influence the results. This is possible in principle, but requires much more computer power and larger systems than the current ones. The reason is that it is necessary to resolve the force curve down to a small fraction of the spheres radius, while having large bubbles on the lattice scale. The bubble, however, may not be entered by the sphere. Therefore, the sphere has to be significantly larger than it is in the presented work for the rough surfaces.

Other super-hydrophobic like behavior could also be created by having a mixture of two liquids, with the less viscous liquid attracted by the surface. Such a system could consist either of water and oil or of polymer melts with an inhomogeneous molecular weight distribution. In this case, the low viscous fluid would cover the surface roughness, leading to a drag reduction. In principle, it is possible to simulate this as well with a lattice Boltzmann model.

In conclusion, it is shown that the effect of roughness and slippage are two distinguishable phenomena, which are highly related. While roughness leads to a shift of the boundary position, slippage, as it can be created by hydrophobic surfaces, leads to a real increased fluid velocity at the boundary. To obtain a correct description of the boundary condition, both phenomena have to be taken into account. This is especially important in the case of so called super-hydrophobic surfaces where vapor is trapped in the asperities of the surface roughness. It is shown that the lattice Boltzmann method is able to describe such phenomena. Therefore, it can be used as a tool to design surfaces with special properties like a high slippage or simulate more complex microfluidic devices, including the complex behavior close to the boundaries. Further, the findings of this work influence the analysis of slip experiments which analyze the fundamental question which boundary condition one has to apply in fluid flow.

Acknowledgments

- Acknowledgements I thank Jens Harting for taking me on as his PhD student, for his help and supervision, and for employing me at the ICP. Further, I want to thank him for his patience with our papers and my thesis.
- I thank Olga I. Vinogradova for fruitful discussions and the extensive explanation of the problems in AFM based slip experiments. I thank Tony Ladd for providing the main parts of the simulation code, for his hospitality at the University of Florida, and for the helpful hints and discussions.
- I thank the DAAD for the scholarship (Doktorandenstipendium) which enabled me to visit Tony Ladd at the University of Florida. Also, I thank the HPC Europa 2 program for funding my visit at the Eindhoven University of Technology (TU/e).
- Special thanks go to the members of all the institutes that I have been to, which are namely the ICP at the University of Stuttgart, the Department of Chemical Engineering at the University of Florida, and the Mesoscopic Transport Phenomena group at the TU/e. Thanks for the hospitality, the valuable discussions, and the support.
- The work was financed by the DFG priority program "nano- and microfluidics" and by the "Landesstiftung Baden-Württemberg". Computations were performed at the Neumann Institute for Computing, Jülich, at the Scientific Supercomputing Center Karlsruhe, and the ICP condor cluster.
- Last but not least, I want to thank my parents for their support and for giving me the opportunity to go so far.
- And very special thanks to Emily .

Bibliography

[1] A. Ajdari and L. Bocquet. Giant amplification of interfacially driven transport by hydrodynamic slip: diffusio-osmosis and beyond. *Phys. Rev. Lett.*, 96:186102, 2006.

[2] M. P. Allen and D. J. Tildesley. *Computer simulation of liquids*. Clarendon Press, 1994.

[3] J. L. Barrat and L. Bocquet. Large slip effect at a nonwetting fluid interface. *Phys. Rev. Lett.*, 82:4671, 1999.

[4] W. Barthlott and C. Neinhuis. The purity of sacred lotus or escape from contamination in biological surfaces. *Planta*, 202:1, 1997.

[5] J. Baudry and E. Charlaix. Experimental evidance for a large slip effect at a nonwetting fluid-solid interface. *Langmuir*, 17:5232, 2001.

[6] O. Bäumchen, R. Fetzer, and K. Jacobs. Reduced interfacial entanglement density affects the boundary conditions of polymer flow. *Physical Review Letters*, 103(24):247801, 2009.

[7] M. Z. Bazant and O. I. Vinogradova. Tensorial hydrodynamic slip. *J. Fluid Mech.*, 613:125, 2008.

[8] R. Benzi, L. Biferale, M. Sbragaglia, S. Succi, and F. Toschi. Mesoscopic two-phase model for describing apparent slip in micro-channel flows. *Europhys. Lett.*, 74:651, 2006.

[9] P. L. Bhatnagar, E. P. Gross, and M. Krook. Model for collision processes in gases. I. Small amplitude processes in charged and neutral one-component systems. *Phys. Rev.*, 94(3):511, 1954.

[10] L. Bocquet and J. L. Barrat. Hydrodynamic boundary conditions and correlation functions of confined fluids. *Phys. Rev. Lett.*, 70(18):2726, 1993.

[11] L. Bocquet and J. L. Barrat. Hydrodynamic boundary conditions, correlation functions, and kubo relations for confined fluids. *Phys. Rev. E*, 49(4):3079, 1994.

[12] L. Bocquet and J. L. Barrat. Flow boundary conditions from nano- to micro-scales. *Soft Matter*, 3:685, 2007.

[13] E. Bonaccurso, H-J. Butt, and V. S. J. Craig. Surface roughness and hydrodynamic boundary slip of a Newtonian fluid in a completely wetting system. *Phys. Rev. Lett.*, 90:144501, 2003.

[14] G. E. P. Box and M. E. Müller. A note on the generation of random normal deviates. *Ann. Math. Stat.*, 29:610, 1958.

[15] ABD Cassie and S. Baxter. Wettability of porous surfaces. *Transactions of the Faraday Society*, 40:546, 1944.

[16] J. T. Cheng and N. Giordano. Fluid flow through nanometer scale channels. *Phys. Rev. E*, 65:031206, 2002.

[17] J. H. Cho, B. M. Law, and F.Rietord. Dipole-dependent slip on Newtonian liquids at smoothsolid hydrophobic surfaces. *Phys. Rev. Lett.*, 92:166102, 2004.

[18] C-H. Choi and C. J. Kim. Large slip of aqueous liquid flow over a nanoengineered superhydrophobic surface. *Phys. Rev. Lett.*, 96:066001, 2006.

[19] C-H. Choi, U. Ulmanella, J. Kim, C-M Ho, and C. J. Kim. Effective slip and friction reduction in nanograted superhydrophobic microchannels. *Phys. Fluids*, 18:087105, 2006.

[20] C-H. Choi, K. J. Westin, and K. S. Breuer. Apparent slip in hydrophilic and hydrophobic microchannels. *Phys. Fluids*, 15:2897, 2003.

[21] N. V. Churaev, V. D. Sobolev, and A. N. Somov. Slippage of liquids over lyophobic solid surfaces. *J. Colloid Int. Sci.*, 97:574, 1984.

[22] B. Cichocki, R. B. Jones, R. Kutteh, and E. Wajnryb. Friction and mobility for colloidal spheres in Stokes flow near a boundary: The multipole method and applications. *J. Chem. Phys.*, 112:2548, 2000.

[23] M. Cieplak, J. Koplik, and J. R Banavar. Boundary conditions at a fluid-solid interface. *Phys. Rev. Lett.*, 86:803, 2001.

[24] C. Cottin-Bizonne, C. Barentin, E. Charlaix, L. Bocquet, and J. L. Barrat. Dynamics of simple liquids at heterogeneous surfaces: molecular dynamics simulations and hydrodynamic description. *Eur. Phys. J. E*, 15:427, 2004.

[25] C. Cottin-Bizonne, J. L. Barrat, L. Bocquet, and E. Charlaix. Low-friction flows of liquid at nanopatterned interfaces. *Nature Materials*, 2:237, 2003.

[26] C. Cottin-Bizonne, B. Cross, A. Steinberger, and E. Charlaix. Boundary slip on smooth hydrophobic surfaces: intrinsic effects and possible artefacts. *Phys. Rev. Lett.*, 94:056102, 2005.

[27] C. Cottin-Bizonne, S. Jurine, J. Baudry, J. Crassous, F. Restagno, and E. Charlaix. Nanorheology: an investigation of the boundary condition at hydrophobic and hydrophilic interfaces. *Eur. Phys. J. E*, 9:47, 2002.

[28] P. V. Coveney and P. Español. Dissipative particle dynamics for interacting multicomponent systems. *J. Phys. C.*, 30:779, 1997.

[29] P. V. Coveney and K. E. Novik. Computer simulations of domain growth and phase separation in two-dimensional binary immiscible fluids using dissipative particle dynamics. *Phys. Rev. E*, 54(5):5134, 1996.

[30] V. S. J. Craig, C. Neto, and D. R. M. Williams. Shear dependent boundary slip in an aqueous Newtonian liquid. *Phys. Rev. Lett.*, 87:054504, 2001.

[31] D. d Humieères. Multiple relaxation time lattice Boltzmann models in three dimensions. *Phil Trans. A*, 360:437, 2002.

[32] A.M.J. Davis and E. Lauga. Geometric transition in friction for flow over a bubble mattress. *Physics of Fluids*, 21:011701, 2009.

[33] B. Du, I. Doubaidoulline, and D. Johansmann. Effects of laterally heterogeneous slip on the resonance properties of quartz crystals imersed in liquids. *Langmuir*, 20:7794, 2004.

[34] B. Dünweg, U. D. Schiller, and A. J. C. Ladd. Statistical mechanics of the fluctuating lattice Boltzmann equation. *Phys. Rev. E*, 76:36704, 2007.

[35] B. Dünweg and A. J. C. Ladd. Lattice Boltzmann simulations oft soft matter systems. *Advanced computer simulation approaches for soft matter sciences*, 3:89, 2008.

[36] P. Español and P. Warren. Statistical mechanics of dissipative particle dynamics. *Europhys. Lett.*, 30(4):191, 1995.

[37] F. Feuillebois, M.Z. Bazant, and O.I. Vinogradova. Effective slip over superhydrophobic surfaces in thin channels. *Phys. Rev. Lett.*, 102:026001, 2009.

[38] Daan Frenkel and Berend Smit. *Understanding Molecular Simulation*. Academic Press, 2002. ISBN: 0-12-267351-4.

[39] T. M. Galea and P. Attrad. Molecular dynamics study of the effect of solid roughness on the slip length at the fluid-solid boundary during shear flow. *Langmuir*, 20:3477, 2004.

[40] J. Gao, W. D. Leuedtke, and U. Landmann. Layering transitions and dynamics of confined liquid films. *Phys. Rev. Lett.*, 79:705, 1997.

[41] L. Gao and T.K. McCarthty. Contact angle hysteresis explained. *Langmuir*, 22:6234, 2006.

[42] P. Gao and J. J. Feng. Enhanced slip on a patterned substrate due to depinning of contact line. *Physics of Fluids*, 21(10):102102, 2009.

[43] P. G. de Gennes. On fluid/wall slippage. *Langmuir*, 18:3413, 2002.

[44] I. Ginzburg, F. Verhaeghe, and D. d'Humieres. Study of simple hydrodynamic solutions with the two-relaxation-time lattice Boltzmann scheme. *Commun. Comput. Phys.*, 3:519, 2008.

[45] I. Ginzburg, F. Verhaeghe, and D. d'Humieres. Two-relaxation-time lattice Boltzmann scheme: about parametrization, velocity pressure and mixed boundary conditions. *Commun. Comput. Phys.*, 3:427, 2008.

[46] M. Gross, F. Varnik, and D. Raabe. Fall and rise of small droplets on rough hydrophobic substrates. *Europhys. Lett.*, 88:26002, 2009.

[47] J. Harting, M. Harvey, J. Chin, and P. V. Coveney. Detection and tracking of defects in the gyroid mesophase. *Comp. Phys. Com.*, 165:97, 2005.

[48] J. Harting, C. Kunert, and H.J. Herrmann. Lattice Boltzmann simulations of apparent slip in hydrophobic microchannels. *Europhysics Letters*, 75:328–334, 2006.

[49] J. Harting, C. Kunert, and J. Hyväluoma. Lattice Boltzmann simulations in microfluidics: probing the no-slip boundary condition in hydrophobic, rough, and surface nanobubble laden microchannels. *Microfluidics and Nanofluidics*, 8:1, 2010.

[50] Y. Hashimoto, Y. Chen, and H. Ohashi. Immiscible real-coded lattice gas. *Comp. Phys. Comm.*, 129:56, 2000.

[51] H. Hasimoto. On the periodic fundamental solution of the Stokes equations and their application to viscous flow past a cubic array of spheres. *J. Fluid Mech.*, 5:317, 1959.

[52] X. He, Q. Zou, L. S. Luo, and M. Dembo. Analytic solutions of simple flows and analysis of non-slip boundary conditions for the lattice Boltzmann BGK model. *J. Stat. Phys.*, 87:115, 1997.

[53] M. Hecht, J. Harting, M. Bier, J. Reinshagen, and H. J. Herrmann. Shear viscosity of claylike colloids in computer simulations and experiments. *Phys. Rev. E*, 74(2):021403, 2006.

[54] M. Hecht, J. Harting, and H. J. Herrmann. Stability diagram for dense suspensions of model colloidal particles in shear flow. *Phys. Rev. E*, 75(5):051404, 2007.

[55] M. Hecht, J. Harting, T. Ihle, and H. J. Herrmann. Simulation of claylike colloids. *Phys. Rev. E*, 72(1):011408, Jul 2005.

[56] F. J. Higuera, S. Succi, and R. Benzi. Lattice gas dynamics with enhanced collisions. *Europhys. Lett.*, 9(4):345, 1989.

[57] E. J. Hinch. *Pertubation methods.* Cambridge Univ. Press., Cambridge, 1991.

[58] P. J. Hoogerbrugge and J. M. V. A. Koelman. Simulating microscopic hydrodynamic phenomena with dissipative particle dynamics. *Europhys. Lett.*, 19(3):155, 1992.

[59] J. Hyväluoma and J. Harting. Slip flow over structured surfaces with entrapped microbubbles. *Phys. Rev. Lett.*, 100:246001, 2008.

[60] T. Ihle and D. M. Kroll. Stochastic rotation dynamics: a Galilean-invariant mesoscopis model for fluid flow. *Phys. Rev. E*, 63:020201(R), 2001.

[61] T. Ihle and D. M. Kroll. Stochastic rotation dynamics I: formalism, galilean invariance, Green-Kubo relations. *Phys. Rev. E*, 67(6):066705, 2003.

[62] T. Inamuro, M. Yoshino, and F. Ogino. A non-slip boundary condition for lattice Boltzmann simulations. *Phys. Fluids*, 7(12):2928, 1995.

[63] A. Jabbarzadeh, J. D. Atkinson, and R. I. Tanner. Effect of the wall roughness on slip and rheological properties of hexadecane in molecular dynamics simulation of couette shear flow between two sinusoidal walls. *Phys. Rev. E*, 61:690, 2000.

[64] K. M. Jansons. Determination of the macroscopic (partial) slip boundary condition for a viscous flow over randomly rough surface with perfect slip microscopic boundary condition. *Phys. Fluids*, 31:15, 1987.

[65] J. E. Jones. On the determination of molecular fields. ii. from the equation of state of a gas. *Proc. R. Soc. Lond. A*, 463:463, 1924.

[66] P. Joseph, C. Cottin-Bizonne, J. M. Benoit, C. Ybert, C. Journet, P. Tabeling, and L. Bocquet. Slippage of water past superhydrophobic carbon nanotube forests in microchannels. *Phys. Rev. Lett.*, 97:156104, 2006.

[67] P. Joseph and P. Tabeling. Direct measurement of the apparent slip length. *Phys. Rev. E*, 71:035303, 2005.

[68] M. Junk, A. Klar, and L.-S. Luo. Asymptotic analysis of the lattice Boltzmann equation. *J. Comp. Phys.*, 210:676, 2005.

[69] G. Karniadakis, A. Beskok, and N. Aluru. *Microflows and nanoflows, fundamentals and simulation.* Springer, 2005.

[70] M. Knudsen. Experimentelle Bestimmung des Druckes gesättigter Quecksilberdämpfe bei 0^o und höheren Temperaturen. *Ann. d. Phys.*, 29:179, 1909.

[71] J. Koplik and J. R Banavar. No-slip condition for a mixture of two liquids. *Phys. Rev. Lett.*, 80(23):5125, 1998.

[72] J. Koplik, J. R. Banavar, and J. F. Willemsen. Molecular dynamics of fluid flow at solid-surfaces. *Phys. Fluids*, 1:781, 1989.

[73] J. Krim. Friction at macroscopic and microscopic length scales. *Am. J. Phys.*, 70:890, 2002.

[74] C. Kunert and J. Harting. Roughness induced boundary slip in microchannel flows. *Phys. Rev. Lett.*, 99:176001, 2007.

[75] C. Kunert and J. Harting. On the effect of surfactant adsorption and viscosity change on apparent slip in hydrophobic microchannels. *Prog. Comp. Fluid. Mech.*, 8:197, 2008.

[76] C. Kunert and J. Harting. Simulation of fluid flow in hydrophobic rough microchannels. In *International Journal of Computational Fluid Dynamics*, volume 22, page 475, 2008.

[77] C. Kunert and J. Harting. Calibration of lubrication force measurements by lattice Boltzmann simulations. In *Proceedings of the 2nd Micro and Nano Flows Conference (2009)*, 2009.

[78] C. Kunert, J. Harting, and O.I. Vinogradova. Simulations of film drainage to probe random-roughness boundary conditions. *Submitted for publication*, 2009. arxiv:0912.1538.

[79] L. D. Landau and E. M. Lifschitz. *Hydrodynamik*. Akademieverlag, Berlin, 1966.

[80] A. J. C. Ladd. Numerical simulations of particulate suspensions via a discretized Boltzmann equation. part 1. theoretical foundation. *J. Fluid Mech.*, 271:285, 1994.

[81] A. J. C. Ladd. Numerical simulations of particulate suspensions via a discretized Boltzmann equation. part 2. numerical results. *J. Fluid Mech.*, 271:311, 1994.

[82] A. J. C. Ladd and R. Verberg. Lattice-Boltzmann simulations of particle-fluid suspensions. *J. Stat. Phys.*, 104:1191, 2001.

[83] L. D. Landau and E. M. Lifshitz. *Fluid mechanics*. Pergamon Press, 1959.

[84] J. Latt and B. Chopard. A benchmark case for lattice Boltzmann: turbulent dipole-wall collision. *Int. J. Mod. Phys. C*, 18:619, 2007.

[85] J. Latt, B. Chopard, O. Malaspinas, M. Deville, and A. Michler. Straight velocity boundaries in the lattice Boltzmann method. *Phys. Rev. E*, 77:056703, 2008.

[86] E. Lauga, M. P. Brenner, and H. A. Stone. Microfluidics: the no-slip boundary condition. In C. Tropea, A. Yarin, and J. F. Foss, editors, *Handbook of Experimental Fluid Dynamics*, chapter 19, pages 1219–1240. Springer, NY, 2007.

[87] E. Lauga and H. A. Stone. Effective slip in pressure driven flow. *J. Fluid. Mech.*, 489:55, 2003.

[88] N. Lecoq, R. Anthore, B. Cickhocki, P. Szymczak, and F. Feuillebois. Drag force on a sphere moving towards a corrugated wall. *J. Fluid Mech.*, 513:247, 2004.

[89] N. Lecoq, K. Masmoudi, R. Anthore, and F. Feuillebois. Creeping motion of a sphere along the axis of a closed axisymetric container. *J. Fluid Mech.*, 585:127, 2007.

[90] R. Lindken, M. Rossi, Große S, and J. Westerweel. Micro-particle image velocimetry: Recent developments, applications, and guidelines. *Lab Chip*, 9:2551, 2009.

[91] D. Lumma, A. Best, A. Gansen, F. Feuillebois., J. O. Rädler, and O. I. Vinogradova. Flow profile near a wall measured by double-focus fluorescence cross-correlation. *Phys. Rev. E*, 67:056313, 2003.

[92] A. Malevanets and R. Kapral. Continuous-velocity lattice-gas model for fluid flow. *Europhys. Lett.*, 44(5):552, 1998.

[93] A. Malevanets and R. Kapral. Solute molecular dynamics in a mesoscale solvent. *J. Chem. Phys.*, 112(18):7260, 2000.

[94] C. A. Marsh and P. V. Coveney. Detailed balance and H-theorems for dissipative particle dynamics. *J. Phys. C.*, 31:6561, 1998.

[95] A. D. Maude. End effects in a falling-sphere viscometer. *British J. Appl. Phys.*, 12:293, 1961.

[96] J. C. Maxwell. On stresses in rarified gases arising from inequalities of temperature. *Phil Trans. Roy Soc. Lond.*, 70:287, 1879.

[97] D. Maynes, K. Jeffs, B. Woolford, and B. W. Webb. Laminar flow in a microchannel with hydrophobic surface patterned microribis oriented parallel to the flow direction. *Phys. Fluids*, 19:093603, 2007.

[98] G. McHale and M. I. Newton. Surface roughness and interfacial slip boundary condition for quarzcrystal microbalances. *J. Appl. Phys.*, 95:373, 2004.

[99] G. R. McNamara and G. Zanetti. Use of the Boltzmann equation to simulate lattice-gas automata. *Phys. Rev. Lett.*, 61(20):2332, 1988.

[100] A. Narváez, T. Zauner, F. Raischel, R. Hilfer, and J. Harting. lattice-Boltzmann simulations for permeability calculations in porous media. *IN PREPARATION*, 2009.

[101] C. L. M. H. Navier. Mémoire sur les lois du mouvement de fluids. *Mem. Acad. Sci. Ins. Fr.*, 6:389, 1823.

[102] M. Nekovee and P. V. Coveney. Lattice Boltzmann simulations of self assembly of binary amphiphilic fluids into ordered lamellar and bicontinous cubic phases. *J. Am. Chem. Soc.*, 123(49):12380, 2001.

[103] C. Neto, V. S. J. Craig, and D. R. M. Williams. Evidence of shear-dependent boundary slip in Newtonian liquids. *Eur. Phys. J. E*, 12:71, 2003.

[104] C. Neto, D. R. Evans, E. Bonaccurso, H. J. Butt, and V. S. J. Craig. Boundary slip in Newtonian liquids: a review of experimental studies. *Rep. Prog. Phys.*, 68:2859, 2005.

[105] N. Q. Nguyen and A. J. C. Ladd. Lubrication corrections for lattice-Boltzmann simulations of particle suspensions. *Phys. Rev. E*, 66(4):046708, October 2002.

[106] X. Nie, G. D. Doolen, and S. Chen. Lattice-Boltzmann simulations of fluid flows in MEMS. *J. Stat. Phys.*, 107:279, 2002.

[107] J. Ou and G. R. Rothstein. Direct velocity measurement of flow past drag-reducing ultrahydrophobic surfaces. *Phys. Fluids*, 17:03606, 2005.

[108] P. Panzer, M. Liu, and D. Einzel. The effects of boundary curvature on hydrodynamic fluid flow: calculation of slip lengths. *Int. J. Mod. Phys. B*, 6:3251, 1992.

[109] J. R. Philip. Flow satisfying mixed no-slip and no-shear conditions. *J. Appl. Math. Phys.*, 23:353, 1972.

[110] R. Pit, H. Hervert, and L. Léger. Direct experimental evidence of slip in hexadecane:solid interface. *Phys. Rev. Lett.*, 85:980, 2000.

[111] N. V. Priezjev, A. A. Darhuber, and S. M. Troian. Slip behavior in liquid films on surfaces of patterned wettability: Comparison between continuum and molecular dynamics simulations. *Phys. Rev. E*, 71:041608, 2005.

[112] Y.H. Qian, D. d'Humieres, and P. Lallemand. Lattice BGK models for Navier-Stokes equation. *Europhys. Lett.*, 17:479, 1992.

[113] R. Rabenseifner. *Parallel programing workshop; introduction to computational fluid dynamics*. HLRS Stuttgart, 2005.

[114] S. Richardson. On the no-slip boundary condition. *J. Fluid Mech.*, 59:707, 1973.

[115] J.P. Rothstein. Slip on superhydrophobic surfaces. *Annu. Rev. Fluid Mech.*, 42:89, 2010.

[116] T. Sakai, Y. Chen, and H. Ohashi. Formation of micelle in the real-coded lattice gas. *Comp. Phys. Comm.*, 129(1–3):75, 2000.

[117] M. Sbragaglia, R. Benzi, L. Biferale, S. Succi, and F. Toschi. Surface roughness-hydrophobicity coupling in microchannel and nanochannel flows. *Phys. Rev. Lett.*, 97:204503, 2006.

[118] M. Sbragaglia and A. Prosperetti. A note on the effective slip properties for microchannel flows with ultrahydrophobic surfaces. *Phys. Fluids*, 17:043603, 2007.

[119] H. Schlichting. *Boundary-layer theory.* McGraw-Hill, 1979.

[120] T. Schmatko, H. Hervert, and L. Leger. Friction and slip at simple fluid-solid interfaces. the roles of the molecular shape and the solid liquid interaction. *Phys. Rev. Lett.*, 94:244501, 2005.

[121] S. Schmieschek and J. Harting. Contact angle determination in multicomponent lattice boltzmann simulations. *arXiv:0910.3915v1*, 2009.

[122] E. Schnell. Slippage of water over nonwettable surface. *J. Appl. Phys.*, 27:1149, 1956.

[123] F. Schwabl. *Statistische Mechanik.* Springer, 2000.

[124] X. Shan and H. Chen. Lattice Boltzmann model for simulating flows with multiple phases and components. *Phys. Rev. E*, 47(3):1815, 1993.

[125] X. Shan and H. Chen. Simulation of nonideal gases and liquid-gas phase transitions by the lattice Boltzmann equation. *Phys. Rev. E*, 49(4):2941, 1994.

[126] X. Shan and G. Doolen. Multicomponent lattice-Boltzmann model with interparticle interaction. *J. Stat. Phys.*, 81(112):379, 1995.

[127] P. A. Skordos. Initial and boundary conditions for the lattice Boltzmann method. *Phys. Rev. E*, 48:4823, 1993.

[128] A. Strook, S. K. W. Dertinger, A. Ajdari, I. Mezić, H. A. Stone, and G. M. Whitesides. Chaotic mixer for microchannels. *Science*, 295:647, 2002.

[129] S. Succi. *The lattice Boltzmann equation for fluid dynamics and beyond.* Oxford University Press, 2001.

[130] S. Succi. Mesoscopic modeling of slip motion at fluid-solid interfaces with heterogeneous catalysis. *Phys. Rev. Lett.*, 89:064502, 2002.

[131] M. C. Sukop and D. T. Thorne Jr. *Lattice Boltzmann modeling.* Springer, 2007.

[132] G. Sun, E. Bonaccurso, V. Franzand, and H. J. Butt. Confined liquid: simultaneous observation of a moleculary layer structure and hydrodynamic slip. *J. Chem Phys.*, 117:10311, 2002.

[133] M. R. Swift, E. Orlandini, W. R. Osborn, and J. M. Yeomans. Lattice-Boltzmann simulations of liquid-gas and binary fluid mixtures. *Phys. Rev. E*, 54(5):5041, 1996.

[134] M. R. Swift, W. R. Osborn, and J. M. Yeomans. Lattice Boltzmann simulation of nonideal fluids. *Phys. Rev. E*, 75(5):830, 1995.

[135] P. A. Thompson and M. O. Robbins. Shear flow near solids: epitaxial order and flow boundary conditions. *Phys. Rev. A*, 41:6830, 1990.

[136] P. A. Thompson and S. Troian. A general boundary condition for liquid flow at solid surfaces. *Nature*, 389:360, 1997.

[137] P. A. Tompson and S. M. Trojan. A general boundary condition for liquid flow at solid surfaces. *Nature*, 389:360, 1997.

[138] D. C. Tretheway and C. D. Meinhart. Apparent fluid slip at hydrophobic microchannel walls. *Phys. Fluids*, 14:L9, 2002.

[139] D. C. Tretheway and C. D. Meinhart. A generating mechanism for apparent slip in hydrophobic microchannels. *Phys. Fluids*, 15:1509, 2004.

[140] D. C. Tretheway, L. Zhu, L. Petzold, and C. D. Meinhart. Examination of the slip boundary condition by micro-PIV and lattice Boltzmann simulations. *Proc. of IMECE*, 2002.

[141] R. Truesdell, A. Mammoli, P. Vorobieff, P. van Swol, and C. J. Brinker. Drag reduction on a patterned superhydrophobic surface. *Phys. Rev. Lett.*, 97:044504, 2006.

[142] P. Tsai, A. M. Peters, C. Pirat, M. Wessling, R. G. H. Lammertink, and D. Lohse. Quantifying effective slip length over micropatterned hydrophobic surfaces. *Physics of Fluids*, 21:112002, 2009.

[143] O. B. Usta, A. J. C. Ladd, and J. E. Butler. Lattice-Boltzmann simulations of the dynamics of polymer solutions in periodic and confined geometries. *J.Chem. Phys.*, 122:094902, 2005.

[144] F. Varnik, D. Dorner, and D. Raabe. Roughness-induced flow instability: A lattice Boltzmann study. *J. Fluid Mech.*, 573:191, 2007.

[145] R. Verberg and A. J. C. Ladd. Accuracy and stability of a lattice-Boltzmann model with subgrid scale boundary conditions. *Phys. Rev. E*, 65:016701, 2001.

[146] O. I. Vinogradova. Drainage of a thin film confined between hydrophobic surfaces. *Langmuir*, 11:2213, 1995.

[147] O. I. Vinogradova. Possible implications of hydrophopic slippage on the dynamic measurements of hydrophobic forces. *J. Phys. Cond. Mat.*, 8:9491, 1996.

[148] O. I. Vinogradova, K. Koynov, A. Best, and F. Feuillebois. Direct measurements of hydrophobic slippage using double-focus fluorescence cross-correlation. *Physical Review Letters*, 102:118302, 2009.

[149] O. I. Vinogradova and G. E. Yakubov. Dynamic effects on force mesurements. 2. lubrication and the atomic force microscope. *Langmuir*, 19:1227, 2003.

[150] O. I. Vinogradova and G. E. Yakubov. Surface roughness and hydrodynamic boundary conditions. *Phys. Rev. E*, 73:045302(R), 2006.

[151] Y. Wang, B. Bhushan, and A. Maali. Atomic force microscopy measurement of boundary slip on hydrophilic, hydrophobic, and superhydrophobic surfaces. 27:754, 2009.

[152] D. E. Weidner and L. W. Schwartz. Contact-line motion of shear-thinning liquids. *Physics of Fluids*, 6:3535–3538, 1994.

[153] R. N. Wenzel. Resistance of solid surfaces to wetting by water. *Ind. Eng. Chem.*, 28:988, 1936.

[154] S. C. Yang and L. B. Fang. Effect of surface roughness on slip in hydrophobic and hydrophilic microchannels by molecular dynamics simulation. *Molecular Simulation*, 31:971, 2005.

[155] T. Young. An essay on the cohesion of fluids. *Philos. Trans. R. Soc. London*, 95:65, 1805.

[156] Y. Zhu and S. Granick. Rate-dependent slip of Newtonian liquid at smooth surfaces. *Phys. Rev. Lett.*, 87:096105, 2001.

[157] Y. Zhu and S. Granick. Limits of the hydrodynamic no-slip boundary condition. *Phys. Rev. Lett.*, 88(10):106102, 2002.

[158] Y. Zhu and S. Granick. No-slip boundary condition switches to partial slip when fluid contains surfactant. *Langmuir*, 18:10058, 2002.